# Numerical Modelling and Field Study of Thermal Plume Dispersion in Rivers and Coastal Waters

Abolghasem Pilechi

Thesis submitted to the Faculty of Graduate and Postdoctoral Studies in partial fulfillment of the requirements for the Doctorate of Philosophy in Civil Engineering

Department of Civil Engineering

Faculty of Engineering

University of Ottawa

# Abstract:

Field measurement and numerical modeling are the most popular and fundamental approaches for studying mixing pattern in rivers and coastal waters. Due to the limitations associated with both of these methods they should be used together to verify each other.

Extensive field measurement was conducted on the effluent plume from the outfall of the Capital Region waste water treatment plant in the North Saskatchewan River. Tracer was injected at the outfall location and the mixing pattern was investigated by tracking the tracer concentration over a 83 km reach of the river. Flow velocity and depth were also measured simultaneously using an acoustic Doppler current profiler. An integrated *in situ* fluorometer-GPS measurement technique was introduced and used for field tracer studies in meandering rivers. The full transverse mixing length for the river was estimated to be 130 km.

A stream-tube orthogonal curvilinear mesh generation algorithm was also developed for numerical modeling of meandering rivers. The method eliminates the effect of transverse velocity field using the stream-tube concept. The field measured velocity data were used for calculating the stream tube width in each cross-sectional strip. The stream-tube grid was used to develop a practical and efficient coupled field-numerical model for estimating the transverse mixing coefficient in meandering rivers. In this model the computational costs associated with solving the hydrodynamic sub-model is reduced by generating the velocity field from measured data. Using the calibrated model, the average transverse mixing coefficient was calculated for the surveyed reach.

Extensive field study was also conducted on the near-field and far-field of a thermal plume discharged by the Ras Laffan Industrial City in Qatar. Three-dimensional perspective of the plume behavior was obtained using field measured temperature and velocity data. Different characteristics of the observed plume including the extent of different zones of the plume, plume thickness, detachment depth and variation of the minimum dilution were investigated and compared with available theories. The

contribution of each effective mixing mechanism was also calculated using the field measured data. Vertical confinement was found to be the main effective parameter on the near-field mixing rate which reduced the minimum dilution rate up to 80%.

An innovative remote sensing technique was introduced to investigate the near-field mixing of thermal surface plumes. The method generates a calibrated thermal image of the plume using LandSat thermal infrared (TIR) satellite images. Using a combination of remote sensing and numerical modeling, the near-field dynamics of the plume was found to be influenced by the wind action. It was also observed that the previous classification for determining the effect of wind on the plume dynamics did not successfully predict the plume behavior in shallow water. Two non-dimensional parameters, $WI_1=U_{wl}/U_0$ (ratio of the long-shore wind speed ($U_{wl}$) to the discharge velocity ($U_o$) and $WI_2= U_{wc}/U_0$ (ratio of the cross-shore wind ($U_{wc}$) to the discharge velocity), were introduced to quantify the effect of wind on the plume dilution and deflection. The plume trajectory was found to be sensitive to a longshore wind greater than 2 m/s, which is half of the reported value for deep water conditions.

The surveyed coastal outfall was also modeled using a nested coupled hydrodynamic-wave approach. Validation of the model with field measured and remote sensing data showed that the employed approach can be used for engineering applications such as designing outfall systems and environmental impact assessment purposes. The calibrated model was used to investigate the effect of various effective factors on the mixing process such as lateral confinement, wave-flow interaction, wave dissipation factors and turbulence models. Lateral confinement was found to reduce the mixing potential of the outfall by 50% at the end of the near-field.

تقدیم به مادرم،

که راه درست زندگی کردن را به من آموخت و هر آنچه دارم از فداکاری ها و حمایت های اوست

و

همسرم،

که همواره مشوق و همراه من در روزهای سخت زندگیست

To my mother who taught me the meaning of living with decency and whose support and sacrifice I owe everything I have achieved in life; and to my wife who has always been a source of encouragement through all the hard times

# Acknowledgements

It is an honor for me to thank those who made this thesis possible and words fail to appreciate them in a way that it should be.

First and foremost, I express my sincere gratitude to my supervisors, Dr. Majid Mohammadian and Dr. Colin Rennie for their extraordinary supervision, guidance, and contribution which have helped me form and strengthen this thesis and the work presented herein.

I extend my appreciation to Dr. Mohammad Albeldawi and Ramadorai Kadambi from Qatar Petroleum, and Dr. Hazim Qiblawey from Qatar University for their support in conducting field study on the outfall of Ras Laffan Industrial City.

To my parents, Afsar Kamali and Hasan Pilechi, my wife Mahvin Memarpour, my sister Maryam Pilechi and brother in law Mohammad Reza Aghmasheh who have blessed me with an endless supply of patience, encouragement and support throughout my life and education.

I also want to thank Qatar National Research Foundation for kindly providing funding for this project.

**Symbols:**

$a_0$ : Cross-sectional area ($m^2$)

*b:* river width (m)

$C_b$ : Geometrical spreading factor

$E_z$ : Transverse mixing coefficient ($m^2s^{-1}$)

$f_b$: Bottom friction (m)

$H$ : Mean channel depth (m)

$\beta$ :Empirical coefficient

$\Gamma_{HG}$ :Unsteadiness parameter ()

ΔD: Change in depth (m)

ΔT: Time duration of the wave (s)

h: Average depth

S: River slope

$\beta$= empirical coefficient (-)

$\kappa$ = 0.41, von Kármán constant (-)

*b:* river width (m)

$b_0$ : Discharge channel width depth (m)

$C$ : Depth-averaged concentration (ppb)

D: Factor of diffusion ()

$E_z$: Transverse mixing coefficient ($m^2s^{-1}$)

$F_0$ : Densimetric Froude number

$g$ : Gravity ($m^2\ s^{-1}$)

$g_0'$ : Initial buoyancy acceleration ($m^2\ s^{-1}$)

$h_0$: Discharge channel depth (m)

$h_{max}$: Maximum plume thickness (m)

$h_{far}$ : Far-field thickness of the plume (m)

$H$: mean channel depth (m)

$IQR = Q3- Q1$, interquartile range ($ms^{-1}$)

$J_0$ : Buoyancy flux ($m^2s^{-3}$)

$k_s$ : Roughness (m)

$k_\alpha$ : Longitudinal mixing coefficient ($m^2s^{-1}$)

$k_\beta$ : Transverse dispersion coefficient ($m^2s^{-1}$)

$L$ : Lower and upper limits of the confidence range ($ms^{-1}$)

$L_z$ : Full mixing length (m)

$L_c$ : Distance downstream of the source where the tracer reaches the opposite bank (m)

$L_z$: Transverse mixing distance (m)

$L_M$ : Jet-to-plume-length scale (m)

$L_Q$: Discharge length scale (m)

$m_\alpha$: Metric coefficients

$m_\beta$ : Metric coefficients

$M_0$: Injection mass rate ($kgs^{-1}$)

$M_0$: Momentum flux ($kgm^{-1}s^{-1}$)

$n$ : Number of points in the velocity profile and the regression residuals (-)

$Obs$ : observation value ($ms^{-1}$)

$P_m$ : ratio of minimum to maximum concentration (-)

$P_m$ : Minimum to maximum concentration (-)

q: Cumulative discharge ($m^3s^{-1}$)

$Q_0$ : Volume flux ($ms^{-1}$)

$Q1$: first quartiles ($ms^{-1}$)

$Q3$: third quartiles ($ms^{-1}$)

$r_c$: Radius of curvature (m)

$r_s$: Ratio of the observed dilution to the predicted dilution (-)

$Ri^*$ : Richardson number (-)

$s$ : Standard error ($ms^{-1}$)

$S_{min}$: The minimum dilution parameter (-)

$S_{mean}$ : Mean dilution (-)

$S_n$: Sinuosity (-)

$T_0$ : Discharge temperature (C°)

$T_a$ : Ambient water temperature (C°)

$t_{\alpha/2,n-1}$ : standard random variable (C°)

$u$: velocity in the bin at height $z$ ($ms^{-1}$)

$U_m$ : Maximum velocity along the jet axis ($ms^{-1}$)

$u'$ : The deviation of the depth-averaged velocity ($ms^{-1}$)

$u_a$ :Ambient water velocity ($ms^{-1}$)

U: Average velocity ($ms^{-1}$)

$U$: upper limits of the confidence range ($ms^{-1}$)

$U_{0:}$ Discharge velocity ($ms^{-1}$)

$u^*$ : shear velocity ($ms^{-1}$)

$U^*$: average shear velocity ($ms^{-1}$)

$v$ : river average velocity ($ms^{-1}$)

$v_\alpha$ : Depth-averaged velocity along the river ($ms^{-1}$)

W: Cross section width (m)

$W^*$ : Wind shear stress ($kgm^{-1}s^{-2}$)

$WI_1$: Non-dimensional parameter (-)

$WI_2$: Non-dimensional parameter (-)

$\Delta\alpha_{i,j,}$: Grid sizes at cell ($i$,$j$) in the $\alpha$ direction (m)

$\Delta\beta_{i,j}$ : Grid sizes at cell ($i$,$j$) in the $\beta$ direction (m)

$\psi$ : Shape factor parameter (-)

$\rho_{0:}$ Discharge density ($kg/m^3$)

$\sigma_0$: Discharge channel direction

$\rho_a$ : Average ambient density ($kgm^{-3}$)

# Chapter 1:

## Introduction

Mixing of wastewater effluent in rivers and coastal areas is a primary research area in environmental hydraulics. Mixing is important with respect to both short-term immediate toxicity of the disposed materials as well as their long term effect on aquatic life and the ecosystem. River and coastal ecosystems provide many ecosystem services, including provision of one of the main human food sources. Furthermore, surface and ground water resources are relied on for drinking, irrigation and recreational purposes. Water quality studies are thus critical.

Dissolved oxygen (DO) is one of the most effective parameters in aquatic life. The level of DO in a flowing stream is highly influenced by Biochemical Oxygen Demand (BOD) loading introduced by wastewater effluent discharged into rivers. Recreational beaches can also be contaminated with pathogens from nearby rivers that carry disposed industrial waste, sewage, or non-point sources of contaminants.

Another example of perturbation effect on the aquatic environment can be seen in phytoplankton cases. About 2% of the worldwide known phytoplankton species are harmful (Landsberg 2002), and algae blooms are related to environmental parameters such as temperature, salinity and dissolved oxygen. Desalination plants generally discharge effluent with higher temperature and salinity than the ambient water. Therefore, the long term effect of desalination plants discharges on the receiving environment can include increased average temperature and salinity of the ambient water, especially in locations close to the outfall. This will consequently increase the risk of harmful algae blooms in these regions. The growth rate of phytoplankton also depends on the relative abundance of substances such ammonia, urea, nitrate ions etc., which can be present in industrial outfalls (Moore et al. 2011).

Due to the importance of water resources pollution, many different environmental assessment studies have been conducted by biologists and environment researchers in different regions of the world. The results of these studies have been used in preparing environmental protection guidelines. The guidelines

indicate the maximum allowed discharging level for harmful materials in the receiving water based on the particular species living in that region, which may vary based on the geographical location. The US Environmental Protection Agency is one of the oldest and most well-known organizations in this field.

Studies are also carried out with the purpose of assessing the fulfillment of environmental regulations. The main goal of all of these studies is to determine the current environmental situation and to develop a general, accurate and applicable controlling method. Mixing studies fall within this category and are conducted to improve the understanding about the mixing pattern of different outfalls systems in the receiving environment which can be river, sea or ocean. Mixing study results can greatly help environmental authorities to prepare development plans and to make decisions in critical situations.

### 1.1 Objectives

The aim of this study is to improve understanding of the mixing process and invent a simple and reliable method for modelling the near field and far field fate of neutral/buoyant effluents in rivers and coastal regions. The subject of this study is twofold. The first goal is to employ advanced field measurement and remote sensing techniques in understanding both near field and far field mixing. The second goal is to develop simple and accurate numerical approaches in predicting the mixing process. In the current study the mixing process is investigated in both a natural river and a coastal region as the most common receiving water bodies. The study of each case will be carried out using both field measurement and the numerical approaches. The river mixing case of the study is carried out on a surface municipal wastewater treatment outfall in the North Saskatchewan River. Understanding mixing of the effluent in the North Saskatchewan River is important for managing downstream uses, which include drinking water and agriculture. The coastal mixing part of the project is conducted on the Ras Laffan Industrial City (RLIC) outfall in Qatar. Qatar is a developing country with extended coastline of 563 km length which supplies most of its needed water from desalination plants (Darvish and Mohtar 2012). The water environmental pollution associated with industrial activities has always been a concern for Qatar environmental authorities (Darwish and Mohtar 2012). Understanding the mixing pattern of RLIC as the biggest

industrial compound in Qatar is required to evaluate the current environmental situation and to develop environmental protection plans.

### 1.2 Mixing in Meandering rivers; case study: mixing in the North Saskatchewan River

Water quality of the North Saskatchewan River (NSR) has been identified as a substantial issue in the North Saskatchewan Regional Plan (Alberta Government). Understanding how inputs to the river are mixed is essential in development and calibration of accurate water quality models. The contaminants are introduced into the river from point sources such as the outfalls of industrial plants and non-point sources such as runoff from agricultural activities. Understanding the mixing patterns along the river helps environmental authorities to improve the reliability of existing surface water quality models, which are used to determine the permissible duration and the magnitude of accidental or controlled discharges into the river.

Following the above mentioned goals, a field campaign was carried out on the North Saskatchewan River between October 26 to October 28, 2011 to study the physical mixing of Capital Region Wastewater Treatment Plant (WWTP) effluent with the ambient river. A new *in situ* field measurement technique was introduced and used in this part of the project. Details of the field work technique and the analysis of the observed mixing pattern is provided in the third chapter of this thesis. The results of the field study were also used in a novel data driven numerical model that was developed for predicting the mixing pattern in the North Saskatchewan River. The developed model utilizes an innovative stream-tube orthogonal curvilinear grid. The details of the model as well as the developed generated mesh are provided in Chapter Four.

### 1.3 Mixing in coastal waters; case study: Ras Laffan Industrial City outfall

Ras Laffan Industrial City is the largest industrial compound of Qatar. Sea water is used to cool petrochemical, gas and fuel refinery in the industrial city. Part of the heated water from the plants is

transferred to the Ras Laffan desalination plant. Desalination plants usually use sea water and discharge their hypersaline outfall into the sea. The Ras Laffan desalination plant uses a Multi Stage Flash (MSF) process. Due to the added heat, MSF desalination plant effluent is normally neutral or positively buoyant, which causes the plume to rise. In the Ras Laffan compound the effluent of the desalination plant is mixed with the cooling water which comes from other plants before being discharged into the sea. The productivity of the desalination plant is 10%, so the effluent salinity is expected to be 10% higher than the sea water. As this effluent is mixed with the mentioned cooling water before discharging into the port, the final effluent density is lower than the receiving water.

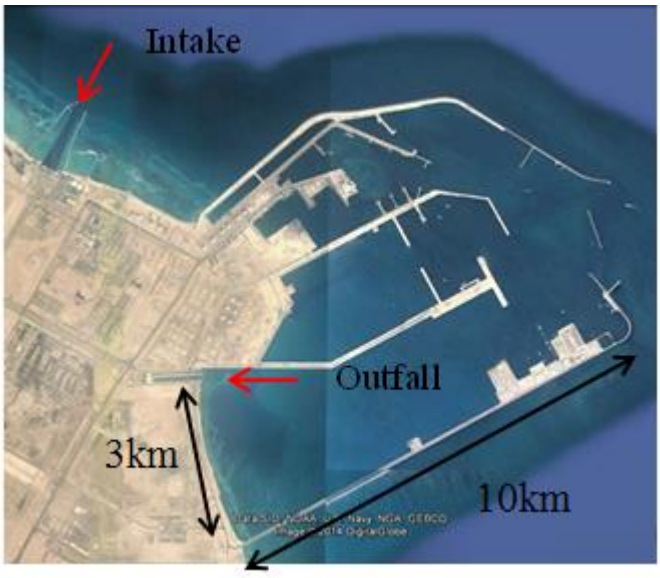


**Figure 0.1 Ras Laffan Industrial City Port. The photo was adopted from the Google Earth**

RLIC has a surface outfall located at 25° 53.480' North (latitude) and 51° 34.483' East (longitude), discharging about 222 $m^3/s$ into the sea. The very high discharge value and shallow depth at the outfall generate a wall-jet-like flow regime. The outfall is located inside the Ras Laffan port, and therefore the generated plume is a confined jet. The water level in the port varies during the tidal cycle; however, due to the low tidal current velocity in the port, the ambient water can be considered as stagnant.

### 1.4 Approach

Extensive field measurements were carried out in both cases. The North Saskatchewan field work was carried out in October 2011 and the RLIC field survey was carried out in March and May 2014. On the North Saskatchewan River, Rhodamine WT was injected as the tracer in the Capital Region WWTP effluent. The tracer concentration was tracked from a boat moving both across and along the river using an *in situ* fluorometer integrated into a Conductivity, Temperature Depth (CTD) instrument over a total distance of 83km along the river path for a period of three days between October 26 to October 28, 2011. For the RLIC study, the near field and far field temperature and salinity of the RLIC effluent plume were also surveyed using a CTD. The collected data from the RLIC field campaigns as well as measured data from three environmental buoys outside of the port was used in calibrating available LandSat7 thermal infra-red (TIR) imagery to estimate plume temperature spatial distributions.

In both cases hydrodynamics parameters (water velocity and depth) were measured using an acoustic Doppler current profiler (aDcp). The CTD and aDcp data was collected simultaneously and synchronized by means of Global Positioning System (GPS) position and time-stamp data that was integrated into the data streams collected by both the CTD and aDcp.

A numerical model was also developed for estimating the transverse mixing in the North Saskatchewan River. The model was based on a proposed coupled field-modelling approach which provides a practical and low cost simulation for highly extended domains. The model employs an orthogonal stream-tube gridding system for the investigation of mixing patterns in meandering rivers. The model was shown to be efficient and reliable in estimating the transverse mixing as well the full mixing length in meandering rivers.

A nested wave-flow numerical model was also developed and validated using the measured field data and the satellite imagery from the RLIC plume.

The model uses the measured water level, temperature, wind and discharge data to predict the velocity field and mixing processes. Moreover, different effective parameters on the mixing processes are investigated including the lateral confinement of the outfall, wave interaction with the ambient flow, wave dissipation factors and different turbulence models.

### 1.5 Novelty and contribution of this research

The novelty of this study can be presented in field measurement, numerical modelling, remote sensing and analytic modelling aspects. This section provides a summary of the contributions of this study in each group and its corresponding chapter.

In Chapter Three, a new *in situ* technique is introduced for field tracer study in natural meandering rivers. The method provides high resolution spatiotemporal data for tracer concentration and hydrodynamics by integrating real-time position data into both *in situ* fluorometer and aDcp data collected at each surveyed point.

A practical and computationally efficient numerical approach for modelling the mixing process in meandering rivers is proposed in Chapter Four. In this chapter, first an innovative stream-tube orthogonal curvilinear method is introduced to generate the computational mesh required for numerical modelling of meandering rivers. A novel practical coupled field-modelling approach model is then developed employing the proposed gridding system for the investigation of contaminant-mixing in meandering rivers.

Using the proposed field measurement technique developed in Chapter Three, the spatial distribution of the thermal plume effluent and the jet velocity of the Ras Laffan Industrial City (RLIC) surface outfall are investigated in Chapter Five. The investigated outfall is distinctive from the previously reported outfalls in the literature due to its very large aspect ratio, lateral confinement and shallow water depth. All of the mentioned parameters were expected to have a significant effect of the mixing process of the effluent,

especially in the near-field. Using the real-time field measurement method made it possible to investigate various aspects of mixing processes that have been rarely evaluated in previous field studies. An innovative remote sensing technique is introduced by calibrating the thermal infrared satellite images using surface water temperature data measured with the CTD probe for investigating the dynamics of the thermal plume in the near-field and far-field.

The proposed remote sensing technique in Chapter Five is employed for investigating the effect of wind on the near-field dynamics of a surface thermal plume of Ras Laffan Industrial City (RLIC) in Chapter Six. Various forcing factors that affect plume dynamics and mixing process are evaluated using a combination of the remote sensing and numerical modelling approaches. The relative importance of wind and discharge momentum wind effect on the near field plume trajectory and the mixing rate is quantified using two innovative non-dimensional parameters.

Finally a nested efficient and practical coupled hydrodynamic-wave approach is introduced in Chapter 7 to model the mixing pattern of thermal plumes in coastal waters. The proposed approach is found to be efficient and practical in designing surface outfalls and conducting environmental mixing studies especially in cases with lack of measured data. The model performance is validated using the field measured data as well as the thermal map data obtained from the remote sensing approach as discussed in Chapter Six

### 1.6 Dissertation Outline

The literature on mixing studies is reviewed in Chapter 2, including near field and far field mixing approaches, hydrodynamic models, and river and coastal mixing studies. The outcome of this review is an assessment of the strengths and weaknesses of current approaches, from which the novel contributions of this thesis to advance understanding of mixing processes are summarized. The field study conducted on the Capital Region WWTP outfall in the North Saskatchewan is explained in detail in Chapter 3. The developed coupled field-numerical model approach and the mesh generating method are summarized in

Chapter 4. The field study on the RLIC outfall and the proposed field-remote sensing technique is discussed in Chapter 5. Using the introduced remote sensing technique, the effect of tidal and wind on the plume dynamics are investigated in Chapter 6. Dispersion of the RLIC plume is modeled using a nested coupled flow-wave numerical model in Chapter 7. Conclusions of this research are provided in Chapter 8. It should be noted that Chapters 3, 4, 5, 6 and 7 in this dissertation are all presented in the format of a technical paper. Chapter 3 has been published in the Journal of Hydraulic Research . Chapter 4 has two parts. The first part that discusses the gridding method has been published in the proceedings of the Canadian Society of Civil Engineering general conference, 2013 Montreal. The second part, which discusses the numerical model and evaluates it performance against the field measurements, has been accepted to be published in in the Journal of Hydraulic Engineering ASCE. Chapters 5 and 6 will be submitted as companion papers in the Journal of Environmental Fluid Mechanics. Chapter 7 will be submitted in Environmental Modelling and Software.

# Chapter 2: **Literature review**

## 2.1 Introduction

The mixing process is generally investigated in the near field or the far field. The near field is defined as the region in which the mixing is controlled by the initial discharge momentum and buoyancy flux as well as the outfall geometry (Jirka et al. 1996). Effluent mixing in the far-field is mainly caused by the ambient flow advection and diffusion. This is also known as passive diffusion and its mixing process is controlled by the turbulence characteristics of the ambient flow (Jirka et al. 1991).

The near field and far field mixing processes are different with respect to their length and time scales. Length scale addresses the largest possible eddy size that causes the mixing. These eddies are sources of momentum, mass and energy transfer in and out of a control volume. For example, the transverse eddies that rotate horizontally, about a vertical axis causes lateral mixing in a river (Gualtieri 2009).

The intermediate field definition also has been used in some studies as the region downstream of the outfall in which the mixing process is still affected by the initial momentum and buoyancy characteristics.

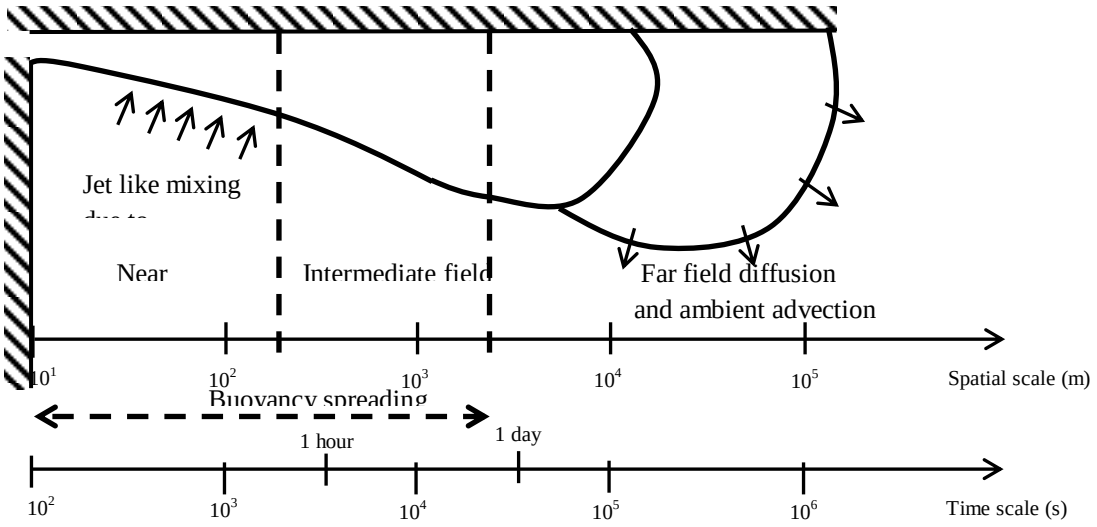


**Figure 2.1 Classification of the hydrodynamic processes**

Due to the large width to depth ratio, the vertical mixing usually occurs close to the outfall in rivers and the near field region is considered from the discharge point up to the point of full vertical mixing. The intermediate field in rivers is defined between the full vertical mixing to the point where full transverse mixing occurs and the far field region begins after this point (Baek and Seo 2010). The full transverse mixing length in rivers is defined as the longitudinal distance required to achieve complete mixing (equal concentration) across the channel (Rutherford 1994). The full mixing condition is assumed when the ratio of the minimum to the maximum concentration ($P_m=S_{min}/S_{max}$) reaches the certain limit, normally 0.98, 0.95 or 0.9 (Rutherford 1994).

In this chapter the river mixing and coastal mixing literature is reviewed in different sub-sections.The outfall systems can be generally categorized as single port, multiport and surface outfalls. They are also different with respect to the discharge capacity, construction cost and dilution potential. Surface outfalls are of the most popular outfall systems due to their low cost and large discharge volume capacity. As both of the investigated cases in this study have a surface outfall, this literature review is more focused on surface discharges.

Effluent outflows generally have different velocity and density from the receiving water. Therefore, the effluent is named as jet in the case of momentum driving force or plume when it is driven as a result of buoyancy. Effluents are generally called buoyant jet or forced plume (Jirka et al. 1996) in the literature if they are influenced by both momentum and buoyancy effects.

The surface jet flows can be divided into three principal regions as the Zone of Flow Establishment (ZFE), the near field and the far field (Lin et al. 1977). The ZFE is the closest region to the outfall. The effluent has uniform “top hat” shaped velocity and temperature profiles at the discharge location. The velocity difference between the ZFE jet and the ambient water produce shear and consequently turbulence around the jet. The ambient water entrains the ZFE and decreases the width of this region with distance from the outfall. The extent of ZFE is defined from the outfall location to the point that the jet centerline

velocity or temperature starts to decay from the discharge value. The length of the ZFE for temperature is less than velocity due to the higher turbulent diffusion coefficient (Lin et al. 1977).

The next region is the near-field, also known as the Zone of Established Flow (ZEF), in which the mixing is affected by the initial volume, momentum and buoyancy fluxes. Velocity, salinity and temperature all have a self-similar Gaussian shape profile in this region. In some studies, the extent of the near-field region is defined to the point where the jet center line velocity excess is dissipated but the density still differs in the plume region from the ambient environment (Lin et al. 1977). The momentum difference between jet region and the ambient water in the near field generates shear and consequently turbulence which is the main mixing mechanism within the initial portion of the near-field. Jet like mixing in this region increases the plume thickness and leads to full vertical mixing in shallow ambient water. The density gradient between the buoyant-jet and the ambient fluid also produces buoyancy forces due to unbalanced hydrostatic pressure, which also enhances the mixing process. This buoyant mixing mechanism is more significant further from the high momentum region near the outfall. In a stratified flow the buoyant plume will reach a level of equal density, whereupon it undergoes lateral buoyant spreading and reduced vertical mixing.

The "Far field" is the region where the plume is transported by the ambient current and mixed by the background turbulent diffusion. Therefore this region is also known as the passive diffusion region. The far field mixing time scale varies from the hours to days and its length scale is thousands of meters (Nekouee et al. 2013). The dilution rate in this region is much slower than the near field (Roberts 2013). The unsteady nature of tidal currents as well as wind generated waves influence mixing in this region, which makes the coastal mixing process complicated in the far field. Far field mixing can be modeled using Eulerian or Lagrangian approaches (Roberts 2013). The Eulerian approach estimates the mass concentration of the substance of interest (tracer, temperature or salinity) by solving the 3D advection diffusion equation in a fixed coordinate system. Lagrangian methods solve the advection-diffusion equation by following a moving particle with a specific characteristic (mass, temperature, etc) in a

moving coordinate system. The particles are advected by the local current which is determined by direct measurements or by a hydrodynamic sub-model and the turbulent diffusion is modeled by adding the random velocity added to the deterministic velocity (Roberts 2013). A detailed discussion on Lagrangian methods can be found in Israelsson *et al.* (2006 ).

Surface outfall flow regimes are generally classified as: free jets, shoreline-attached jets, wall jets, and upstream intruding plumes (Jones 1996, 2007) (Fig. 2.2). Nekouee et al. (2013) further improved the classification scheme by considering the wind effect on the plume shape in the surface outfalls with large aspect ratio (Fig. 2.3). Abessi et al. (2012) also added the classification criteria for negative buoyant surface outfalls (Fig. 2.4).

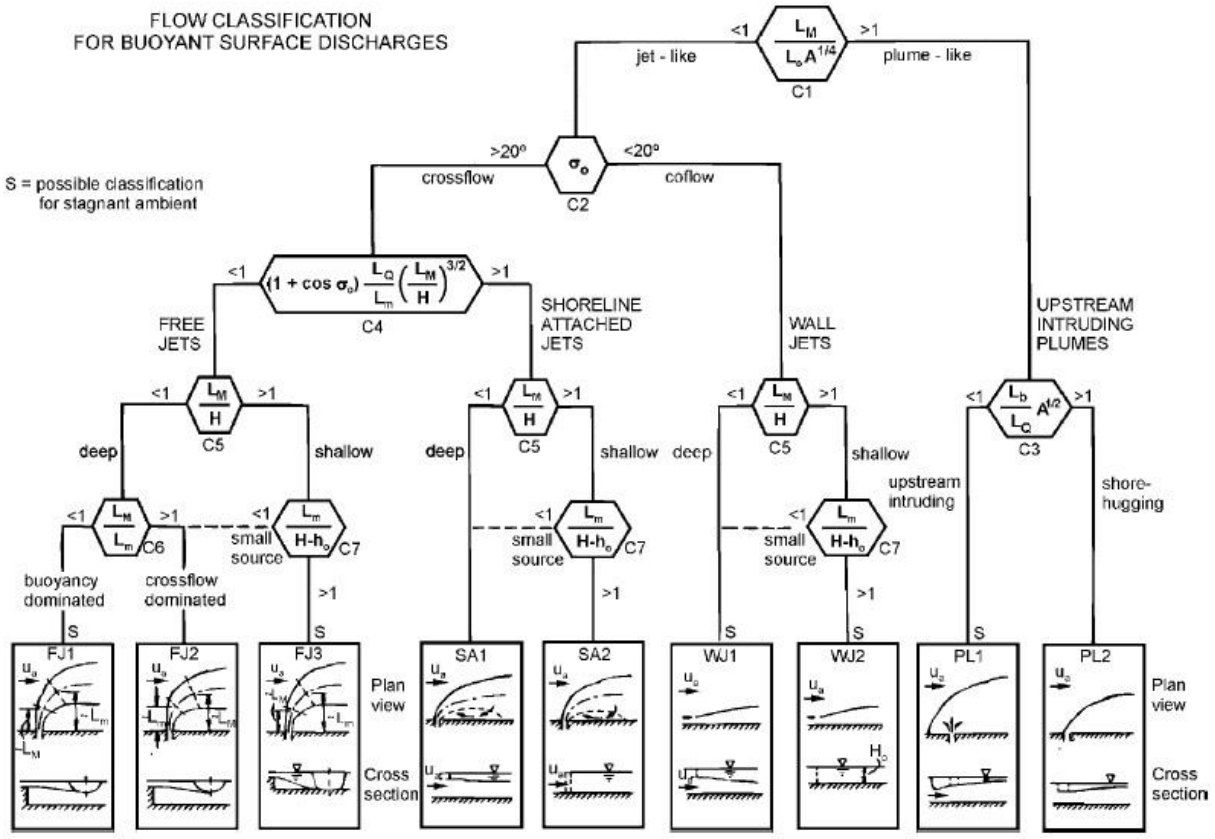


**Figure 2.2 The classification scheme for surface discharge of positively buoyant effluents (from Jones et al. 2007)**

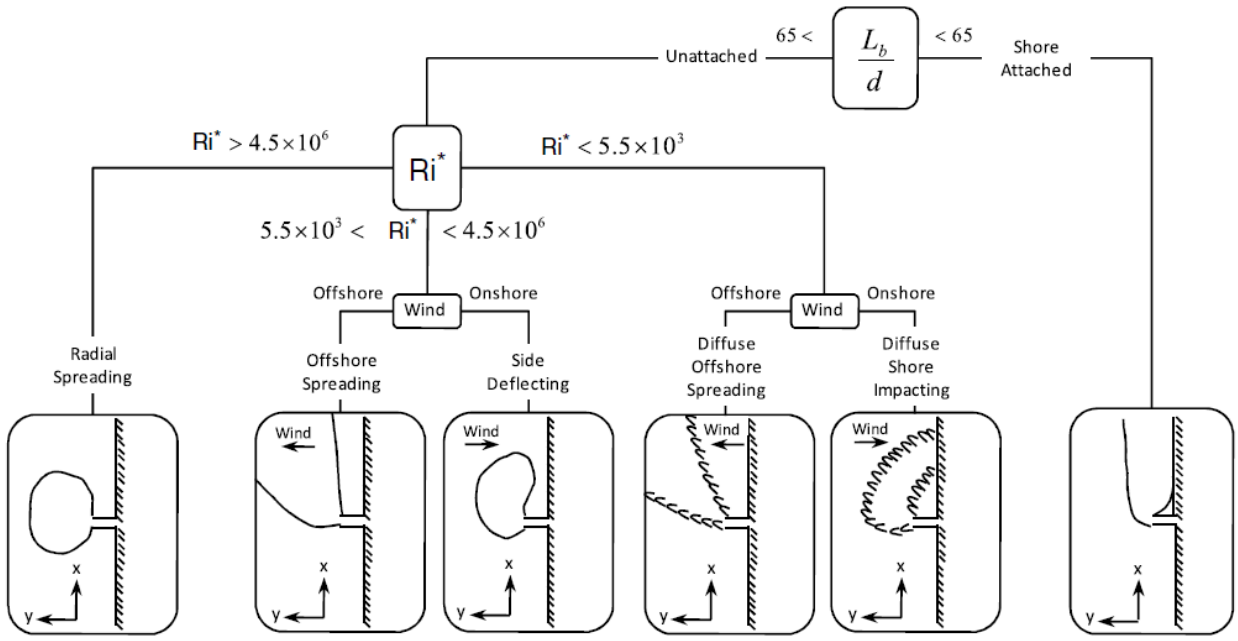


**Figure 2.3 Proposed surface buoyant plumes classification (Nekouee et al. 2013)**

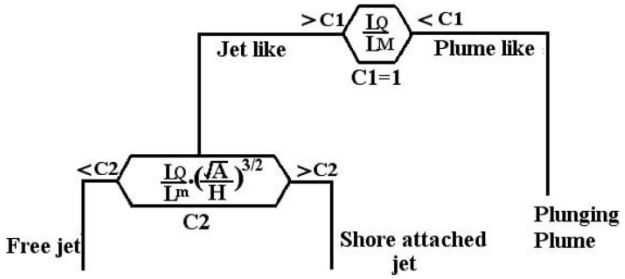


**Figure 2.3 First level of classification scheme is surface discharge of negatively buoyant flows (Abessi et al. 2012)**

Two transition zones can be defined in the surface buoyant jets (Jirka 2007). The first transition occurs within the zone of flow establishment where the relatively uniform top hat shaped velocity distribution is transformed to a sheared jet-like Gaussian shaped profile. The entrainment mechanism within this region is due to the stream wise or azimuthal shear (Jirka 2004). As the jet gets further from the source it is weakened due to the momentum diffusion (Jirka et al. 1981) and the second transition zone begins. This is the region in which jet-like behavior transitions to plume-like behavior and the vertical entrainment is inhibited and the buoyancy spreading dominates the mixing process. This will result in a sharped-edged vertical profile along the edge of the plume, which eventually reaches a uniform "top hat" shape and

forms a horizontally spreading density front (Nash and Jirka 1995) that separates the plume warm region from colder ambient water (Hunt et al. 2001) and uniform conditions in the lateral direction (Jirka 2007). A detailed discussion on frontal entrainment of surface buoyant jets can be found in (Lukentina and Imberger 1987).

The entrainment mechanisms in this region are summarized by Akar and Jirka (1994) as buoyant damping of vertical entrainment, frontal entrainment, and interfacial entrainment at the plume base.

The near field outfall behaviour can be addressed by the discharge properties such as discharge velocity $U_0$, discharge channel width $b_0$ , depth $h_0$ and channel cross-sectional area $a_0 = b_0 h_0$, discharge density $\rho_0$ and the discharge angle relative to the channel direction $\sigma_0$. In a general designation, these parameters are defined as the initial volume flux ($Q_0 = U_0 a_0$), momentum flux ($M_0 = U_0^2 a_0$) and buoyancy flux ($J_0 = U_0 g_0' a_0$). The initial buoyancy acceleration $g_0' = (\Delta \rho_0 / \rho) g$, is calculated from the initial density difference $\Delta \rho_0 = \rho_a - \rho_0$ , where $\rho_a$ is the average ambient density and $g$ is gravitational acceleration. Ambient velocity $u_a$, water depth $H$ and distance along the jet trajectory are ambient properties that affect the near field flow regime and mixing pattern (Jirka 2007).

In order to simplify consideration of the above mentioned parameters in the mixing process, some length scales are defined using dimensional analysis to represent the dynamic discharge quantities and the outfall interaction with the ambient water (Jones *et al.* 2007). Discharge length scale $L_Q$ defines the extension of the region where flow characteristics are greatly influenced by channel geometry,

$$L_Q = \frac{Q_0}{M_0^{\frac{1}{2}}} \qquad \textbf{(2.1.1)}$$

This parameter is used to define the extension of the zone of flow establishment, which is generally small and insignificant on the overall flow pattern. It is also measured against the jet to the plume length scale (introduced in the following), to determine the upstream intrusion.

The relative importance of the initial momentum and buoyancy flux is measured with the jet to plume length scale $L_M$,

$$L_M = \frac{M_0^{3/4}}{J_0^{1/2}} \qquad \textbf{(2.1.2)}$$

This length scale indicates the extension of the region where the jet mixing process is dominated by momentum as opposed to buoyancy induced lateral mixing. This length scale is independent of the ambient water properties and defines the balance between unsteady jet mixing and the buoyant spreading mechanism.

The jet to cross flow length scale defines the relative significance of the initial momentum to the ambient cross flow as,

$$L_m = \frac{M_0^{1/2}}{u_a} \qquad \textbf{(2.1.3)}$$

where $u_a$, is the ambient current velocity. This length scale can be used to indicate if the flow is weakly or strongly deflected.

The ratio of the initial buoyancy flux to the ambient cross flow is defined with plume to cross flow length scale $L_b$.

$$L_b = \frac{J_0}{u_a^3} \qquad \textbf{(2.1.4)}$$

As previously mentioned, an upstream intruding plume is one of the main surface outfall categories defined by Jones (1996, 2007). The $L_b$ length scale is used to determine upstream spreading extension.

The bulk Richardson number ($R_i$) and the densimetric Froude number ($F_r$) are commonly used in surface discharge mixing studies. The bulk Richardson number is a dimensionless parameter,

$$R_i = \frac{\Delta\rho g h}{\rho_a u^2} \qquad \textbf{(2.1.5)}$$

where $\Delta\rho$ is the average local density difference between jet and the ambient fluid, $h$ is the jet local thickness and $u$ is the average local jet velocity. This parameter represents the ratio of the vertical stability and the vertical shear. Stratification generally supresses the vertical turbulence and consequently vertical entrainment occurs in high $R_i$ values (Ellison and Turner 1959). The densimetric Froude number ($F_r$) is the ratio of the inertia force to the buoyancy force and is defined as,

$$Fr = (u / \sqrt{\left(\frac{\Delta\rho}{\rho_a}\right) g h}) \qquad \textbf{(2.1.6)}$$

and is related to $R_i$ by,

$$R_i = \frac{1}{Fr^2} \qquad \textbf{(2.1.7)}$$

Chu and Jirka (1986) suggested the value $F_r$=2.5 for distinguishing between jet like and plume like behavior. They reported that for $F_r$<=3 the discharge can be treated as a plume. Jirka et al. (1981) used local Froude number to express the local influence of the buoyancy on jet entrainment and profile shapes.

Near field mixing models can be categorized as length scale models, jet integral models, and numerical models (Jones et al. 1996). Length scale models use experimental or field measured data to develop an empirical expression to predict the average dilution rate, shape and trajectory of the jet/plume. Length scale models are based on the empirical expression of the plume parameters and are often derived from laboratory studies (Roberts et al. 1989 a,b,c). Multiple studies have used detailed measured data and theoretical and statistical analysis to develop formulae for predicting mixing under different initial discharge and ambient conditions. Jirka et al. (1996) combined various research results in this regard and developed the CORMIX model. This model is based on the flow classification which is the most

appropriate qualitative description of the outfall, and uses formulae proposed in other experimental studies to predict the dilution in analogues cases.

The jet diffusion theory governing equations are based on the conservation relationships for mass, momentum and energy (Abraham 1972). However for a turbulent flow, the number of unknowns is more than the equations which leads to the closure problem. This is the main idea behind using the entrainment concept in the governing equations to obtain a closed system of equations. Jet integral models are based on solving the ordinary differential equations and are derived by integrating the jet properties like momentum, buoyancy and mass fluxes across the section (Jirka et al. 1981). These models apply the influence of different turbulent sources by the empirical entrainment coefficients in the conservation of mass, buoyancy and momentum fluxes. Integral models apply the effect of different mixing sources such as wind, turbulent mixing, buoyancy and; interfacial and drag forces as entrainment coefficient in the simplified governing equations. Morton et al. (1956) and Townsend (1966) used the entrainment constant concept to model the turbulence mixing. In one of the earliest studies, Morton et al. (1956) employed the entrainment rate in an integral model to study the mixing of a simple plume in a stratified environment. Shirazi and Davis (1974), Jones et al (1996) and Jirka (2004, 2006, 2007) are some examples of the integral models developed for modelling outfall mixing. The entrainment rate is introduced to represent different phenomena that are expected to affect the mixing rate, such as turbulence, wave, wind stress, etc (Akar and Jirka, 1995; Jirka 2007). The concept of entrainment can be expressed as,

$$V_e = E_s U_m \qquad \textbf{(2.1.8)}$$

where $V_e$ is the entrainment velocity at plume edges, $U_m$ is the plume centerline velocity and $E_s$ is the entrainment coefficient and is derived using experimental or field data. The entrainment is assumed to be normal to the jet trajectory. This equation is valid only for low velocity ambient flow conditions (Lin et al. 1977). The spreading coefficient is another parameter that represents the rate of change in plume width along the jet trajectory. This parameter has a similar concept as the entrainment velocity, and can be used instead to achieve a closed system of equations. Jirka *et al.* (1975); and Stolzenbach and Harleman (1971)

showed that there is a linear relationship between entrainment velocity and spreading coefficient. For a heated surface discharge, the entrainment process is generally divided into lateral entrainment (Hoopes e t al., 1968) and vertical entrainment (Stolzenbach and Harleman, 1971). The spreading coefficient and entrainment velocity are obtained by solving the continuity and momentum equations. The solution is based on the hydrostatic pressure distribution assumption and the buoyancy forces produced by the density gradient are balanced with the hydrodynamic drag forces. The total spreading process in either horizontal or vertical direction can be split to buoyant and non-buoyant components. The non-buoyant component is zero at the jet axis and increases linearly towards the jet boundaries.

Jirka (2007), developed a jet integral model to predict the near field of surface outfalls. He generally categorized the complex processes as pure jet mixing, buoyant entrainment damping and collapse motions, lateral density front formations, a propensity for internal hydraulic jump discontinuities, Coanda attachment processes, low pressure shoreline interaction and recirculation effects, heat buoyancy loss, and wind-induced mixing. The developed jet integral model was based on the implemented principles by Jirka (2004, 2006 ) for single port jets. He considered the contribution of each of these mechanisms separately in the entrainment *E* into the buoyant surface jet and applied each of them using the proposed equation for estimating entrainment from other experimental or theoretical studies (Parker et al.1987, Akar and Jirka , 1994).

The fate of an injected tracer injected is governed in the near field and far field by the 3D advection-diffusion equation (Elhadi et al. 1984),

$$\frac{\partial S}{\partial t}+u_x\frac{\partial S}{\partial x}+u_y\frac{\partial S}{\partial y}+u_z\frac{\partial S}{\partial z}=\frac{\partial}{\partial x}(\varepsilon_x\frac{\partial S}{\partial x})+\frac{\partial}{\partial y}(\varepsilon_y\frac{\partial S}{\partial y})+\frac{\partial}{\partial z}(\varepsilon_z\frac{\partial S}{\partial z}) \qquad \textbf{(2.1.9)}$$

where $S$ can be temperature, salinity or tracer concentration, $u$ is the velocity and $\varepsilon$ is the eddy diffusivity, $x$ and $y$ are the horizontal directions, $z$ is the vertical direction and $t$ is the time. The velocity field can be calculated from hydrodynamic sub-models (Dow et al. 2009) or can be generated from measurements (see Chapter four). The hydrodynamic models provide the velocity field by solving either

the full Navier Stokes equations or simplified forms such as hydrostatic (shallow water) models. The hydrostatic models assume a hydrostatic distribution for pressure in the vertical direction and are used in circumstances where the vertical acceleration is negligible. This simplifying assumption provides a more computationally efficient model. However, for the cases with high vertical acceleration, the hydrostatic assumption is not applicable. The vertical acceleration may be produced by a sudden change in the bathymetry or a strong source of momentum or buoyancy. In cases for which the vertical acceleration component is relatively small, the hydrostatic assumption for pressure distribution in the vertical direction is reasonable, and hence the hydrodynamic pressure can be neglected. However for cases with vertical acceleration, the hydrodynamic pressure cannot be neglected. Therefore, the hydrodynamic component of the pressure has to be calculated to provide a realistic flow behaviour. For each of the mentioned models, eddy diffusivity is obtained from the turbulence model of the hydrodynamic model (Delft3D-Flow User Manual).Eddy diffusivity ($\varepsilon_t$) is obtained from the eddy viscosity ($\nu_t$) according to

$$\nu_t = \Pr \varepsilon_t \qquad \textbf{(2.1.10)}$$

where *Pr* is the Prandtl-Schmidt number which range between (0.6-1) based on the substance of interest. Hydrodynamic models generally use the numerical approach for solving the mentioned governing equations. There are some other simplified approaches also proposed based on the analytical solution of the simplified form of the governing equations which will be discussed in the next sections.

The numerical models solve the advection-diffusion equation in which the eddy diffusivity is calculated from the turbulence model. The velocity field and the eddy diffusivity are the main required parameters in these models and are calculated using the hydrodynamic and the turbulence models respectively (Koziy et al. 1998). Due to the significant difference in the length and time scale, the near-field and far-field mixing are commonly simulated using separate models that are coupled. Regardless of the employed model in the near-field or the far-field, the coupling methods are generally categorized as one-way such as Zhang and Adams (1999) and Bleninger and Jirka (2004) or two-way coupling models. The two-way coupling

methods apply the full interaction between the near-field and far-field by excluding the entrainment element into the plume within the near-field extension of the far-field model and applying the near-field output as sources at the boundary of the near field and the far-field (Hamrick 1992; Choi and Lee 2007)

Numerical methods always introduce some numerical errors and impose higher computational cost to the model. Although recent computer advances have considerably increased the popularity of numerical models for mixing studies, the main difficulty in using these models in both near field and far field is their high computational cost as well as choosing the proper turbulence model and boundary condition. The turbulent eddies enlarge with distance from the discharge point. Therefore, a finer grid is required in the near field region to resolve the near field eddies. This also imposes a higher computational cost to the model and is the main reason behind using the simplified models for the near field modelling as well as developing the coupling approaches to link the simplified near field models and the large scale far field models (Zhao 2012).

### 2.2 Coastal mixing

The mixing characteristics of buoyant coastal outflow has been investigated in various theoretical (Luketina and Imberger 1989, Hetland and MacDonald 2007), experimental (Lal and Rajaratnam 1977) and field (Luketina and Imberger 1987) studies. McCorquodale (2007) provided a comprehensive review of the theoretical, experimental, numerical, and field research on stormwater discharges with jet-plume surface outflows and interaction with flow in rivers and coastal waters. Specific features of coastal mixing studies include the mixing sources, such as tidal currents, waves and wind, which affect the dynamics and the mixing pattern of the plume. The wind can influence coastal mixing through wind generated waves or wind driven currents. Coastal water waves are generally either local random wind generated waves with various wave height and frequency or regular swell waves with lower frequencies generated by distant winds

or storms. Density stratification of the ambient receiving water can also be an important consideration. Turbulence is the main source of mixing and can be produced by fluid shear, friction or buoyancy (see Appendix A in Chapter 7). In a stratified flow the buoyancy production term of turbulence is negative. Therefore, the buoyancy term suppress the turbulence and consequently weakens the mixing process (Johnson et al. 1989).

The summary of the various experimental, numerical and theoretical studies shows that the wave oscillatory motions enhance the jet entrainment rate and consequently jet spreading and the dilution rate (Xu et al. 2014). Mori and Chang (2003) introduced the wave-to-momentum ratio ($R_M$),

$$R_M = \frac{gA^2}{4b_0 u_0^{\,2}} \qquad \textbf{(2.2.1)}$$

where $A$ is the wave amplitude, g is gravity, $b_0$ is jet radius and $u_0$ is jet velocity. They categorized the jet oscillations under wave interaction into three types of symmetric or asymmetric oscillations with a continuous jet center line as well as asymmetric oscillations with a discontinuous jet center line. They reported that as the wave amplitude increases the jet oscillation pattern changes from symmetric to asymmetric and finally becomes discontinuous.

Coastal buoyant outflow attachment to the shore is an important issue from the environmental point of view especially along recreational coasts. Nekouee et al. (2013) used a specific Richardson number that was a function of wind velocity to predict the coastal buoyant plume attachment to the shore line.

Wind driven current can also affect the jet trajectory and enhance the vertical mixing as a result of upwelling and downwelling processes. Whitney and Garvin (2005) introduced the wind strength index ($W_s$) as the ratio of the wind-driven and buoyancy driven velocity scales that determine the wind effect on the plume shape for the Delaware Coastal estuary buoyant outflow. Walker et al. (2005) also reported trapping the plume around the river mouth in the case of onshore wind.

In surface wall jet discharge in shallow water, the investigated case in this study, jet entrainment is restricted by the presence of side solid wall and bed. The jet is initially attached to the bed in the region close to the outfall. This is the region where the inertial forces dominate and is referred as the turbulent core (Safaei 1979). Linear spreading is observed within this region as the result of momentum exchange between the jet and the ambient water. This mechanism is also known as the jet mixing. Flowing over the mild slope bed, the jet reaches to the maximum depth ($h_{max}$) and then detached from the bed. From this point turbulence and entrainment reduces greatly, buoyancy spreading controls the mixing, and the plume thickness reduces until it obtains the uniform transverse distribution. Due to the difference in the mixing mechanism, predicting the detachment point is a critical issue. Estimating the detachment point has been investigated in different studies (Baddour and Chu 1975, Weigle et al. 1976, Safaei 1979). In one of the more recent studies, Atkinson (1993) applied the physical mixing process in solving the momentum equation and proposed a numerical approach for determining the detachment point.

Recent advancement in remote sensing technology has greatly enhanced the popularity of employing remote sensing approaches in mixing studies, especially in the regions where conducting field survey is not possible due to the access difficulties. The idea of using remote sensing to monitor ocean outfalls dates back to the 1980's (Davis et al. 1985 and 1987). These approaches are based on measuring the volume reflectance by remote sensing sensors. The remittance may be in the visible, near infrared or thermal infrared wave lengths. As the remote sensing sensors only measure the reflectance, they are normally calibtated with field measurements. Remote sensing methods vary with respect to their utilized sensor. Employing the thermal imaging camera (Ali et al. 2011), ocean surface current radar (OSCR) (Chin et al. 1997) and airborne photography (da Silva et al. 2001) are some examples of using different remote sensing methods to identify the fate of discharges in rivers and coastal waters. Davies et al. (1997, cited in Torgersen et al. 2001) used thermal infrared (TIR) imagery to map the cooling-water discharge from a power plant.

## 2.3 River mixing

The goal of river mixing studies is generally to estimate the longitudinal and transverse dispersion coefficient or to investigate the effect of different parameters such as river discharge, bed roughness, ice cover, etc. on the mixing potential. The longitudinal and transverse dispersion coefficients are both based on the Fick's law and describe the elongation of the tracer cloud in stream wise or transverse direction, respectively (Fischer 1979).

Knowledge of the mixing potential of a river can greatly help in developing environmental plans. Transverse mixing has greater importance than longitudinal mixing when dealing with pollutant mixing in rivers. In a general classification, Baek and Seo (2013) categorized the method for estimating the mixing as observing and estimating methods.

The observing methods are based on tracer study results from field or laboratory work. Several observing mixing methods have been proposed in the literature such as standard method of moments (Yotsukura and Sayre, 1976) and general method of moments (Beltaos, 1980; Rutherford, 1994), Eqs. (4.2.8 and 4.2.9) , or more sophisticated ones like the cumulative discharge method (Yotsukura and Cobb, 1972;Yotsukura and Sayre, 1976), routing (Baek and Seo 2010) and stream tube routing (Seo et al. 2010). The genetic algorithm (GP) is another approach which has been used in some studies for estimating transverse mixing coefficient (Azamathulla and Ahmad 2012) or longitudinal mixing coefficient (Etemad-Shahidi and Taghipour 2012). These methods are based on the simplified form of the 3D advection diffusion equation and assume a uniform and steady flow condition in the river.

Estimating methods use the mixing coefficient provided from observational methods and propose practical formulae that use hydraulic and geometric parameters for estimating the average longitudinal or transverse dispersion coefficient. These empirical equations use the bulk flow parameters for estimating the average transverse mixing coefficient. Relatively simple formulae have been proposed to estimate mixing coefficients in straight channels (e.g., Fischer et al. 1976). These formulae consider only the bed

shear turbulence effects on mixing. They use depth as the length scale and a representative maximum eddy size to drive mixing.

Secondary flows are generated in curved channels and have a great influence on enhancing the transverse mixing. Various studies have been conducted to improve the understanding of secondary flow structures (Blanckaert 2011; Kashyap et al. 2012) and their influence on the transverse dispersion in curved channels. In a straight channel secondary currents are small. As the flow enters a bend the variation in centrifugal force develops the secondary currents with a transverse flow toward the outer bend in the upper portion of the section and return flows along the bed. In a bend with uniform curvature, transverse velocities increase with distance downstream until the secondary flow becomes fully developed and the velocities remain constant until channel curvature changes. When the channel becomes straight again, the secondary currents decrease with distance and eventually dissipates. In meandering channels, shape, width to depth ratio, and surface roughness of the channel affect the size, strength, number, and arrangement of vortex structures (Aydin 2009).

Boxall and Guymer (2003) found the maximum transverse mixing coefficient values in the regions of strong secondary circulation, just downstream of the bend apex, and minimum values in the straighter regions. The generated secondary current at the bends of meandering channels causes transport of momentum and mass between the areas of low streamwise velocity near the inner bank and of relatively high velocities near the outer bank. This enhances the mixing over the cross-section.

Fischer (1975), Liu (1977), Iwasa and Aya (1991), Seo and Cheong (1998), Koussis and Rodriguez-Mirasol (1998), Seo and Baek (2004) are some examples of equations developed for estimating longitudinal mixing coefficient in meandering rivers. The influence of secondary flow in meandering flows is considered by employing the sinuosity (Jeon et al. 2007) or using cross section width instead of depth as the length scale (Baek and Seo 2011, Sayre 1979). However, all of them use shear velocity as the velocity scale. The performance of the proposed formulas in general cases depends on the number and diversity of the data sets used for developing them.

# Chapter 3:

## *In situ* spatially distributed field measurements of transverse dispersion of a wastewater effluent in an extended natural meandering river reach for estimation of the full mixing length

**Published in the Journal of Hydraulic Research:** DOI:10.1080/00221686.2014.950611, 2014

**Authors:** Abolghasem Pilechi, Colin D. Rennie, Majid Mohammadian, David Zhu

### 3.1 Abstract

A new *in situ* technique is introduced and tested for field tracer study in natural meandering rivers. Real-time position data from a global positioning system (GPS) was integrated with *in situ* fluorometer data, thereby providing a 2D spatial distribution of the tracer concentration. The method was used in an intensive tracer field survey over a 83km reach of the North Saskatchewan River downstream the Capital Region Waste Water Treatment Plant (WWTP). The objectives of the study were twofold. The primary objective was to determine the downstream distance required to achieve full mixing of the effluent. Our second goal was to provide a reliable and accurate tracer data set for a highly extended meandering river which can be used in other numerical and analytical mixing studies. Rhodamine WT was injected as the tracer at the outfall of Capital Region WWTP and the tracer concentration data was measured across a total of 17 sections using an *in situ* fluorometer. Hydrodynamics data was also collected simultaneously by measuring stream-wise water velocity and depth using an acoustic Doppler current profiler (aDcp). The measured average depth and stream-wise velocity for the surveyed reach were 1.36 m and 0.6 m/s, respectively. The Rhodamine WT concentration reduced gradually along the river path from 100 ppb at the right-bank outfall to 0.83 ppb in the last surveyed section 83 km downstream of the outfall. Despite the massive survey effort over many river km, full mixing to the point of uniform concentration across the section was not observed up to 83 km downstream the outfall. The full mixing length for this surface bank

outfall at the observed low flow condition was inferred to be 130 km. The employed technique effectively improved the understanding of mixing patterns in complex flows by providing tracer and hydrodynamic data with high spatial and temporal resolution.

### 3.2 Introduction and literature review

Understanding of contaminant mixing in natural meandering rivers is important for management of environmental and water resources, with consequences for drinking water, irrigation, and recreational uses. Dissolved oxygen (DO) is one of the most effective parameters in aquatic life. The level of DO in a flowing stream is highly influenced by Biochemical Oxygen Demand (BOD) loading introduced by wastewater effluent discharged into rivers. This paper reports a detailed study of transverse mixing of a wastewater effluent in a natural meandering river.

Summarising the reported transverse dispersion coefficient results from various previous field and laboratory studies in straight, meandering, ice-covered, and sinuous natural channels, Rutherford (1994) suggested the value of 100-300 times the channel width as the approximate river reach length required for transverse full mixing downstream of a point source near the middle of a river section. For a source near the bank, the value should be increased four times. In mixing studies, the transverse mixing distance ($L_z$) is used as the distance from the outfall where tracer becomes fully mixed across the channel. The fully mixed condition can be assumed when the ratio of minimum to maximum concentration ($P_m$) reaches the range between 0.9-0.98 across the channel (Rutherford, 1994). Considering $P_m = 0.98$ and assuming a monotonic decrease in concentration gradient in relation to increased distance from the source, Rutherford (1994) suggested $L_z = 0.536vb^2/k_s$ in the case of bank outfalls, where $v$ is the river average velocity, $b$ is the river width, and $k_s$ is the bed roughness. The other important parameter is the distance downstream of the source where the tracer reaches the opposite bank ($L_c$). This parameter has been termed the cross distance by Holley *et al*. (1972). Rutherford (1994) suggested $L_c = 0.0546vb^2/k_s$ as the distance from the bank source where tracer concentration at the opposite bank reaches 2% of the near-bank concentration.

It is generally accepted in the literature that the transverse mixing coefficient in a river is affected by several main parameters, such as river geometry, depth, discharge, width, ice cover, and shear velocity (Zhang and Zhu 2011). Much effort has been expended to identify the level of importance of these parameters in the transverse mixing process. Lau and Krishnappan (1981) summarised that higher sinuosity in a meandering channel caused increase in transverse mixing. In one of the most recent field studies Zhang and Zhu (2011) observed the effect of flow rate and ice-cover on transverse mixing in a meandering river. They found that transverse mixing coefficient increased linearly with the flow rate. The ice-covered condition was also found to have a negative effect on the transverse mixing process.

Transverse mixing in rivers is due to molecular diffusion (usually insignificant), turbulent diffusion, and advection due to secondary currents (Gualtieri 2009). In a numerical or analytical mixing model, a dispersion coefficient is used to account for processes that are not directly modeled. Dispersion thus accounts for mixing resulting from velocity gradients "i.e., velocity shear" over the depth and width. In a 2D model, dispersion accounts for both turbulent and molecular diffusion processes. Advection due to secondary currents increases the rate of mixing by moving the particles in opposite directions at different depths (Fischer, 1969).

While many hydraulic and contaminant fate numerical models have been developed that consider each of these processes, prediction of turbulent dispersion, i.e., mixing of pollutants due to turbulence, is challenging. In general, a mixing coefficient is required to quantify this process. The mixing coefficient can be estimated using either analytical or numerical approaches (Nikiema *et al*. 2007), but both of these approaches are ultimately driven by experimental data.

Analytical methods can be defined as either observational or predictive methods (Jeon *et al*. 2007), both of which require reliable sets of tracer and hydraulic data to verify their performance. The observing methods estimate mixing coefficients directly from hydraulic and tracer data that indicate dispersion of the tracer in the channel. Some of the observing methods are relatively simple such as the standard method of moments (Yotsukura and Sayre, 1976) and Generalized Methods of Moment (Beltaos, 1979 and Rutherford, 1994), while others are more complicated such as the cumulative discharge method

(Yotsukura and Cobb, 1972; Yotsukura and Sayre, 1976). Predicting methods such as Fischer (1969), Bansal (1971), Gharbi and Verrette (1998) and Jeon *et al.* (2007) generalize observational results to provide a formula for estimating the average mixing coefficient. Analytical approaches employ simplifying assumptions such as uniform velocity and depth throughout the channel. These simplifying assumptions may lead to inaccurate predictions, especially where the region of study is a highly extended long reach. The desire to minimize errors in estimation of mixing coefficients has led researchers to utilize numerical approaches (Parker *et al.* 2012). Several turbulence closure models are available for estimation of the mixing coefficient, such as the $k$-$\varepsilon$ model (Rodi, 1993). However, direct estimation of the mixing coefficient in rivers by field measurement is usually necessary for validating such models.

To obtain sufficient data to estimate mixing coefficients, several experimental tracer studies have been performed in controlled laboratory conditions. In one of the earliest experimental studies, Elder (1959) found that the concentration distribution from a point slug injection of tracer follows a Gaussian distribution. He proposed $E_z=\beta HU^*$ for estimating the transverse mixing coefficient, where $E_z$ is the transverse mixing coefficient, $H$ is the mean channel depth, $U^*$ is the average shear velocity and $\beta$ is the empirical coefficient which was found equal to 0.23 in that study. Of the laboratory studies carried out since then, some were conducted in straight channels (e.g., Miller and Richardson,1974; Holly, 1975; Lau and Krishinapan, 1977; Nokes and Wood, 1988). On the other hand, several studies have been conducted in meandering channels, focusing on the influence of channel curvature on mixing (Fischer, 1969; Chang, 1971; Boxall and Guymer 2003).

Although laboratory studies have been generally more popular, in some cases their controlled conditions may also cause discrepancy between laboratory and field results (Fischer, 1969). This is attributed to the uncertainties in scaling law or irregularities in river geometry, depth or side walls which cannot be taken into account properly in laboratory studies. One of the earliest field transverse mixing studies was conducted by Glover (1964) in the Columbia River. Similar to laboratory experiments, field studies have been conducted on straight (Fischer, 1969) or meandering channels (Yotsokura, 1970). The curvilinear flow in meandering channels produces transverse advection and secondary circulations (Blanckaert,

2011; Kashyap *et al.* 2012) which enhance the transverse mixing. This effect and its dominance was investigated in various field studies (Lau and Krishnapan, 1981; and Seo *et al.* 2006). Conducting a laboratory experiment in a meandering channel, Lau and Krishnapan (1981) suggested using stream sinuosity to consider the effect of secondary currents in transverse mixing. Seo *et al.* (2006) concluded that secondary currents enhance transverse mixing in meandering channels and are directly related to the stream sinuosity and the ratio of width to depth in meandering channels.

Field tracer studies have also differed in the extent of the study region. Some of them have focused on the mixing pattern in the intermediate region from an outfall (Dow *et al.* 2009), while others have focused on far field mixing patterns (Zhang and Zhu 2011). All tracer studies from the earlier ones like Elder (1959) to more recent ones (Seo *et al.* 2006) were conducted to provide a method or formulation which can present the mixing mechanism more accurately. Rutherford (1994) gathered different experimental and field work data and summarised them in non-dimensionalised graphs which are very useful for estimating the mixing.

In all of the mentioned experimental or field tracer studies, water sampling methods have been used for measuring tracer concentration. The sampling methods introduce time lags in the data acquisition process especially in field measurements, which can be a source of error when the data is post-analyzed. These methods cannot be used for real-time monitoring, and may create significant problems in studying dispersion in water bodies. Recent developments in field equipment, such as employing more accurate global positioning system (GPS) and acoustic Doppler current profiler (aDcp) instruments, have improved the quality of field data and increased the tendency towards conducting field studies. For example, vertical velocity profiles measured with an aDcp have been used in recent studies to estimate the longitudinal dispersion coefficient (Carr and Rehmann 2007; Shen *et al.* 2010).

In recent years the limitations of sampling methods have also been reduced by the advent and recent employment of *in situ* fluorometers [*In situ* fluorometry has been used to study spatial plume dynamics in lakes (e.g. Goudsmit *et al.* 1997 ) and oceans (e.g. Ledwell et al. 1993)]. In one of the earliest studies, Katz *et al.* (2003) used an *in situ* fluorometer to study the mixing field of the discharged waste from a

vessel into its wake zone. Later, Hunt *et al*. (2010) used an *in situ* fluorometer to study the initial dilution, near field and far mixing of the sewage outfall plume in Boston harbor. Rowiński *et al*. (2008) also used an *in situ* fluorometer to investigate mixing and transport process in a 90-km reach of the Upper Narew River in the northeast of Poland. In Rowiński's study, the *in situ* fluorometer was mounted at a fixed position in the middle of the surveyed sections. Therefore, the fully 2D spatial distribution of the tracer concentration was not provided.

Studying the full mixing length of the natural meandering rivers with small mixing coefficients has always suffered from logistical difficulties which may negatively affect the output of the study. The full mixing in these cases occurs far from the discharge point. Therefore the steady injection of the tracer during the field work may not be applicable due to the massive amount of required tracer. In these rivers, the full mixing condition is not commonly reached within a one day of field work. Finding the plume in the next day of field work is an essential task which greatly affects the accuracy of the study. Therefore, the accuracy of the traditional sampling methods, which suffers from the time lags in the data acquisition process, depends directly on correctly locating of the plume in the river. This is more important in the cases for which the field campaign is continued for several days.

The error in estimating the travel time of the plume may lead to inaccuracy in estimating the mixing coefficient or the mixing pattern of the plume along the river path. Therefore, having an extensive set of tracer and hydrodynamic data with high spatial and temporal resolution is essential in understanding the mixing pattern of the plume in an extended region of interest with complex flow patterns. The novel contribution of this paper is to integrate real-time position data into both *in situ* fluorometer and aDcp data collected at each surveyed point in the river, and thereby provide a fully 2D spatial distribution of the tracer concentration in a natural meandering river. Due to the wide cross section of the river in this study as well as the outfall location which was on the bank side, providing a spatial distribution of the tracer concentration is critical for understanding the behavior of the plume along the river path. The main objective of this study is to introduce a new technique for tracer field study by using the latest technology in field measurement and to show the effectiveness of this technique for studying the mixing pattern of

extended natural meandering rivers. Furthermore, the observations are used to infer the stream path length required to achieve full mixing of the effluent.

In this study, Rhodamine WT was injected as the tracer at the outfall of Capital Region Waste Water Treatment Plant (WWTP) which disposes its treated wastewater effluent into the North Saskatchewan River downstream of the City of Edmonton, Canada. The tracer concentration was then tracked using an *in situ* fluorometer along an extended 83 km long reach of the river from a boat moving across and along the river. The hydraulic characteristics of flow, including depth averaged velocity and bed elevation, were also collected simultaneously using an aDcp. The shear velocity, as one of the most effective parameters on the mixing coefficient, was also calculated from collected velocity profiles.

In the next step, a filtering process was performed on the collected data. The filtered data was then mapped and interpolated with the kriging method. The mean value of interpolated data was then calculated as the representative of that parameter in the surveyed sub-reach.

This study provides reliable data sets of the basic hydraulic parameters as well as tracer results, which can be used in different hydraulic and mixing studies. For example, the summary of data presented herein is used in Chapter four to develop a numerical model to simulate mixing of natural conservative substance in a meandering river. The model employs an orthogonal stream tube coordinate system and considers the effect of fluctuating river discharge in simulating the mixing pattern in the river. The dispersion coefficients were also estimated using the standard and general method of moments for the first quarter of the study length and the results were compared with the numerical model. The mixing coefficient was estimated in different surveyed sub-reaches along the river path and the averaged dispersion coefficient was calculated for the total surveyed reach.

This paper is prepared as follows. First, the methodology for conducting the field work is explained in detail. Subsequently, in the post processing section, the methods used for filtering and mapping the collected data are discussed. In the results section, the output tracer concentration, water velocity, flow depth, and shear velocity across several sections in the extended reach are presented. A detailed analysis


**Figure 3.1 Capital Region WWTP outfall; b) site location (adopted from Google Earth)**

of velocity, depth, and tracer concentration distributions in a particular meander bend is also conducted. A discussion of the observed mixing patterns follows, including an assessment of the influence of channel morphology on mixing. The paper concludes with a summary of the presented results, and limitations of the study.

### 3.3 Field work

The field work was started by injecting tracer at the outfall location of Capital Region WWTP, which is the fourth-largest wastewater treatment facility in Alberta, Canada. The plant has a surface outfall located at the right bank side of the river, facing downstream (Fig.3.1) at 53° 38.297'North (latitude) and 113° 18.489' West (longitude).

Following government of Alberta environmental guidelines, in this study Rhodamine WT was used as a tracer of the wastewater effluent in the river. The tracer was also diluted with an equal volume of methanol in order to produce a neutrally buoyant mixture. The density of Rhodamine WT is 1.26 g/cm$^3$, thus it was diluted with an equal volume of methanol with 0.791 g/cm$^3$ density to produce a neutrally buoyant mixture with lower viscosity and surface tension characteristics. This also minimized the effect

of buoyancy on transverse mixing rate. In addition, the injection rate was chosen so that the concentration of Rhodamine WT did not exceed 10 ppb at the full mixing condition or at any withdrawal point.

In most cases the outfall of a wastewater treatment plant acts as a steady source of pollution to the receiving river. Ideally, to study the effluent plume from source to the point of far field full mixing, tracer should be injected continuously into the source at a steady rate. However, for large rivers this requires an enormous quantity of tracer. In this study, the tracer was injected for 13 hours on October 26, 2011, at a steady rate of 64 mg/s using a peristaltic pump. This created a tracer slug that could be tracked as it mixed into the river. The mixing pattern was tracked from a boat moving across and along the river using an *in situ* flourometer. The Rhodamine plume was traced for a period of three days (October 26-28, 2011) by surveying a total of 17 sub-reaches over a total distance of 83km along the river path. As described below, survey data within each sub-reach was projected onto a single section (Fig. 3.2). The spatial location of the surveyed sections as well as the surveying dates are provided in Table (3.1).

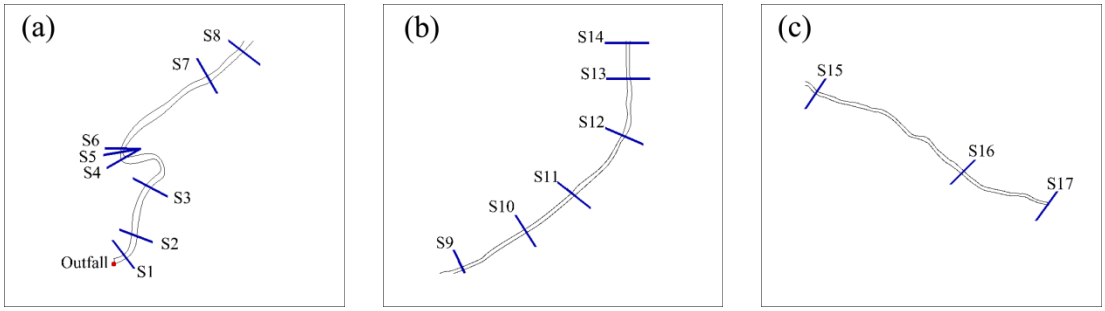


**Figure 3.2 Sections surveyed on a) October 26; b) Sections surveyed on October 27; c) Sections surveyed on October 28**

**Table 3.1Summary of the surveyed section information**

| Date | Section | Distance from Outfall (km) |
|---|---|---|
| October 26 | *S1* | 0.74 |
| | *S2* | 2.3 |
| | *S3* | 3.5 |
| | *S4* | 6.5 |
| | *S5* | 6.5 |
| | *S6* | 6.5 |
| | *S7* | 10 |
| | *S8* | 12 |
| October 27 | *S9* | 39 |
| | *S10* | 44 |
| | *S11* | 47 |
| | *S12* | 52 |
| | *S13* | 55 |
| | *S14* | 59 |
| October 28 | *S15* | 66 |
| | *S16* | 78 |
| | *S17* | 83 |

The innovative aspect of this study is real-time tracer data collection and data display with the *in situ* fluorometer. Real-time *in situ* measurements allowed for much higher sampling intensity, thus the plume was characterized in much greater detail than was possible with conventional water sampling. Furthermore, real-time display of tracer concentration along the survey path allowed for identification of the plume location while in the field, which allowed for on-the-fly optimization of the survey path to best characterize the effluent plume. This greatly increased the utility of the collected data.

As previously mentioned the *in situ* fluorometer was used in another study by Rowiński *et al*. (2008) to investigate mixing and transport process in a river. However, the fluorometer was stationary at the surveyed sections in Rowiński's study. Integrating the position data from GPS with fluorometer data in current study allowed for providing the spatial distribution of tracer concentration while it mixes along the river path.

The fluorometer used in the present study was a WetlabECO-RHRY, integrated within a Seabird SBE19-Plus Conductivity-Temperature-Depth (CTD) probe. This fluorometer can detect Rhodamine WT concentrations ranging from 0.01 ppb to 230 ppb with 0.01 ppb sensitivity (i.e., resolution). Rhodamine WT concentrations were recorded with a sampling frequency of 4 Hz. Fluorometer data was collected at one elevation in the flow, assuming zero vertical concentration gradient. This was a reasonable assumption because the river was very shallow at the outfall (less than 1m), thus full vertical mixing occurred very close to the outfall.

The river hydrodynamics were also measured using a Sontek M9 Riversurveyor acoustic Doppler current profiler (aDcp). This aDcp has a small "blanking distance" of 20cm, i.e., it obtains its first measurement bin only 20 cm from the transducers, which was essential for this study because the river was shallow with depths of only O(1 m) during the survey. The aDcp measured water velocities and depths at 1 Hz sampling frequency. The surveying procedure started 3 hours after the start of Rhodamine injection, which was sufficient time for the tracer concentration spatial distribution to stabilize in the near and medium fields. The fluorometer and aDcp data was collected simultaneously and synchronized by

means of Global Positioning System (GPS) position and time-stamp data that was integrated into the data streams collected by both the flourometer and the aDcp. A survey grade dual frequency real-time kinematic (RTK) Global Differential Positioning System was employed on the boat to locate the measurements. The GPS was manufactured by Novatel, and included a Novatel DL-V3-L1L2 base receiver and a Novatel Propak LB+ rover receiver with reported relative horizontal position accuracy of ±2 cm CEP (i.e. 50% of position estimates have error < 2 cm). The precision of the RTK-DGPS system was previously evaluated by Rennie and Rainville (2006), wherein average error of measured RTK-DGPS velocity equaled 2.6 cm/s. The radio communication between base and receiver had a range of about 10 km, which limited RTK accuracy to this range. For sampling at larger distances from the outlet, differential correction was obtained conventionally using the Wide Area Augmentation Strategy (WAAS), which has position accuracy of O(1m) and average velocity error of about 10 cm/s. Position data was collected at 10 Hz, and were integrated into the fluorometer and aDcp data sets for correct positioning and synchronization of the fluorometer and aDcp data.

The river discharge during the field campaign was approximately 115 $m^3/s$ from Hydat data (Water Survey Canada) for the gauge station 05DF001, located at approximately 113° 28.634'West (longtitude) and 53° 32.385'North (latitude), 26 km upstream of the outfall. The average October North Saskatchewan River flow rate between 2000 and 2009 was 163 $m^3/s$, and the average flow rate for 29th of October was 135 $m^3/s$.

The hydrograph data (Fig. 3.3) for this gauge station shows river discharge variation between 96 $m^3/s$ and 136 $m^3/s$ during our field campaign. The river discharge during the survey was slightly below the long term average for the period of the survey. This discharge variation was not found to influence plume dispersion substantially, but did modify longitudinal advection of the plume (see Chapter four).

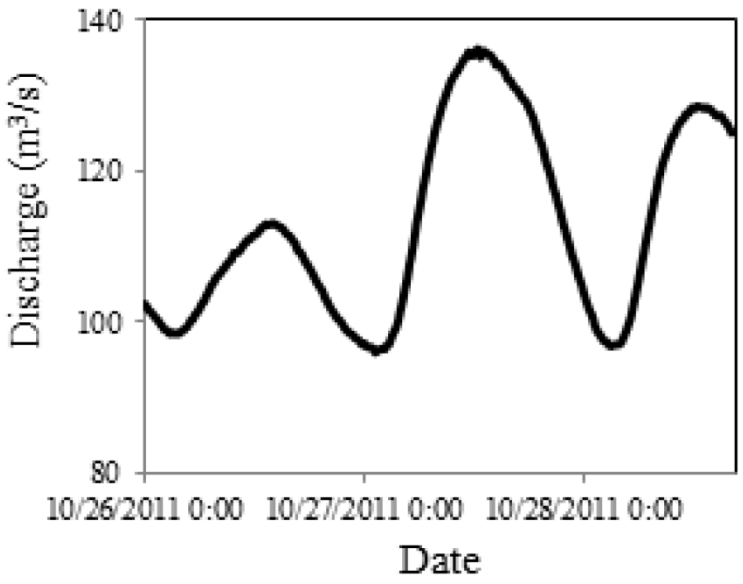


**Figure 3.3 The hydrograph for the gauge station 05DF001 between October 26 to October 28, 2011**

The maximum variation in the discharge was about 35%, which occurred in 12 hours. The duration of survey in each sub-reach was about 1 hour and considering the average variation of 3% per hour for river discharge, the steady state condition was assumed during each sub-reach survey. Furthermore, when calculating shear velocities at a section (see below), it was assumed that flow unsteadiness was too weak to disrupt formation of fully developed semi-log velocity profiles. Song and Graf (1995) evaluated velocity profiles in unsteady flow, and determined that the log-law holds within the inner region in unsteady flows, similar to observations in steady uniform flows. Furthermore, they defined an unsteadiness parameter $\Gamma_{HG} = \frac{1}{u*}\frac{\Delta D}{\Delta T}$ where $u_*$ is the bed shear velocity before the passage of the unsteady wave, $\Delta D$ is the change in depth with passage of the wave, and $\Delta T$ is the time duration of the wave. In their experiments, $\Gamma_{HG}$ ranged from 4E-3 to 18E-3. The largest possible value that could have been observed during our field measurements was more than an order of magnitude lower ($\Gamma_{HG}$ = 0.2E-4). Given that a) the log-law holds in unsteady flows, and b) minimal degree of unsteadiness in the present case, the steady state condition was assumed in calculating the shear velocities.

### 3.4 Post processing

The first post processing step was to remove the highest 5% of the collected tracer data from moving blocks of 50 data points. In the next step a low pass filter was implemented on each tracer data time series. The processed data (concentration, velocity, depth, longitude and latitude) were then imported into ARCGIS(9.3) and superimposed on a North Saskatchewan river boundary shape file, downloaded from http://www.geobase.ca/geobase/en/index.html.

Due to river flow, the boat moving across the river was not on a straight line. Therefore a straight line perpendicular to the river banks was drawn near the most parallel boat transects within a sub-reach. Adjacent upstream and downstream data points were snapped perpendicularly to this drawn line. As discussed below, the snapped data were then used to represent the concentration and/or velocity at this sub-reach. In order to be able to infer the pattern and characteristics of mixing from collected sample data, each cross section was split into 20 cross-sectional intervals, and the average tracer concentration was calculated for each interval.

As previously mentioned, shear velocity is an important parameter for predicting the mixing process. This important parameter is generally estimated as,

$$u_* = \sqrt{ghS} \qquad \textbf{(3.4.1)}$$

where g is gravity, h is the average depth and S is the river slope. However, Boxall and Guymer (2003), found that Eq. (3.1) overestimates the shear velocity at bends. In the present study, shear velocity was estimated from the slope of the fitted log-law vertical profile of stream wise velocity measured with the aDcp (Eq. 3.2).

$$u = \frac{u_*}{\kappa}\ln(z) + \frac{u_*}{\kappa}\ln(\frac{30}{k_s}) \qquad \textbf{(3.4.2)}$$

In Eq. (3.2) u is the velocity in the bin at height z above the mean bed elevation, κ is the von Kármán constant (0.41)`, and ks is the bed roughness. Following Rennie and Church (2010) a moving average of 11 adjacent aDcp pings were employed to calculate the velocity profile for each shear velocity estimate. Shear velocity estimates were filtered if calculated ks exceeded 5 m or was less than 0.1 mm. This method had been successfully used by Rennie and Church (2010) for mapping the shear velocity in Fraser River, British Columbia.

Due to fewer velocity points, shear velocity uncertainty is greater for shallower profiles (Rennie and Church 2010). In order to minimize the effect of this uncertainty, further filtering was implemented on estimated shear velocity within each of the surveyed sub-reaches. In the first step, the 95% confidence interval was estimated for each individual shear velocity estimate based on the lower and upper confidence limits for the log-law regression slope (Eq. 3.3 and 3.4)

$$L = u_* - S\,t_{\alpha/2,n-1} \quad \textbf{(3.4.3)}$$

$$U = u_* + S\,t_{\alpha/2,n-1} \quad \textbf{(3.4.4)}$$

where L and U are respectively the lower and upper limits of the confidence range, and u* is the shear velocity estimated from the slope of the particular log-law velocity profile. The parameter S is the standard error of the u* estimate from the log-law regression, which depends upon the number of points in the velocity profile (n) and the regression residuals. Finally, tα/2,n-1 is the standard random variable from the T-distribution for a probability of α/2, where α equals 0.05 for the 95% confidence interval.

In the next step, all estimates within a sub-reach were grouped into a single population, with the goal being to identify the average value for the sub-reach. Within a sub-reach population, profiles identified as producing outliers for any of the lower confidence limit, upper confidence limit, or the estimated shear velocity were removed. For each of these statistics, outliers were identified as the points where $A>0$ or $B<0$, where

$$A = Obs - (Q3 + 1.5IQR) \quad \textbf{(3.4.5)}$$

$$B = Obs - (Q1 - 1.5IQR) \quad \textbf{(3.4.6)}$$

In Eqs. (3.5) and (3.6), *Obs* is the observation value, *Q1* and *Q3* are the first and third quartiles respectively; and $IQR=Q3-Q1$ is the interquartile range. The observation point was removed from the data set for the points where any of the upper, lower or estimated shear velocity was an outlier. The statistical parameters for filtered and raw data for section S1 are provided in Table (3.2).

**Table 3.2 Statistical characteristics of raw and filtered shear velocity data for S1**

| Section (*S1*) | Number of observation | Mean value(m/s) | Standard deviation | Coefficient of variation | Skewness |
|---|---|---|---|---|---|
| Raw | 1516 | 0.085 | 0.073 | 85.68 | 6.51 |
| Filtered | 791 | 0.080 | 0.026 | 32.49 | 0.22 |

After removing the outliers of each sub-reach data set, the results were imported again into ArcGis 9.3. The imported dataset included depth averaged velocity, bed elevation, estimated shear velocity, bed roughness and position data of the surveyed points within each sub-reach. Within each of the surveyed sub-reaches, these parameters were then interpolated using the kriging method. The mean value of interpolated data was then chosen as representative of that parameter in the surveyed sub-reach.

## 3.5 Results

### 3.5.1 Tracer concentration

The cross-sectional transverse distributions of measured rhodamine tracer concentrations (µg/l, or equivalently, ppb) are plotted for river sections at different distances downstream of the outfall in Fig. 3.4. In all of the provided graphs the *x*-axis is the normalized transverse distance across the section, which was calculated from the right bank side of the river (facing downstream). Due to shallow water depth, there were some sections in which the fluorometer could not be kept in the water for the whole section, thus no in situ tracer data is presented for those parts of the sections.

(a) S1

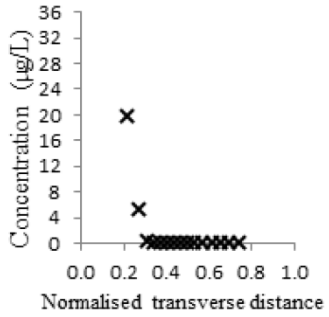


(b) S2

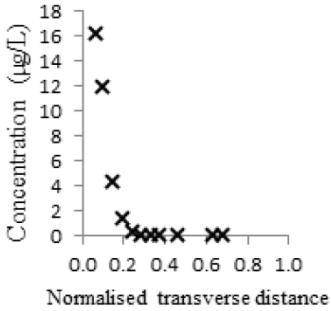


(c) S3

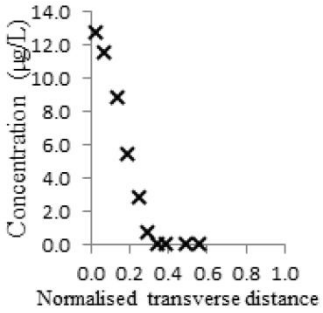


(d) S4

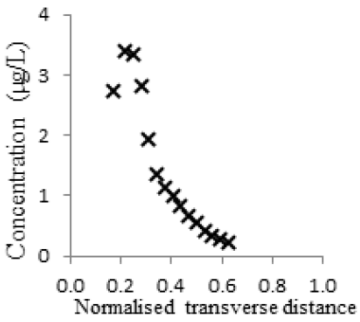


(e) S5

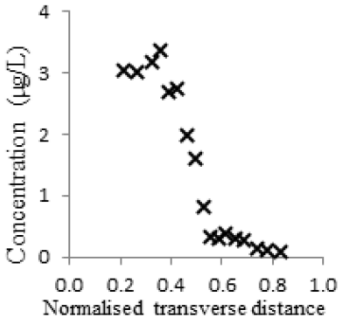


(f) S6

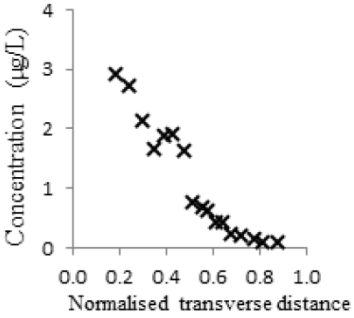


(g) S7

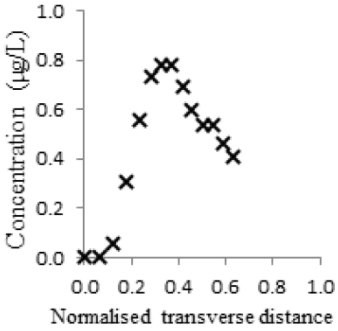


(h) S8

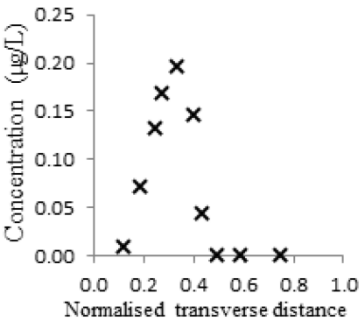


(i) S9

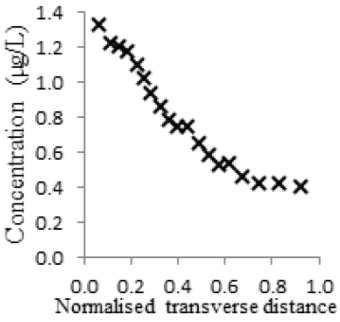

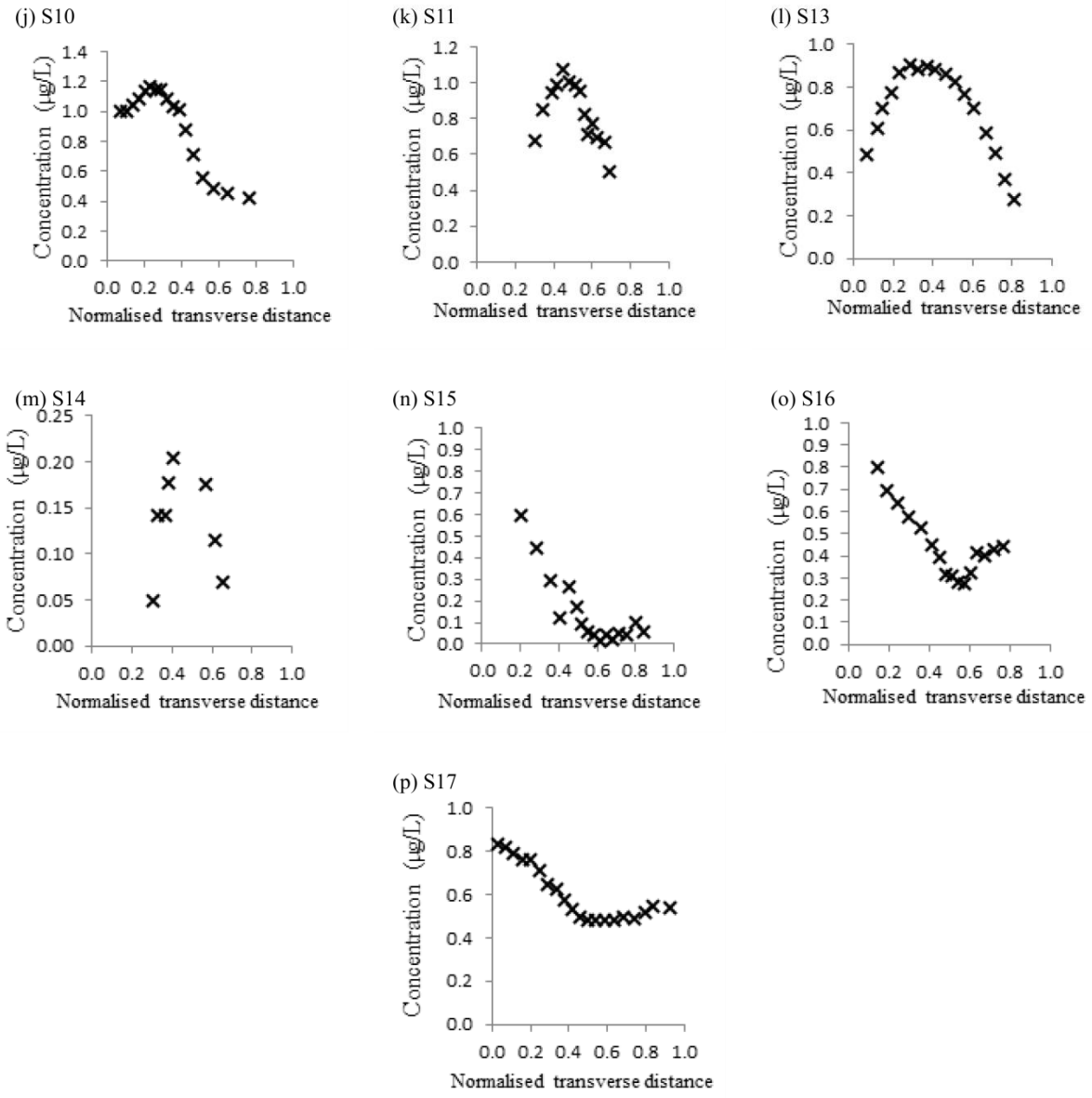


**Figure 3.4 Measured tracer concentration for surveyed sections S1 through S17**

The tracer was injected at the outfall located at the right bank side of the river, thus in most of the sectional tranverse concentration profiles (Fig. 3.4), the highest tracer concentration across the section was observed at the right bank side. Tracer concentration gradually reduced along the river path to 0.83 µg/l at the last surveyed section (82 river km from the outfall). The rhodamine reached the left bank at the sharp bend 6.5km from the outfall. The highest measured rhodamine concentration difference between left bank side and right bank side reduced from 16 µg/l in S2 to 0.27 µg/l in S17.

In order to investigate the effect of the sharp bend located 6.5km downstream of the outfall, sections S4, S5, and S6 were closely spaced in the beginning, middle, and end of the sharp bend. From the rapid change in the transverse distribution of tracer concentration between these sections (Fig. 3.4), it is apparent that the bend flow induced mixing towards the outer bank of the sharp bend. This mixing process is investigated in detail below and in Chapter four.

As the outfall is located at the right bank side of the river, it was generally expected to observe higher tracer concentration in the right bank side of all sections upstream of the full transverse mixing condition. However, at some sections (e.g., S8 and S14) lower peak concentrations were observed near the right bank. This is because the fluorometer samples were not always taken in the longitudinal middle of the plume and the river velocity and depth were not uniform across the river section. The higher depth averaged velocity along the thalweg streamline caused the tracer to move faster within the deeper center portion of the channel section. The influence of non-uniformity in the river velocity and depth is explained below in the discussion section.

### 3.5.2 Velocity and Depth

Flow velocity and depth are the basic parameters that affect the mixing process in rivers. These parameters are used in all of the transverse mixing coefficient prediction methods. In addition, as will be discussed in Chaper four for cross sections located within a sub-reach, local bed features may result in different transverse mixing coefficients. The measured depth averaged velocity and depth are presented in Appendix A (Fig. 3.a.1) for all of the sections where tracer distribution was measured. Similar to Fig. 3.4, the horizontal axis shows the normalized transverse distance. The positive part of the vertical axis presents velocity in m/s and the negative part presents depth in m.

The presented data was calculated by bin-averaging the values measured by the aDcp within 80 intervals across the section. Similar to the concentration graphs, portions of some sections were too shallow to survey with the aDcp (less than 0.5 m). For these portions, data has been generated using linear interpolation between measured neighbouring points.

Due to the topographic steering, it is generally expected to observe higher depth averaged velocity along the thalweg streamline which follows the deeper part the channel (Dietrich and Smith, 1983). In most of the surveyed sections in this study, the thalweg was located in the channel center where increased depth-averaged velocity was observed Fig. 3.a.1.The largest measured depth was 4.9m in the middle part of section S5 which was located around the middle portion of the sharp bend.

Within each of the surveyed regions used to generate data at a section, the collected data was spatially interpolated using the kriging method and the average of the interpolated data fields are presented in Table (3.3). The measured tracer concentration, stream-wise velocity and depth at the sharp bend, was presented at three sections S4, S5 and S6, in Fig. 3.4 and Fig. 3.a.1. However, the average values of measured parameters were calculated for the entire data set collected along the bend and presented as sub-reach S4-S6 in Table (3.3).

**Table 3.3 Summary of reach averaged data from surveyed sub-reaches**

| Sub-reach | Mean velocity (m/s) | Width (m) | Mean depth (m) | Mean Shear velocity (m/s) | Bed roughness (m) | Total observation | Percentage of good observation (%) |
|---|---|---|---|---|---|---|---|
| *S1* | 0.69 | 133 | 1.3 | 0.08 | 0.21 | 1516 | 44 |
| *S2* | 0.69 | 133 | 1.3 | 0.07 | 0.33 | 730 | 52 |
| *S3* | 0.69 | 140 | 1.3 | 0.06 | 0.20 | 1172 | 61 |
| *S4-S6* | 0.46 | 103 | 2.4 | 0.04 | 0.31 | 1859 | 52 |
| *S7* | 0.62 | 146 | 1.2 | 0.07 | 0.39 | 1132 | 85 |
| *S8* | 0.7 | 144 | 1.1 | 0.07 | 0.29 | 607 | 52 |
| *S9* | 0.48 | 123 | 2 | 0.05 | 0.75 | 766 | 52 |
| *S10* | 0.4 | 116 | 2.3 | 0.04 | 0.36 | 417 | 60 |
| *S11* | 0.55 | 147 | 1.3 | 0.06 | 0.31 | 861 | 44 |
| *S12* | 0.39 | 178 | 1.5 | 0.04 | 0.62 | 910 | 37 |
| *S13* | 0.6 | 183 | 1 | 0.08 | 0.84 | 1017 | 50 |
| *S14* | 0.63 | 154 | 1.2 | 0.07 | 0.78 | 520 | 62 |
| *S15* | 0.67 | 146 | 1.4 | 0.09 | 0.80 | 824 | 63 |
| *S16* | 0.77 | 183 | 1 | 0.08 | 0.26 | 966 | 65 |
| *S17* | 0.49 | 152 | 1.8 | 0.05 | 0.18 | 646 | 33 |

### 3.5.3 Shear velocity and roughness

Shear velocity $u_*$ is one of the most important parameters for describing the mixing process. The shear velocity is a measure of the bed shear stress, and is indicative of the near-bed velocity and fluid shear. In meandering rivers, a higher shear velocity is generally observed in the regions with higher bed roughness ($k_s$), turbulence and secondary circulations.

As described in the Post Processing section, in this study the shear velocity and the bed roughness were calculated from the slope and intercept of a fitted log-law velocity profile (Eq.3.2). A filtering process was then implemented and the filtered data was interpolated using the kriging method. The sub-reach averages of interpolated values are presented in Table (3.3). The estimated shear velocity values of surveyed sub-reaches generally show a consistent trend especially in the neighbouring sub-reaches. The maximum and minimum estimated shear velocity was 0.09 m/s and 0.04 m/s respectively.

Estimating the shear velocity from the slope of the fitted log-low has been used successfully in various studies of fully developed two-dimensional flows (e.g., Reynolds *et al.* 1994). However, in meandering channels, the shear velocity is also affected by the secondary circulation generated at bends (e.g., Kashyap *et al.* 2012; Jamieson *et al.* 2013). These secondary circulations prevent development of a logarithmic velocity profile (Blanckaert and De Vriend 2003). Therefore the estimation of shear velocity and bed roughness on the basis of a log-law fit may not be accurate for the sub-reaches located within the bend region. In the current study, sub-reaches S4, S5 and S6 are located along a sharp bend. The estimated roughness for these sub-reaches is larger than other sub-reaches. However, the estimated shear velocity in this region is lower than other surveyed sub-reaches. This can be attributed to the measuring time which was carried out during the low flow season in the river when shear tends to be low in bends (cf. velocity reversal hypothesis, Keller 1971, MacVicar 2010 ) .

### 3.5.4 Sharp bend

Due to the importance of bends in the mixing process within meandering rivers, interpolated spatial distributions of shear velocity, depth and velocity are mapped (Fig. 3.6, 3.7, 3.8) for the sharp bend located 6.5 km downstream of the outfall (see Fig. 3.2, sections S4, S5 and S6). In recognition of streamwise variation along a sharp bend, the collected data was interpolated by kriging three sub-sets corresponding to the upstream, central and downstream portions of the bend.

The spatial map of depth-averaged velocity (Fig. 3.5) shows two regions of high velocity. The first one is located closer to the outer bank of the bend. It is formed within the upstream portion of the sharp bend and extends to the bend exit. The second region, which has larger maximum velocity (1.5 m/s), is located closer to the inner bank just upstream of the bend apex. This second region moves towards the outer bank along the central portion of the bend and combines with the first region by the end of the central portion of the bend (cf. Kashyap *et al*. 2012). The higher velocity region stays close to the outer bank in the downstream portion of the bend.

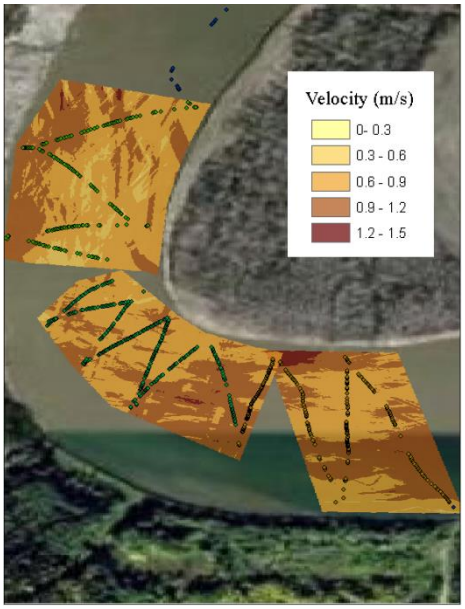


**Figure 3.5Spatial distribution of depth-averaged velocity (ms-1) along the sharp bend. Flow is from bottom right to top. The survey track is shown as a zig-zag pattern. Underlying satellite image obtained from Google Earth.**

Figure 3.6 illustrates the spatial distribution of the flow depth along the bend. The deepest portion of the bend is observed where the thalweg reaches the outer bank just downstream of the bend apex. In the upstream portion of the bend, the thalweg is close to the inner bank of the bend. The thalweg moves toward the outer bank in the middle portion of the bend and again moves back toward the channel center in the downstream portion of the bend. The observed bathymetry pattern is typical of sharp meander bends (e.g., Jamieson *et al*. 2013 a and b).

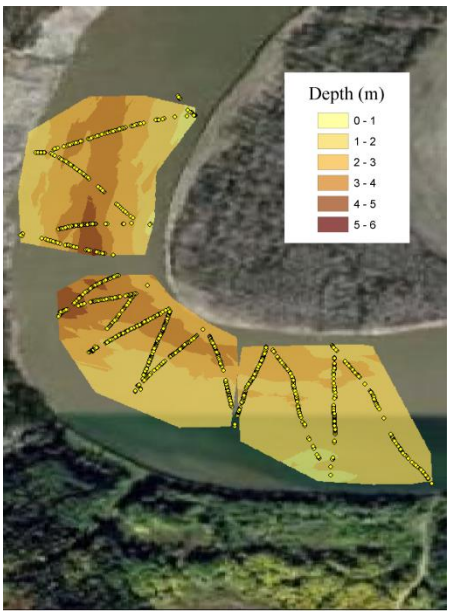


**Figure 3.6 Spatial distribution of depth (m) along the sharp bend. Flow is from bottom right to top. The survey track is shown as a zig-zag pattern. Underlying satellite image obtained from Google Earth.**

The higher shear velocity region is observed close to the outer bank, in the upstream and central portion of the bend (Fig. 3.7). This region of high shear velocity appears to correspond to local flow acceleration immediately upstream of a near-bank sediment deposit on the outer bank upstream of the bend apex. The high shear velocity region at the outer bank diminishes along the bend and moves towards the inner bank in the downstream portion of the bend. This is somewhat contrary to previous laboratory and numerical observations of bed shear stress distribution in channel bends, which suggest that the zone of high bed shear stress within a bend transitions from the inner to the outer bank (e.g., Blanckaert 2011; Kashyap *et*

*al.* 2012). However, it should be recognized that the effect of the secondary flow generated at the sharp bend has not been considered in estimating the shear velocity, as the estimate is based on the assumption of a fully developed logarithmic velocity profile. Furthermore, the measurements were conducted during low flow conditions, which may have altered the observed spatial distribution of bed shear stress.

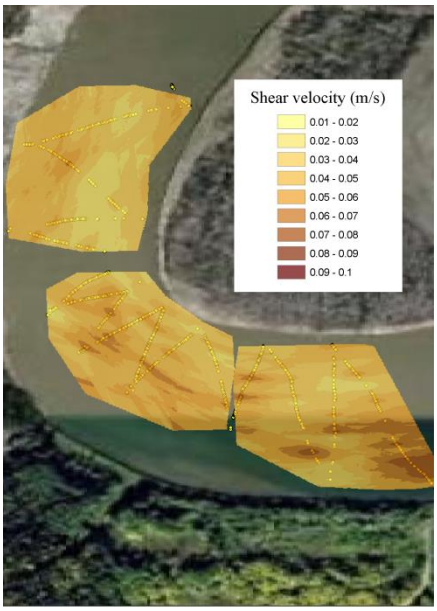


**Figure 3.7Spatial distribution of shear velocity (ms-1) along the sharp bend. The survey track is shown as a zig-zag pattern. Underlying satellite image obtained from Google Earth.**

### 3.5.5 Cross section width

The effect of cross section width on transverse mixing coefficient was first introduced by Lau and Krishnapan (1981). Since then, this parameter has been used in most of the methods developed for estimating transverse mixing coefficient in meandering rivers. In the present study, section surveys were limited to navigable portions of the channel. The presented value for cross section width in Table (3.3) is the value that produces the same discharge as measured by aDcp from the measured flow depth and depth averaged velocity. Therefore, the presented values for river width are less accurate than the measured values for depth and depth-averaged velocity. Nevertheless, the presented values in Table (3.3) can be used to show the variation of cross section width in different sub-reaches along the surveyed reach.

### 3.6 Discussion

The coherence between the presented cross sectional distributions of tracer concentration (Fig. 3.4) suggests that the collected tracer data can be used to investigate the mixing pattern in the North Saskatchewan River. The tracer was injected for 13 hours and the approximate length of the tracer plume was expected to be approximately 25 km. As the rhodamine was injected from the right bank into the river, it was highly concentrated in the right bank side of the river and the measured concentration on the left bank side was zero for the initial sections. The tracer reached the left bank at section S5, located 6.5 km downstream the outfall. At sections S4, S5 and S6, a shift is observed in the centroid of tracer distribution toward the centre of the channel. This lateral translation of the locus of the tracer concentration is essential for the transverse mixing process, and is attributed to two mechanisms: 1) the transverse velocity as a result of transverse and longitudinal variation of depth and velocity at the sharp bend (Blanckaert 2011; Kashyap *et al*. 2012), and 2) differential advection in the channel centre versus near the channel banks.

As flow enters a meander bend the inertia of the fluid causes it to advect towards the outer bank. In very sharp bends this can lead to flow separation at the inner wall, but even in more moderate bends without flow separation, a shear layer can be observed between low speed fluid near the inner wall and the high velocity core advecting to the outer wall (Constantinescu *et al.* 2013). Advection to the outer wall leads to superelevation of the water surface along the outer bank, which sets up a pressure gradient that drives the formation of secondary circulation cells, with flow directed toward the inner wall near the bed and toward the outer wall near the water surface. The secondary circulation dramatically enhances transverse mixing. Importantly, the advection of the high velocity core toward the outer wall encourages transverse dispersion toward the outer wall. This was observed in the present study, as seen in S4-S6 in Fig. 3.6.

The shift along the reach in locus of tracer concentration toward the channel centre can also be attributed to the difference in advection speed between the channel center versus the edges of the channel.

This was important because the tracer was released for 13 hours to form a tracer slug as opposed to a continuous release, thus steady state was not achieved at the leading and trailing edges of the plume. Due to the higher flow velocity in the deeper part of the section (Dietrich and Smith, 1983), the tracer advected faster in the thalweg which was located in the middle of the channel for most of the surveyed sections in this study. This influenced the observed transverse distributions of tracer concentration at individual sections, depending upon when they were surveyed with respect to the advection time of the plume. In sections such as S7, S8, S10, S11, S12 and S14, which were located in front of the tracer plume at the time of their survey, higher tracer concentration was observed in the middle of the section (e.g., Figures 3.4g and 3.4h). This was determined by comparing velocities measured near the bank and in the center of the channel. Between the outfall and S8, the average measured flow velocities near the right bank and the middle of the section were 0.38 and 0.7 m/s, respectively. Considering the period between starting the injection and the measurement time for S7 and S8, it is concluded that the tracer should have reached the middle of these sections but not the right bank. In contrast, in sections S15, S16 and S17, which were located in the rear part of the plume at the time of their survey, lower tracer concentration was observed in the middle part of the section (Fig. 3.5). This influence of differential advection speed across the section has been confirmed by numerical simulation results in Chapter four.

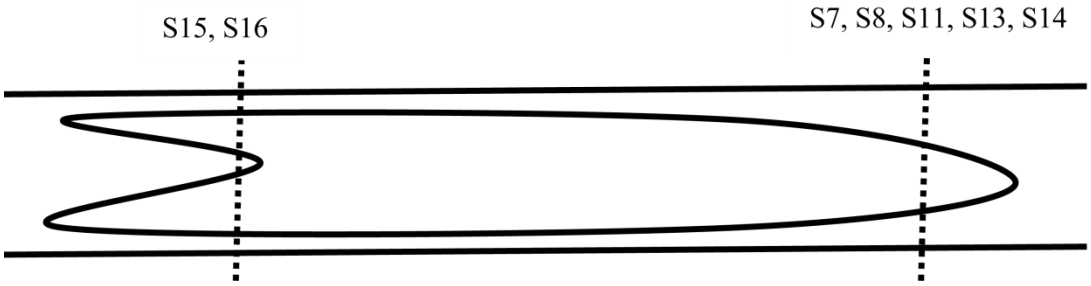


**Figure 3.8 Schematic of the advecting tracer slug, showing locations of the presented sections for the front and rear part of the plume. Flow from left to right. Sections S7, S8, S10, S11, S12, and S14 were surveyed at the leading of the plume, whereas sections S1**

As mentioned in the Introduction section, the main goal of field studies is to provide data sets which can be used to estimate the mixing coefficients. Both analytical and numerical approaches have been used in

the literature for estimating the mixing coefficients in the meandering rivers. The numerical methods allow for considering the effect of discharge variation in the river as well as unsteady tracer injection. The provided tracer data in this study was used in a developed numerical model in Chapter fourin a stream-tube orthogonal curvilinear coordinate system. The transverse mixing coefficient was estimated in different surveyed sub-reaches. The numerical model results were also compared with the estimated transverse mixing coefficient from the standard and general method of moments. Due to the high range of discharge variation, the influence of the varying discharge on transverse mixing coefficient was also studied by comparing the numerical model results in steady and unsteady flow conditions. The unsteady discharge condition changed the estimated averaged transverse mixing coefficient by 10%. The highest transverse mixing coefficient was found in the sharp bend which was attributed to the high sinuosity and the effect of secondary circulation on the mixing process. The higher transverse mixing coefficients were generally found in the sub-reaches with high shear velocity. Using the transverse mixing coefficient in different sub-reaches, the average transverse mixing of 0.037 $m^2/s$ was calculated for the entire surveyed reach of the North Saskatchewan River. Using the estimated shear velocity, depth and depth averaged velocity in this study, the average transverse mixing coefficient of 0.0423 $m^2/s$ was calculated using the Jeon *et al.* (2007) formula, which was in good agreement with the estimated value from the numerical approach.

Comparing the presented averaged values for velocity, depth and width in Table (3.3), a consistent trend is observed between variation of average velocity, depth and river section width in different sub-reaches. The average stream-wise velocity measured at sub-reaches surveyed on October 26 and 28 were 0.66 m/s and 0.68 m/s, which are higher than the average velocity in the sub-reaches surveyed on October 27 (0.5 m/s). The higher velocity for October 26, in spite of lower average discharge on that day, is attributed to lower average cross section area for the sections surveyed on October 26.

The highest average depth in a sub-reach (2.4 m) was measured at the sharp bend located 6.5km downstream of the outfall (S4, S5 and S6). This is attributed to induced secondary flow creating high average shear stress in the sharp bend at channel forming flow, although our measurements at low flow

did not yield highest shear velocity in this sub-reach. The second largest depth (2.3 m) was observed at S10 downstream of an island located in the middle of the channel. The higher averaged depth in this sub-reach is attributed to higher shear stress in the anabranch confluence downstream of the island. In the other surveyed sub-reaches the averaged depth varied between 1 m and 1.8 m.

The high rhodamine concentration difference between left bank side and right bank side reduced from 100 ppb at the outfall to 0.27 ppb at S17. However, this value is still 46% of the average rhodamine concentration at the 83 km section, which means that the full mixing condition was not achieved.

The 64% mixing at section S17 located about 83 km downstream of the outfall suggests a full mixing length of 130 km for the effluent discharged from Capital Region WWTP in the North Saskatchewan River. This is also in agreement with Pilechi et al. (2012) which inferred 123 km as the full mixing length of the discharged effluent from Goldbar WWTP into the North Saskatchewan River based on measurements up to 110 km downstream of the outfall. Therefore, $L_z$=130 km is inferred as the maximum full mixing length for the surface bank outfall in the North Saskatchewan River at low flow. From the average velocity, width and roughness data in table (3.3), the full mixing length of 66 km as well as cross distance of 3.7 km were calculated from the proposed formula by Rutherford (1994). Although the observed full mixing length falls within the suggested range by Rutherford (1994) for a point source near the bank, it is much higher than the calculated value from the proposed formula. This discrepancy is attributed to the simplifying assumption in the proposed formula which is based on a monotonic decrease in concentration gradient in relation to increased distance from the source. The observed cross distance is 6.5 km is also higher than the calculated value from the proposed by Rutherford's (1994) formula (3.7 km). Both Rutherford's cross distance and full mixing length formulae underpredicted by a factor of approximately two.

The two regions of high stream-wise velocity observed in the upstream portion of the sharp bend (Fig. 3.6) are attributed to the outer and inner bank cells of secondary flow (Blanckaert 2011). Secondary flows are generally observed in meandering river bends and act as the driving force of the velocity excess (Blanckaert 2011). The formation of the secondary flow is a function of the river plan form. Secondary

flow causes transverse shear velocity and leads to the transverse bed slope with higher flow depth in the outward direction of the bend (Fig. 3.7). The inner bank and outer bank regions of high stream wise velocity were also observed in Kashyap *et al.* (2012). The ratio of channel width to depth in the current study (61) is much higher than in Kashyap *et al.*'s (2012) test cases (5, 6.5). Regardless, a similarity is observed between the general spatial distribution patterns of stream wise velocity and depth in the current study and Kashyap *et al.* (2012).

The higher shear velocity at the outer bank side of the upstream portion of the bend may be due to the sediment deposition on the outer bank, or the effect of secondary flow on developing the logarithmic profile of velocity. It should be noted, as the measurements were carried out in low flow season (not channel forming flow), it might not be expected to see the same spatial pattern for shear as observed in lab studies.

## 3.7 Summary and Conclusions

A field campaign was carried to study the mixing pattern over a 83 km reach of the North Saskatchewan river. Rhodamine WT was injected as a tracer of the wastewater effluent from the outfall of Capital Region WWTP. The tracer concentration was tracked with a new measurement technique by moving a boat across and along the river with an in situ fluorometer. The real-time in situ measurements allowed for much higher sampling intensity than conventional water sampling, and also facilitated locating the plume while in the field. The tracer data was integrated with GPS data and provided a spatial distribution of tracer across the river. The maximum measured rhodamine concentration was reduced from 100 ppb close at the outfall to 0.83 ppb at 83 km downstream of the outfall. At the last surveyed section, a rhodamine concentration difference of 46% was observed across the section, thus the full mixing condition was not achieved by 83km from the outfall. A full mixing length of 130 km was inferred for a surface bank outfall in the North Saskatchewan River at the observed low flow stage. The employed technique was found effective for investigating the mixing behaviour as well as full mixing length of meandering rivers by providing reliable and extensive data sets.

During the survey, the depth-averaged velocity and water depth were also measured with an aDcp. The average depth and depth-averaged velocity along the river were 1.36 m and 0.6 m/s respectively. Greater depth-averaged velocities were observed in the deeper parts of each section. This was attributed to topographic steering which causes higher depth-averaged velocity along the thalweg stream line (Dietrich and Smith, 1983). The shear velocity and roughness were also estimated from the slope and intercept of best fitted log-law on the collected depth averaged velocity profiles.

The observed cross distance of 6.5 km from the outfall corresponded to the location of a sharp bend, thus confirming the importance of river meandering for the transverse mixing process. Due to the complex structure of flow in sharp bends as well as their importance in the mixing process, the spatial distributions of depth-averaged velocity, depth, and shear velocity were presented at this sharp bend. The maps of stream wise velocity and depth showed good agreement previous studies on sharp bends. The spatial distribution of shear velocity in the bend did not show good agreement with similar previous studies.

### 3.8 Acknowledgements

The authors would like to thank Chris Krath, Mat Langford and Beth Robertson for their field assistance, and Curtis Brock for helpful support in coordinating the field work.

### 3.9 Funding

The field work described herein was funded by Alberta Environment.

## 3.10 Appendix A

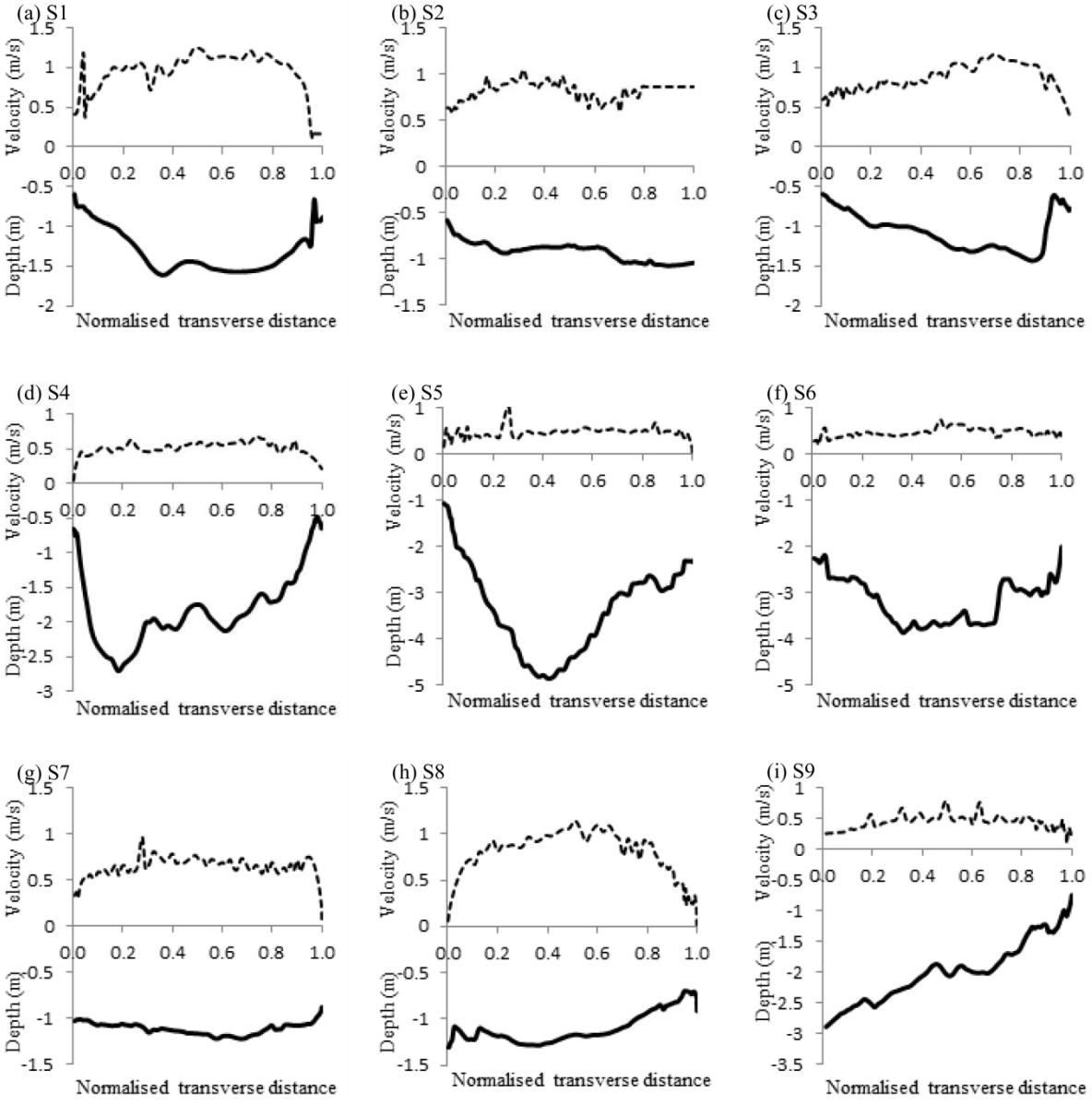

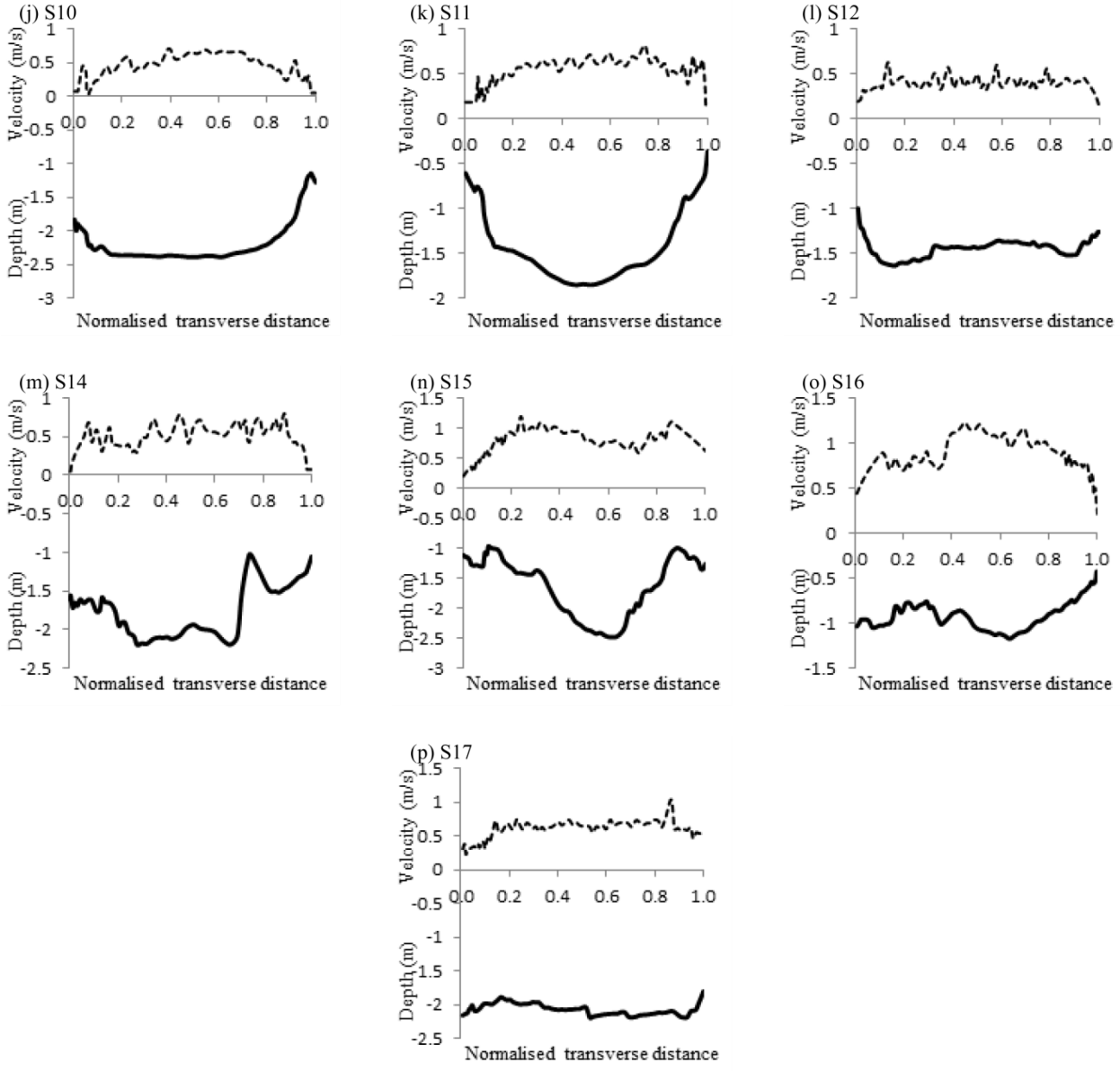


**Figure 3.9 Measured depth averaged velocity (dashed line) and depth (solid line) for surveyed sections S1 through S17**

### 3.11 Notation

$\beta$= empirical coefficient (-)

$\kappa$ = 0.41, von Kármán constant (-)

$v$ = river average velocity ($ms^{-1}$)

$b$ = river width (m)

$E_z$ = transverse mixing coefficient ($m^2s^{-1}$)

$H$ = mean channel depth (m)

$IQR = Q3 - Q1$, interquartile range ($ms^{-1}$)

$k_s$ = roughness (m)

L = lower and upper limits of the confidence range (ms-1)

Lz = full mixing length (m)

Lc = distance downstream of the source where the tracer reaches the opposite bank (m)

n = number of points in the velocity profile and the regression residuals.

Obs = observation value (ms-1)

Pm = ratio of minimum to maximum concentration (-)

Q1 = first quartiles (ms-1)

Q3 = third quartiles (ms-1)

s = standard error (ms-1)

u= velocity in the bin at height $z$ (m)

U= upper limits of the confidence range (ms-1)

u* = shear velocity (ms-1)

U* = average shear velocity (ms-1)

tα/2,n-1 = standard random variable

# Chapter 4: **Numerical Modelling**

## 4.1 An innovative gridding system for numerical modelling in meandering rivers

**Published in the Canadian Society for Civil Engineering 2013 Annual Conference, Proceedings, Montreal, May 29-June 1, 2013**

**Authors:** Abolghasem Pilechi, Majid Mohammadian, Colin D. Rennie

### 4.1.1 Abstract

This paper presents a practical method to generate the computational mesh required for numerical modelling of meandering rivers. The proposed algorithm is based on the "stream tubes" concept. This gridding system transforms the curvilinear coordinates of a meandering river to Cartesian coordinates by discretizing in equal increments of specific flow rate. In order to mitigate the effect of the transverse velocity field, which is usually difficult to measure in field surveys and imposes extra computational cost on a numerical model, the grid has also been orthogonalised in two steps. The grid has been successfully employed in a numerical model for contaminant-mixing in a meandering river, and its performance has been investigated by comparing the model results and measured data.

### 4.1.2 Introduction

The mixing process of discharged pollutants into rivers and waterways has been studied by environmental water resource engineers for many years. Mixing simulation models generally fall into analytical and numerical categories. The analytical models are based on exact solution of a governing equation. In contrast to numerical models, analytical models are free of high computational cost. They are much simpler and more computationally efficient. However, due to simplifying assumptions, these

models cannot consider the variability in channel hydraulic parameters such as depth and velocity, which greatly affect the mixing process, especially in natural meandering channels. So, employing a numerical model is generally preferable for the simulation of mixing in extended and complex natural channels.

Both analytical and numerical approaches require a computational grid in order to solve the governing equations and present the results. In situations where sufficient hydraulic and bathymetry data is available, the numerical approach is applicable. There are different kinds of gridding systems, and each of these gridding systems has specific characteristics that makes it suitable for a particular problem. The governing equations may also vary for different gridding systems. Duan (2004) used Cartesian coordinates to simulate mass transport and dispersion in a meandering channel. Due to the capability of the curvilinear coordinate system in modelling meandering channels with highly variable geometry and width, this coordinate system has been widely adopted for hydrodynamic modelling in meandering channels Demuren and Rodi (2006); Molls and Chaudhry (1995); Darby (2002). Smith and Mclean (1984) employed orthogonal curvilinear coordinates to simulate flow in meandering streams. The main advantage of the curvilinear coordinate system over the Cartesian coordinate system is its ability create a smooth mesh, especially n meandering rivers with highly variable alignment and geometry. The mixing equation is also simpler in a curvilinear coordinate system for natural meandering channels (Yotsukura and Sayre, 1976).

Using a numerical approach introduces numerical diffusion errors into the solution (Holly, 1975). There are generally two strategies for minimizing these errors. One method is using higher-order methods, and the other is optimizing grid sizes. Beltaos and Arora (1988), suggested using an irregularly spaced grid in a stream tube coordinate system to minimize the artificial diffusion which is introduced by the advection term in governing equations. This method was later used by Luk et al. (1990) in order to model mixing of a conservative substance in meandering rivers. (Putz and Smith, 1998) also evaluated the (Beltaos and Arora, 1988) method. They compared the model output with unsteady field test results from the North Saskatchewan River.

Unstructured grids are another group of grids which can be employed in numerical models. An unstructured grid system can generate a smoother grid, especially in regions where the geometry of the computational domain is highly variable. However, due to its higher computation cost, unstructured grids are not regularly employed for highly extended regions. Dow et al. (2009) employed an unstructured grid in a hydrodynamic sub-model to simulate mass transport and dispersion in the intermediate mixing zone in the North Saskatchewan River.

The transverse velocity field is generally a difficult quantity to measure in field work. This is an important effective parameter, and it cannot be neglected in the mixing process. The presence of this term in the mixing governing equation makes the equation more complicated and imposes more computational effort. To overcome this, there are generally two methods to eliminate the effect of the transverse velocity field without sacrificing accuracy. One is employing a stream tube coordinate system, and the second is to align the longitudinal direction such that it follows the direction of the depth-averaged velocity (Yotsukura and Sayre 1976). In meandering channels, transverse and longitudinal variations in depth and velocity cause transverse convective transport (Chang 1971), as flow is "topographically steered" toward the deeper parts of a channel section (Dietrich and Smith 1983). This will result in shifting and asymmetry in the cross-sectional distribution of tracer, which generally has Gaussian distribution in a normal diffusion process. This is the main idea of introducing the stream tube concept (Cobb 1972). This concept was later used by Yotsukura and Sayre (1976) in a mathematical model to predict the mixing pattern in a meandering channel. The main concept of this method relies on considering the cumulative discharge $(q)$ instead of lateral distance. The governing equation is also transformed from the $x-y$ coordinate system, where $x$ is the longitudinal and $y$ is the cross-sectional direction respectively to the *x-q* coordinate system. In contrast to the *x-y* coordinate system in which the cross section is divided into strips of equal width, in the *x-q* coordinate system, the cross-section is divided into strips of equal discharge called stream tubes. The stream tube concept has also been used by (Lau and Krishnappan 1981), (Somlyódy 1982),and (Gowda 1984) to represent meandering channels. In natural meandering

channels, one of the main concerns is irregular cross-section and geometry of the channel. The ability of stream tube models in simulating the mentioned irregularities has made them popular for mixing models.

Bathymetry and flow information are the basic information needed in the stream tube gridding system. In the current study, the field-measured depth-averaged velocity and depth data in Chapter three were used to estimate the width of cross-sectional strips.

The presented gridding system in this study uses a combination of the stream tube concept and an orthogonal grid to consider the effect of transverse current without having the difficulties of transforming the governing equations into a cumulative discharge coordinate system. Using this method, an orthogonal stream tube grid was generated for an 83 km reach of the North Saskatchewan River. The generated mesh is employed in a numerical model in Section 4.2 in order to simulate unsteady mixing of a neutral conservative substance in the North Saskatchewan River. The satisfactory results of the numerical simulation show that the gridding system can be employed with an acceptable degree of confidence to model mixing in highly-extended meandering rivers.

This paper is presented as follows. First, the methodology for using the available information and constructing the grid is explained in detail. Subsequently, a few of the results obtained by employing the mesh in a numerical model are presented to evaluate the performance of the gridding system. The paper concludes with a summary of the described method, the presented results, and limitations of the method.

### 4.1.3 Methodology

In the first step, a Cartesian grid was produced by dividing the boundary of the entire surveyed reach into equal longitudinal and cross-sectional intervals. The shape file of the North Saskatchewan River boundary was downloaded from: http://www.geobase.ca/geobase/en/index.html. Following Putz and Smith (1998) and Odigboh (1999), the river section was divided into 20 equal intervals. In order to

eliminate the effect of local bed features on the entire depth field, the grid dimension was not further refined across the river section.

#### 4.1.3.1 Orthogonal grid

As previously mentioned, one of the applicable methods for eliminating transverse velocity is to align the longitudinal direction such that it follows the direction of the depth-averaged velocity (Yotsukura and Sayre 1976). This was achieved by specifying channel sections orthogonal to the banks throughout the domain (Figure 4.1.1). First, the UTM easting and northing coordinates of the channel boundary were used to identify local slopes of each channel boundary line.

$$m_{AC} = \frac{y_C - y_A}{x_C - x_A} \quad \textbf{(4.1.1.1)}$$

$$m_{DF} = \frac{y_F - y_D}{x_F - x_D} \quad \textbf{(4.1.2)}$$

$$m_{BE} = \frac{y_E - y_B}{x_E - x_B} \quad \textbf{(4.1.3)}$$

where *m* indicates slope and the coordinate positions are demonstrated in Figure 4.1.1. This gave the channel boundary slope on each side of the river in the vicinity of a given section ($m_{AC}$ and $m_{DF}$). The negative reciprocal of the average of the local slopes from opposite banks was defined as the slope of the orthogonal section line ($m_{\beta}$).

$$m_{\alpha} = 0.5(m_{AC} + m_{DF}) \quad \textbf{(4.1.4)}$$

$$m_{\beta} = -\frac{1}{m_{\alpha}} \quad \textbf{(4.1.5)}$$

The center point of the section line was defined as the origin, and the UTM right and left bank boundary coordinates were transformed to this origin. Finally, the Cartesian cross-section line and associated boundary coordinates were rotated by angle $\theta$ around its center point to provide an orthogonal coordinate system line and boundary coordinates that are perpendicular to the river path, where

$$\theta = \frac{m_\beta - m_{BE}}{1 + m_{BE} m_\beta} \qquad \textbf{(4.1.6)}$$

The coordinates of $B'$ and $E'$, endpoints of the new cross section line $(B'E')$ in orthogonal coordinates, were then calculated as:

$$x_{B'} = x_B Cos\theta - y_B Sin\theta \qquad \textbf{(4.1.2.7)}$$

$$y_{B'} = x_B Sin\theta + y_B Cos\theta \qquad \textbf{(4.1.8)}$$

$$x_{E'} = x_E Cos\theta - y_E Sin\theta \qquad \textbf{(4.1.9)}$$

$$y_{E'} = x_E Sin\theta + y_E Cos\theta \qquad \textbf{(4.1.3.10)}$$

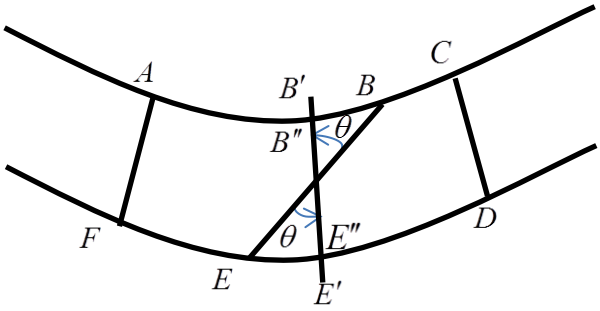


**Figure 4.1.1 Rotating cross-section line to orthogonal coordinates**

In order to keep the river boundary unchanged, the length of the cross-section line had to be modified to $(B''E'')$ as outlined in Equations 4.1.11-17. Having the slope and coordinates of $B'$ and $E'$, the equation for $B'E'$ is obtained:

$$y = m_{B'E''}(x - x_{E'}) + y_{E'} \qquad \textbf{(4.1.11)}$$

As boundary lines $BB''$ and $EE''$ are perpendicular to $B'E'$, their slopes are calculated as,

$$m_{BB''} = -\frac{1}{m_{B'E'}} \quad \textbf{(4.1.12)}$$

$$m_{EE''} = -\frac{1}{m_{B'E'}} \quad \textbf{(4.1.13)}$$

Having the coordinates of $B$ and $E$ as well as the $m_{BB''}$ and $m_{EE''}$ values, the equations of $BB''$ and $EE''$ are obtained:

$$y_{BB''} = m_{BB''}(x - x_B) + y_B \quad \textbf{(4.1.14)}$$

$$y_{EE''} = m_{EE''}(x - x_E) + y_E \quad \textbf{(4.1.15)}$$

The coordinates of $B''$ and $E''$, which are needed in the modified grid, are calculated by solving the system of equations for $BB''$ and $B'E'$; and $EE''$ and $B'E'$ separately.

$$\begin{cases} y_{BB''} = m_{BB''}(x - x_B) + y_B \\ y_{B'E'} = m_{B'E''}(x - x_{E'}) + y_{E'} \end{cases} \quad \textbf{(4.1.16)}$$

$$\begin{cases} y_{EE''} = m_{EE''}(x - x_E) + y_E \\ y_{B'E'} = m_{B'E''}(x - x_{E'}) + y_{E'} \end{cases} \quad \textbf{(4.1.17)}$$

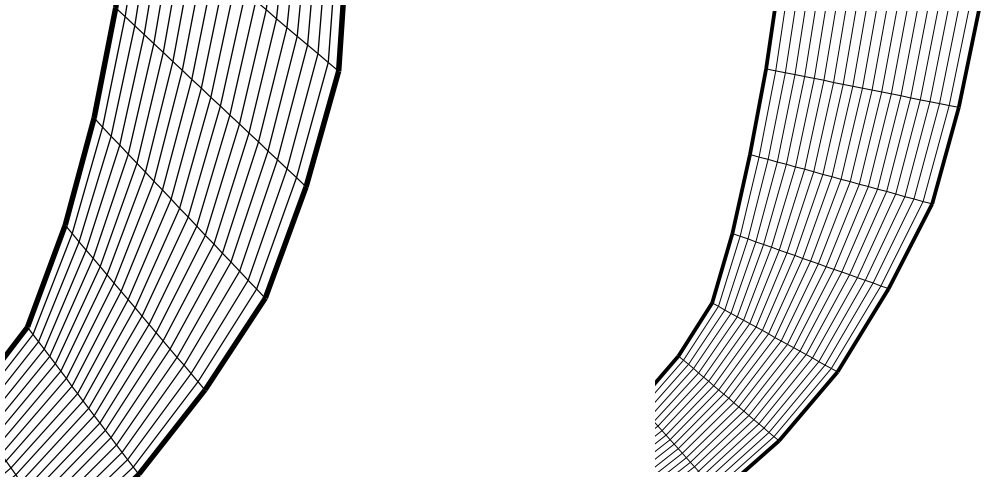

**Figure 4.1.2 Cross-section line before rotation (left), and the cross-section line after rotation (right)**

### 4.1.4 Stream tube grid

The stream tube concept was also employed to eliminate the effect of transverse velocity. To employ this method, the number of cross-sectional intervals (n) should be large enough to capture the mixing process with acceptable resolution. It should be noted that this parameter should be chosen such that the effect of local bed features on the bathymetry is eliminated. Following Putz and Smith (1998) and Odigboh (1999), $m = 20$ was chosen as the number of cross-sectional strips to resolve the tracer concentration with acceptable accuracy. Consequently, in the stream tube coordinate system, the total discharge $(Q)$ was divided into $20$ increments. Each streamtube is formed by $z\Delta x\Delta y$, where $x$ represents the longitudinal, $y$ the transverse, and $z$ the vertical direction. The cumulative discharge $(q)$ is an independent variable which is defined as:

$$q_j = \frac{Q}{m} \qquad \textbf{(4.1.18)}$$

The $q$ variable is defined across the section, and its value varies from $q = 0$ at the right bank side to $q = Q$ at the left bank side. Cross-sectional profiles for depth-averaged velocity and depth, available from an intensive field survey of the North Saskatchewan River (Pilechi et al. 2012), were used for calculating stream tube width at the surveyed sections. The width of the $j^{th}$ strip $(w_j)$ was calculated so that the discharge within each streamtube would be equal to $q_j$ (Fig. 4.1.3):

$$q_j = \sum_{y_{j-1}}^{y_j} u\ h dy \qquad \textbf{(4.1.19)}$$

$$w_j = \int_{y_{j-1}}^{y_j} dy \qquad \textbf{(4.1.20)}$$

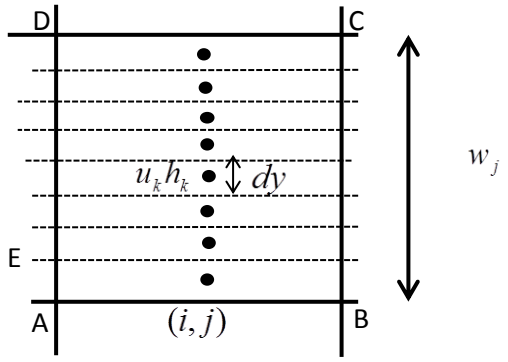


**Figure 4.1.3 Calculating the stream tube's width using the measured velocity and depth**

The parameters $u$ and $h$ are depth-averaged velocity and depth respectively, and $y_{j-1}$ and $y_j$ are transverse distance coordinates of the $j^{th}$ stream tube from the bank. For sections between the surveyed sections, the strip widths were estimated by linear interpolation of strip widths calculated for the surveyed sections.

With the width of each stream tube (perpendicular to the flow direction) as well as the coordinates of the cross-section line edges, the coordinates of cross-sectional grid points within each cross-section can be calculated. For example, starting from the right boundary at cross section $BH$ in Fig. (4.1.4),

$$x_E = \hat{u}_{BH}.w_j + x_B \qquad \textbf{(4.1.21)}$$

$$y_E = \hat{u}_{BH}.w_j + y_B \qquad \textbf{(4.1.22)}$$

where $\hat{u}_{BH}$ is the unit vector of $BH$. The orthogonalisation is then started from the right boundary. Having the coordinate of $B$ and $E$ as well as the slope of $EF$ and $BE'$, the equations for $EE'$ and $BE'$ were obtained.

$$m_{\alpha} = 0.5(m_{AB} + m_{EF}) \quad \textbf{(4.1.23)}$$

$$m_{BE'} = -\frac{1}{m_{\alpha}} \quad \textbf{(4.1.24)}$$

$$y_{EF} = m_{EF}(x - x_E) + y_E \quad \textbf{(4.1.25)}$$

$$y_{BE'} = m_{BE'}(x - x_B) + y_B \quad \textbf{(4.1.26)}$$

The coordinates for $E'$, which is the intersection of $EE'$ and $BE'$, are obtained by solving the above system of equations.

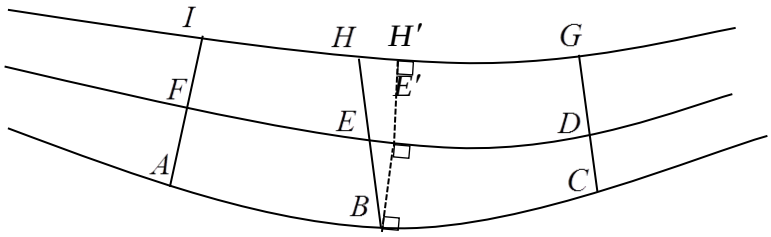


**Figure 4.1.4 Orthogonalising the stream tube coordinate system**

Having the coordinates for $E'$, the edge coordinates in the neighboring strips ($H'$ for example) are calculated sequentially up to the opposite bank side in the same manner as $E'$.

A portion of the final constructed mesh, at the sharp bend about 6.5km downstream the outfall location, is presented in Fig. (4.1.5).

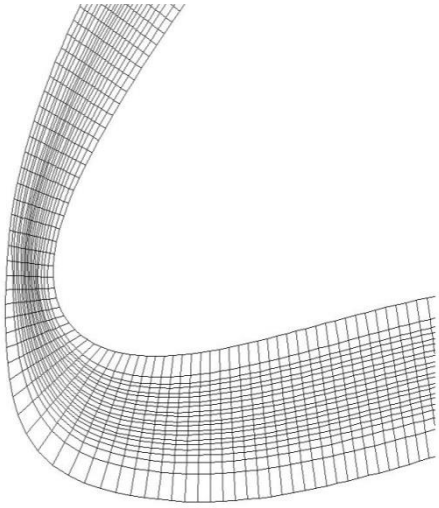

**Figure 4.1.5 A part of the orthogonal stream tube grid at the sharp bend**

### 4.1.5 Results and discussion

The grid generated as described in the previous section is employed in a numerical model in Section 4.2 in order to model the mixing pattern of a natural conservative substance in the North Saskatchewan River.

The model solves a depth-averaged two-dimensional advection diffusion equation (4.1.27) in an orthogonal streamtube coordinate system.

$$\frac{\partial s}{\partial t}+\frac{v_\alpha}{m_\alpha}\left(\frac{\partial s}{\partial \alpha}\right)=\frac{1}{h m_\alpha m_\beta}\left[\frac{\partial}{\partial \beta}\left(\frac{m_\alpha}{m_\beta}hk_\beta\frac{\partial s}{\partial \beta}\right)\right]+R \qquad \textbf{(4.1.27)}$$

In Eq. (4.1.27), the parameter $s$ is the depth-averaged concentration, $v_\alpha$ is the longitudinal velocity, $k_\beta$ is the transverse mixing coefficient, and $R$ is the sink term. The parameters $m_\alpha$ and $m_\beta$ are metric coefficients in the longitudinal ($\alpha$) and transverse ($\beta$) directions. Having the coordinates for all of the grid points, the metric coefficients can be calculated for each of the cells within the computational domain. Further details of the numerical method and definition of parameters can be found in Section 4.2.

In order to evaluate the performance of the generated mesh, the numerical model output and the measured results from the field test are presented in Fig. (4.1.6) for two of the surveyed sub-reaches in Chapter 3.

a) b)

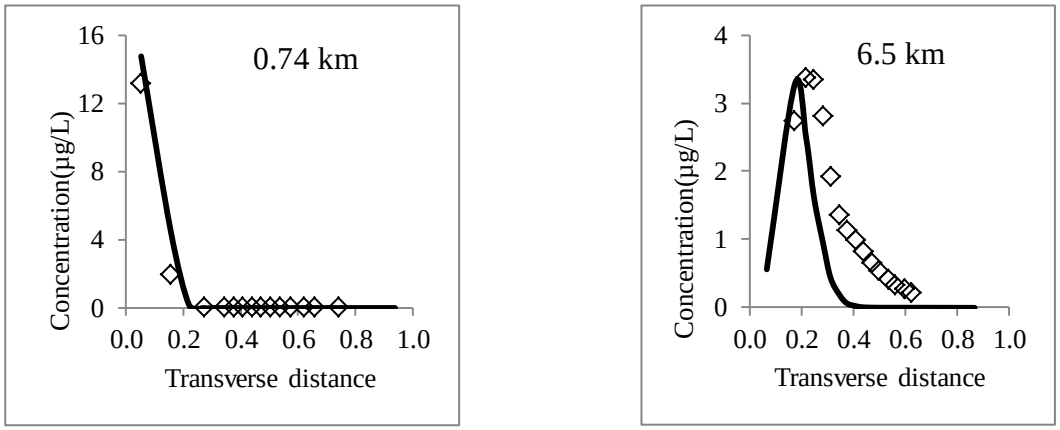


**Figure 4.1.6 Comparison of numerical model output and measured tracer results presented Chapter three. The transverse distance across the section is non-dimensional (divided by section width), and the sub-reach distance downstream of the outfall is specifi**

Fig. (4.1.6) shows the predicted and measured tracer concentration at two different sections downstream from the outfall. The tracer was injected in the outfall located at the river bank (transverse distance 0.0), thus the highest tracer concentration was observed adjacent to the river bank in the section closest to the outfall (Fig. 4.1.6a). Due to the large transverse velocity field at the sharp bend 6.5km downstream from the outfall (Fig. 4.1.6b), the centroid location of the measured profiles moved towards the middle of the section, which was captured in the streamtube coordinate system. In spite of some discrepancy between the centroid of the measured and modeled profiles, the employed gridding system was generally shown to be successful in taking into account the effect of transverse velocity (see Section 4.2).

### 4.1.6 Conclusion

In order to provide a computational domain to study mixing in meandering rivers, an orthogonal curvilinear streamtube gridding system was presented for 83km of the North Saskatchewan River. Starting with the river bank line coordinates, in the first step a curvilinear gridding system was generated for the entire region. In the next step, each cross-section line was rotated to align the longitudinal direction orthogonal to the river banks. Using the depth-averaged velocity and depth from Chapter 3, in the next step the streamtube width of each cross-sectional strip was calculated. In the last step, the entire grid was orthogonalised again to minimize the effect of transverse velocity. The obtained grid is employed in a numerical model to study mixing in the North Saskatchewan Riverin Section 4.2 . Comparing the numerical model output and the field measurements showed that the presented grid is capable of modelling the effect of transverse velocity in a meandering river. This confirms that the presented gridding system can be confidently used to model mixing in extended meandering rivers.

## 4.2 An efficient method for coupling field data and numerical modelling for the estimation of transverse mixing coefficients in meandering rivers

**Accepted to be published in the Journal of Hydraulic Engineering, ASCE**

**Authors**: Abolghasem Pilechi, Majid Mohammadian, Colin D. Rennie, David Z. Zhu

### 4.2.1 Abstract

A numerical model has been developed employing an orthogonal stream-tube gridding system for the investigation of mixing patterns in meandering rivers. The proposed model is a coupled field-modelling approach, in which a measured velocity field is used to solve the advection-diffusion equation, which provides a practical simulation with greater accuracy and lower computational cost for estimation of mixing in meandering channels with a long full mixing length The model has been used to estimate the transverse mixing coefficient in surveyed sub-reaches of the North Saskatchewan River (Canada). Good agreement was observed between the numerical and measured tracer concentrations using reasonable values for the transverse mixing coefficient. The average dimensionless transverse mixing coefficient from the calibrated numerical model for the surveyed reach was 0.39, which was consistent with values estimated using empirical formulas for transverse mixing coefficients in natural meandering rivers. The estimated transverse mixing coefficient was more than an order of magnitude higher in a sub-reach with a sharp bend than in other sub-reaches. For comparison, the transverse mixing coefficient has also been calculated analytically from standard and general methods of moments between some sections.

### 4.2.2 Introduction

Modelling point-source pollution in water resources has been an important issue for water quality and environmental management. Most contaminant point sources are outfalls of waste water treatment, power, or other industrial plants. In natural rivers, due to the relatively shallow water depth, vertical mixing usually occurs rapidly close to the outfall location. Therefore, the transport of neutral pollutants beyond the initial zone can be expressed by the two-dimensional advection-diffusion equation (Rutherford 1994):

$$\frac{\partial}{\partial t}(hC)+\frac{\partial}{\partial x}(hu_xC)+\frac{\partial}{\partial y}(hu_yC)=\frac{\partial}{\partial x}(hD_x\frac{\partial C}{\partial x})+\frac{\partial}{\partial y}(hD_y\frac{\partial C}{\partial y}) \qquad \textbf{(4.2.1)}$$

where $h$ is depth, $C$ is the depth-averaged concentration, and $D_x$ and $D_y$ are the mixing coefficients in the $x$ and $y$ directions respectively, which also include the effects of vertical integration of the initial three-dimensional advection-diffusion equation.

Estimation of the mixing coefficients is an important issue in river-modelling studies, and the objective of this paper is to propose a coupled field-modelling approach to estimate these coefficients. This study is focused on estimating transverse mixing in the intermediate field, which is defined as the region between the full vertical mixing point and full transverse mixing region in rivers (Baek and Seo 2010). In contrast to transverse mixing, which is critical in verifying whether the loading level of introduced pollution exceeds environmental criteria, longitudinal mixing is relatively unimportant in rivers in the intermediate field, especially in the case of slowly varying sources (Rutherford 1994). In most cases, the transverse mixing coefficient ($D_i$) is non-dimensionalized using average shear velocity ($U^*$) as the velocity scale and average depth ($H$) as the length scale (Rutherford 1994).

The methods of determining the transverse mixing coefficient generally fall into two categories: observational methods and predicting methods (Jeon et al. 2007). The observational methods, such as the standard method of moments (Yotsukura and Sayre 1976), general method of moments (Beltaos 1980, Rutherford 1994), cumulative discharge method (Yotsukura and Cobb 1972, Yotsukura and Sayre 1976),

and stream tube routing (Seo et al. 2010) analyze tracer measurements from field work or laboratory experiments to estimate the transverse mixing coefficient. A group of methods are generally based on an analytical solution for simplified forms of (4.2.1) for a steady state condition. Some methods assume small local changes in depth and velocity values while others impose different restrictive assumptions. However, in tracer studies, continuous and steady injection of tracer for a duration equivalent to plume advection time to a fully mixed condition is not possible due to the high amount of tracer needed. This is a limitation of tracer studies, especially in meandering channels with a long full mixing length.

Predicting methods use empirical observations of transverse mixing to propose practical formulas that use hydraulic and geometric parameters to estimate the average transverse dispersion coefficient. These empirical equations use the overall flow parameters for estimating the average transverse mixing coefficient. Table (4.2.1) provides some of the relationships proposed in the literature for estimating the transverse mixing coefficient.

**Table 4.1: Prediction formulas for estimating the transverse mixing coefficient for meandering channels**

| Study | Formula |
|---|---|
| Bansal (1971)* | $\frac{D_y}{HU_*} = 0.002\left(\frac{W}{H}\right)^{1.498}$ |
| Sayre (1979)** | $\frac{D_y}{HU_*} = (0.3 \sim 0.9)(\frac{U}{U_*})^2(\frac{W}{r_c})^2$ |
| Deng et al. (2001)*** | $\frac{D_y}{HU_*} = 0.145 + \frac{1}{3520}(\frac{U}{U_*})(\frac{W}{H})^{1.38}$ |
| Jeon et al. (2007) **** | $\frac{D_y}{HU_*} = (0.0291)(\frac{U}{U_*})^{0.463}(\frac{W}{H})^{0.299}(S_n)^{0.733}$ |

* $W$ is the cross section width
** $r_c$ is the radius of curvature
*** $U$ is the average velocity
**** $S_n$ is sinuosity, which is the ratio of actual path length to the shortest path length

Numerical modelling is another approach which can be used to eliminate the deficiencies of the previously mentioned methods due to their simplifying assumptions. Numerical approaches have been previously used to model mass dispersion in different studies (Ye and McCorquodale 1997, Duan 2004, Gualtieri 2010). In one of the most recent studies, Seo and Park (2010) used the two-dimensional FEM models SMS (Surface-water Modelling System) and RAMS (River Analysis and Modelling System) to study the effect of secondary currents on flow pattern and dispersion in a meandering channel.

Velocity and depth are the required parameters for applying (1) for a mixing model. The velocity field can be estimated using hydrodynamic sub-models. Duan (2004), Darby (2002), and Hsieh and Yang (2003) are examples of two-dimensional models for simulating flow in meandering rivers. Dow et al. (2009) used River2D, a two-dimensional finite element hydrodynamic model, to predict the travel time of a river in a study of intermediate-field transverse mixing in the North Saskatchewan River. Calculating the velocity field from the hydrodynamic sub-models implicitly requires the employment of a suitable turbulence model, and all these calculations eventually impose a greater computational cost for the numerical model and introduce some numerical errors.

Recent advancements in field measurement devices have enabled the measurement of velocity and depth fields with high resolution using an acoustic Doppler current profiler (aDcp) (e.g., Rennie and Church 2010). aDcp data have also been used directly in some other studies to estimate the mixing coefficient (Carr and Rehmann 2007, Shen et al. 2010, Kim 2011 ). In order to reduce the computational cost and errors caused by simulating a velocity field, in the present study a novel practical approach that couples field measurements and a numerical model is proposed. Essentially, instead of a simulated velocity field, the velocity field measured with an aDcp is used to solve the advection-diffusion equation (1). This maximizes the use of real field-measured data instead of calculating velocities indirectly. The proposed methodology is meant to minimize errors and enhance accuracy while keeping a reasonable computational cost, as described in Section 4.2.3. The use of the proposed coupled field work-modelling approach in this study enabled us to efficiently simulate mixing in an 83 km reach of the North Saskatchewan River for a duration of three days, using an ordinary computer.

This paper is organised as follows. In Section 4.2.2, a summary of the field work is presented. Analytical approaches and the novel numerical modelling approach for estimation of transverse mixing coefficient are explained in Section 4.2.3. Results and discussions are presented in Section 4.2.4, and some concluding remarks in Section 4.2.5 complete the study.

### 4.2.3 Field work

This study uses tracer concentration, depth-averaged velocity, shear velocity, and bathymetry data, which are provided in Chapter three. The field campaign was carried out for three days, from October 26 to October 28, 2011, in the North Saskatchewan River downstream from the Capital Region Wastewater Treatment Plant over a total distance of 83km from the outfall. Rhodamine WT was injected as a neutral tracer at the outfall with a peristaltic pump for 13 hours at the rate of 64 mg/s. The survey was begun about 3 hours after the injection started. Comparing the duration of the injection and the duration of the field campaign shows that we are dealing with an unsteady case in this study. Rhodamine WT concentrations were measured in real time at 17 surveyed sections (Fig. 4.2.1) with an *in situ* fluorometer connected to a CTD system linked to a computer in order to measure and record concentrations, with a sampling frequency of 4 Hz. An acoustic Doppler current profiler (aDcp) was also used simultaneously to measure depth and velocity in the surveyed sections.

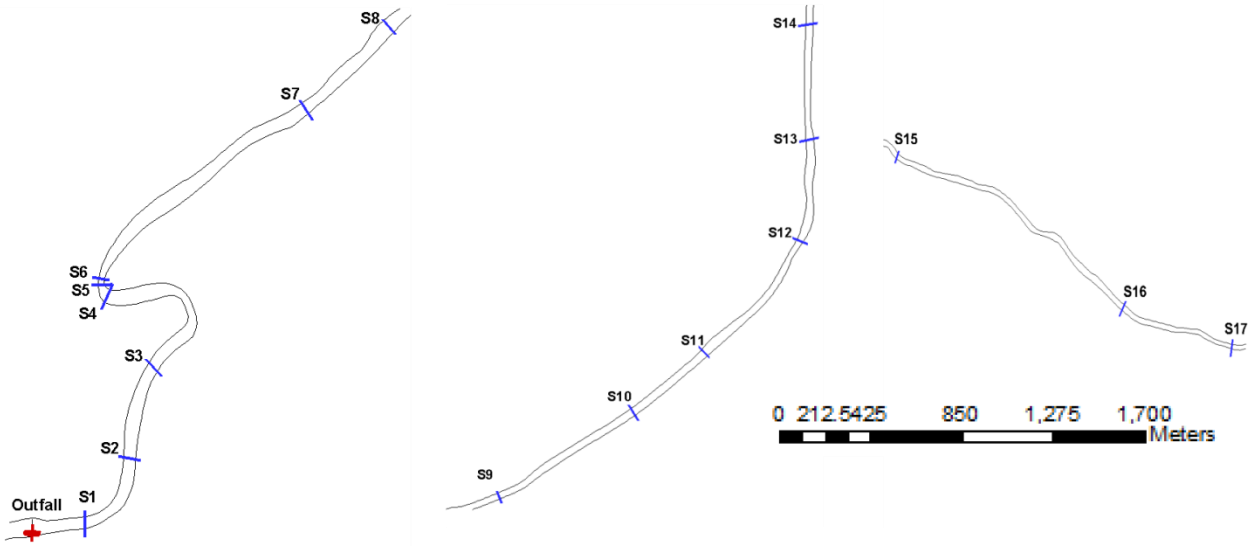


**Figure 4.2 a) Sections surveyed on October 26; b) Sections surveyed on October 27; c) Sections surveyed on October 28**

At each section, the surveyed path was recorded using a survey-grade dual-frequency real-time kinematic (RTK) Global Differential Positioning System. The GPS recorder data were integrated with the data collected by the aDcp and fluorometer. The spatial location of the surveyed sections as well as the survey dates have been provided in Table (4.2.2). The details of the equipment employed, field work, and post-processing procedures, including the shear velocity calculation method as well as the collected data sets, can be found in Chapter three.

**Table 4.2: Summary of the surveyed section information**

| Date | Section | Distance from the outfall (km) | Time |
|---|---|---|---|
| October 26 | S1 | 0.74 | 13:45 |
| | S2 | 2.3 | 14:12 |
| | S3 | 3.5 | 15:10 |
| | S4 | 6.5 | 15:39 |
| | S5 | 6.5 | 15:50 |
| | S6 | 6.5 | 16:00 |
| | S7 | 10 | 16:30 |
| | S8 | 12 | 17:07 |
| | S9 | 39 | 17:29 |
| | S10 | 44 | 17:05 |
| October 27 | S11 | 47 | 13:44 |
| | S12 | 52 | 16:10 |
| | S13 | 55 | 15:45 |
| | S14 | 59 | 15:16 |
| October 28 | S15 | 66 | 14:17 |
| | S16 | 78 | 15:28 |
| | S17 | 83 | 16:00 |

The average values of the measured concentrations were calculated in 40 stream tubes across the surveyed sections and plotted versus the numerical model results. Due to the shallow water depth, there

were some sections where the fluorometer system could not be submerged in the water for the whole section, and thus, no *in situ* Rhodamine WT concentration data are available for those parts of the section.

### 4.2.4 Modelling

#### 4.2.4.1 Analytical model (method of moments)

The approximate length of the injected tracer plume in this study during the field survey period was about 25 km (see Chapter three). Consequently, as the plume is convected with a non-uniform velocity across the river, the position of the surveyed section within the plume varies as a function of the time of survey (see Fig. 5 in see Chapter three). Only the sections surveyed in the middle of the plume [S1, S2, S3, S9] were not influenced by the differential advection; i.e., in these sections, both the center and edges of the plume have reached but not yet passed the channel section (see Chapter three). In sections within the middle of the plume, the standard (Yotsukura and Sayre 1976) and generalized (Beltaos 1980, Rutherford 1994) methods of moments, with the assumption of a steady source condition, can be used for analysing the tracer concentration. These methods assume a uniform velocity and depth in the river as simplifying assumptions, and employ the analytical solution for the steady form of (4.2.1) in the stream tube coordinate system without considering the longitudinal dispersion.

$$u\frac{\partial C}{\partial x} = \frac{\partial}{\partial q} D(\frac{\partial C}{\partial q}) \qquad \textbf{(4.2.1)}$$

In (2), $x$ is the distance of the section from the outfall and D is the factor of diffusion. At any point $Y_0$ across the section, $q(Y_0) = \int_o^{Y_0} uhdy$ is the cumulative discharge across the section, and was constructed using the measured depth-averaged streamwise velocity ($u$) and local depth ($h$) provided in Chapter three.

Employing either the standard or generalised methods of moments requires having the cross-sectional distribution of the tracer concentration. Concentration measurement is greatly affected by measurement errors, especially at the edges of the transverse tracer profile. Hence, Rutherford (1994) advised dropping

or smoothing out the points with an order of magnitude difference in tracer concentration from the neighbouring points in the measured tracer profile before calculating the variance, which is required for the analysis methods.

Fitting the measured concentration in a section onto the analytical solution of Eq. (4.2.2) provides the average transverse mixing coefficient between the outfall and the section. Moreover, the tracer concentration for unmeasured sections can be obtained by using the fitted solution. For sections where the tracer has not reached the opposite bank, the analytical solution for (4.2.2) is:

$$C = \frac{2M_0}{\sqrt{4\pi Dx}} \exp\left(\frac{-q^2}{4Dx}\right) \qquad \textbf{(4.2.2)}$$

where $M_0$ is the injected mass rate at the bank discharge. Assuming a small variation in the transverse dispersion coefficient across the section (Lau and Krishnappan, 1981), the factor of diffusion can be considered as constant in a given section and is calculated as:

$$D = \psi k_\beta U H^2 \qquad \textbf{(4.2.3)}$$

where $\psi$ is the shape factor parameter

$$\psi = \frac{1}{W} \int_{y=0}^{W} \left(\frac{h}{H}\right)^2 \frac{u}{U} dy \qquad \textbf{(4.2.5)}$$

in the range of 1.0-3.6 (Sayre 1979, Beltaos 1980), $k_\beta$ is transverse dispersion coefficient, and $H$ and $U$ are the average depth and velocity. Equation (4.2.3) is in the form of a Gaussian distribution and shows that, assuming steady conditions and no boundary effects, transverse mixing of the tracer follows a Gaussian distribution.

For sections where the tracer has reached the opposite boundary, the analytical solution can be modified by taking the wall boundary effects as virtual sources and superimposing their distribution effect on the actual initial point source (Fischer, 1979).

The standard method of moments assumes a constant dispersion coefficient, uniform channel, and steady source. This method is applicable before the point where the tracer impinges on the opposite bank and the bank boundary starts to affect the tracer distribution. This method underestimates *D* where flow converges and overestimates it in regions of diverging flow. In regions of converging flow, negative values for transverse dispersion are also possible (Rutherford, 1994). Before the impingement point, the transverse mixing follows a Gaussian distribution, and the factor of diffusion (*D*) is calculated based on the change in plume size for different sections along the river path.

$$D = \frac{1}{2}\frac{d\sigma_q^{\,2}}{dx} \qquad \textbf{(4.2.4)}$$

The $\sigma_q^{\,2}$ parameter represents the plume size and is defined as the variance of the *C*-*q* profile. The standard method of moments assumes a linear increase in tracer variance in relation to distance from the outfall, as:

$$\sigma_q^{\,2} = \frac{1}{M_0}\int_{q=0}^{Q} q^2 C dq \qquad \textbf{(4.2.5)}$$

In the current study, the tracer concentration was observed at the downstream left bank at a sharp bend 6.5 km from the injection point. The tracer does not follow a Gaussian distribution after this section, so the generalized method of moments should be used for analyzing the tracer in the sections after the sharp bend. The generalised method of moments can handle non-uniformity in the channel as well as the effect of tracer impingement on the banks, and in this method, the $\sigma_q^{\,2}$ parameter is calculated as:

$$\sigma_q^{\,2} = 2D\int_0^x f(x)dx \qquad \textbf{(4.2.6)}$$

where *f(x)* deals with variations in concentration across the section. Note that the standard method of moments is obtained by setting *f(x)*=1 in (4.2.8). The general formula for *f(x)* (Rutherford, 1994) is written as:

$$f(x) = \frac{\int_{q=0}^{Q} q\varphi(q)\frac{\partial C(x,q)}{\partial q}dq}{\int_{q=0}^{Q} C(x,q)dq} \qquad \textbf{(4.2.7)}$$

In (4.2.9), parameter $\varphi(q)$ describes the variation of $D$ across the section. Considering a constant dispersion coefficient across the section would lead to $\varphi(q)$=1 in (4.2.9).

Estimation of variance from (4.2.9) requires the integration of $f(x)$ between two consecutive sections. Following Rutherford (1994), in order to estimate the integral value, an exponential decrease in $f(x)$ between sections has been assumed. In the current study, only 4 surveyed sections (S1, S2, S3, and S9) were found to be not influenced by the differential advection and eligible for the use of methods of moments to analyze the tracer data. All the remaining 13 surveyed sections were located towards the front or rear of the plume, where the mixing should be considered as an unsteady process. This constraint actuated us toward using the numerical approach. It should be noted that both the standard and general methods of moments may lead to unreasonable values, such as negative values for mixing coefficients, due to difficulties in the sampling methods leading to unreasonable calculated values of variance of the concentration distributions.

#### 4.2.4.2 Numerical model

Due to the non-uniformity in velocity distribution, differential advection affects the mixing process, especially in the case of non-continuous injection. In such cases, a numerical approach is often preferred. The distribution of depth and velocity throughout the river channel are the basic parameters required for employing a numerical model.

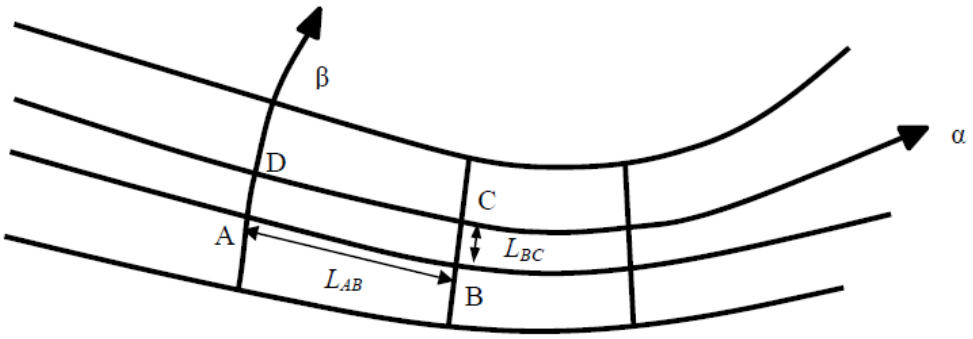


**Figure 4.3: Stream tube orthogonal coordinate system in a meandering river**

**Numerical model equations**

As previously stated, in this study the governing equation (4.2.1) has been transformed to the stream tube orthogonal curvilinear gridding system (Fig. 4.2.2), where $\alpha$ is the streamwise coordinate and $\beta$ is the transverse coordinate. The resulting equation (Rutherford 1994) is written as:

$$\frac{\partial C}{\partial t}+\frac{v_\alpha}{m_\alpha}\left(\frac{\partial C}{\partial \alpha}\right)=\frac{1}{h m_\alpha m_\beta}\left[\frac{\partial}{\partial \alpha}\left(\frac{m_\beta}{m_\alpha}hk_\alpha\frac{\partial C}{\partial \alpha}\right)+\frac{\partial}{\partial \beta}\left(\frac{m_\alpha}{m_\beta}hk_\beta\frac{\partial C}{\partial \beta}\right)\right]+R \qquad \textbf{(4.2.8)}$$

where $C$ is depth-averaged concentration, $v_\alpha$ is depth-averaged velocity along the river path, $h$ is water depth, $k_\alpha$ and $k_\beta$ are the longitudinal and transverse mixing coefficients respectively, and $\alpha$ and $\beta$ represent the transformed coordinates (Fig. 4.2.2). Parameters $m_\alpha$ and $m_\beta$ are metric coefficients in the stream tube orthogonal coordinate system and are calculated from the distances ($L$) between grid points as:

$$m_\alpha=\frac{L_{CD}}{L_{AB}} \qquad \textbf{(4.2.9)}$$

$$m_\beta=\frac{L_{BC}}{L_{AD}} \qquad \textbf{(4.2.10)}$$

As the tracer flows and mixes in the river, it adsorbs to the bed material, and the injected mass decreases along the river. This process is represented by the sink term $R$ in (4.2.10). The longitudinal mixing coefficient ($k_\alpha$) is another important parameter which is required for solving equation (4.2.10). Following Fischer et al. (1974), in this study the longitudinal mixing coefficient was calculated as:

$$k_\alpha = \frac{I}{W k_\beta} \qquad \textbf{(4.2.11)}$$

$$I = -\int_0^W u' \int_0^y \int_0^y u' dy dy dy \qquad \textbf{(4.2.12)}$$

In equation (4.2.13), $W$ is the cross section width and $u'$ is the deviation of the depth-averaged velocity from the cross-sectional mean velocity obtained from the field-measured data. The required transverse mixing coefficient ($k_\beta$) in (4.2.13) was taken from the initially calibrated numerical model without longitudinal mixing. The approach of employing equation (4.2.13) has been adopted in various previous studies for estimating the longitudinal mixing (e.g., Seo and Baek 2004, Kim 2011).

In order to reduce computational costs, the momentum equation is not solved in the proposed method. The velocity, depth, and discharge field are generated by a linear interpolation of measured values in the surveyed sections. Having the time history of unsteady discharge at each survey section from a 1D model (Appendix A), the velocity field is updated at each time step. The tracer mixing process is then calculated by solving (4.2.10) numerically. Using the measured tracer concentration, the numerical solution is then calibrated by varying the transverse mixing coefficient. The transverse mixing coefficients were estimated by calibrating the model results versus the measured concentrations, using the least squares method.

**Numerical discretization scheme**

As previously mentioned, longitudinal advection and transverse mixing are dominant in two-dimensional contaminant mixing in a meandering river. The second term on the left-hand side of (4.2.10) represents the longitudinal advection of the tracer mass. In order to reduce the numerical errors associated with advective transport, a high-order scheme was employed in this study for solving the advective mass transport. The developed numerical model employs a Finite Volume method and solves the advection part by using an explicit third-order upwind scheme (Mohammadian and Le Roux 2008). The diffusion part is explicitly solved by using the standard second-order centered scheme, and the advection and diffusion terms are solved separately within the solving procedure. The proposed method is first-order accurate in

time and respectively second- and third-order accurate in solving the diffusion and advection parts. The developed numerical model does not take into account the effect of islands. In order to minimize the computational cost, the maximum stable time step was used in this study ($\Delta t$=0.2 s).

The advection term in (4.2.10) can be written as:

$$\frac{v_\alpha}{m_\alpha}\left(\frac{\partial C}{\partial \alpha}\right)=\frac{\partial F}{\partial \alpha}-C\frac{\partial G}{\partial \alpha} \quad \textbf{(4.2.13)}$$

where

$$F=\frac{v_\alpha C}{m_\alpha} \quad \textbf{(4.2.14)}$$

$$G=\frac{v_\alpha}{m_\alpha} \quad \textbf{(4.2.15)}$$

Therefore, (4.2.10) may be written as:

$$\frac{\partial C}{\partial t}=-\frac{\partial F}{\partial \alpha}+C\frac{\partial G}{\partial \alpha}+\frac{1}{hm_\alpha m_\beta}\left(\frac{\partial N}{\partial \alpha}+\frac{\partial T}{\partial \beta}\right)+R \quad \textbf{(4.2.16)}$$

where

$$N=\frac{m_\beta}{m_\alpha}hk_\alpha\frac{\partial C}{\partial \alpha} \quad \textbf{(4.2.17)}$$

$$T=\frac{m_\alpha}{m_\beta}hk_\beta\frac{\partial C}{\partial \beta} \quad \textbf{(4.2.18)}$$

For the cell ($i$,$j$) at a given time step ($n$), the depth-averaged concentration is represented by $C_{i,j}^{n}$. The concentration field is first calculated as a result of the advection process in an intermediate time step for the whole computational domain. Removing the diffusion term from (4.2.18), and using the finite volume method for an arbitrary region ($\Omega$), one obtains:

$$\frac{\partial}{\partial t}\int_{\Omega} C d\alpha d\beta + \int_{\Omega}\left(\frac{\partial F}{\partial \alpha} - C\frac{\partial G}{\partial \alpha}\right) d\alpha d\beta - \int_{\Omega} R d\alpha d\beta = 0 \qquad \textbf{(4.2.19)}$$

Using the finite volume method, the explicit discretization of (4.2.21) can be written as:

$$\frac{\left(C^{*}_{i,j} - C^{n}_{i,j}\right)A_{i,j}}{\Delta t} = \left[F^{n}_{i+1/2,j}\Delta\beta_{i+1/2,j} - F^{n}_{i-1/2,j}\Delta\beta_{i-1/2,j}\right] - C^{n}_{i,j}\left[G^{n}_{i+1/2,j}\Delta\beta_{i+1/2,j} - G^{n}_{i-1/2,j}\Delta\beta_{i-1/2,j}\right] + R_{i,j}$$

**(4.2.20)**

with $A_{i,j} = \Delta\alpha_{i,j}\Delta\beta_{i,j}$ , where $\Delta\alpha_{i,j}$ and $\Delta\beta_{i,j}$ are the grid sizes at cell $(i,j)$ in the $\alpha$ and $\beta$ directions respectively. $F^{n}_{i+1/2,j}$ represents the numerical advection flux, which is calculated using a third-order upwind scheme (Mohammadian and Le Roux, 2008) as explained in Appendix B. In (4.2.22), $C_{i,j}^{*}$ represents the intermediate concentration at cell $(i,j)$. Equation (4.2.22) leads to:

$$C^{*}_{i,j} = C^{n}_{i,j} + \frac{\Delta t}{A_{i,j}}\left[F^{n}_{i+1/2,j}\Delta\beta_{i+1/2,j} - F^{n}_{i-1/2,j}\Delta\beta_{i-1/2,j}\right] - \frac{\Delta t C^{n}_{i,j}}{A_{i,j}}\left[G^{n}_{i+1/2,j}\Delta\beta_{i+1/2,j} - G^{n}_{i-1/2,j}\Delta\beta_{i-1/2,j}\right] + \frac{\Delta t}{A_{i,j}}R_{i,j}$$

**(4.2.21)**

The result of the advection part ($C_{i,j}^{*}$) is then used for solving the diffusion part. This will eventually lead to the depth-averaged concentration as a result of both the advection and diffusion processes $C_{i,j}^{n+1}$. Removing the advection and source terms from (4.2.18) and using the finite volume method, one obtains:

$$\frac{\partial}{\partial t}\int_{\Omega} C d\alpha d\beta + \int_{\Omega}\left(\frac{\partial N}{\partial \alpha} + \frac{\partial T}{\partial \beta}\right) d\alpha d\beta = 0 \qquad \textbf{(4.2.22)}$$

Equation (4.2.24) can be rewritten as:

$$\frac{\left(C^{n+1}_{i,j} - C^{*}_{i,j}\right)A_{i,j}}{\Delta t} = \left[N^{n}_{i+1/2,j}\Delta\beta_{i,j} - N^{n}_{i-1/2,j}\Delta\beta_{i,j} + T^{n}_{i,j+1/2}\Delta\alpha_{i,j} - T^{n}_{i,j-1/2}\Delta\alpha_{i,j}\right] \textbf{(4.2.23)}$$

Therefore, the concentration value for cell $(i,j)$ as a result of advection-diffusion at time step $n+1$ is finally calculated as:

$$C^{n+1}_{i,j} = \frac{\Delta t\Delta\beta_{i,j}}{A_{i,j}}\left[N^{n}_{i+1/2,j} - N^{n}_{i-1/2,j}\right] + \frac{\Delta t\Delta\alpha_{i,j}}{A_{i,j}}\left[T^{n}_{i,j+1/2} - T^{n}_{i,j-1/2}\right] + C^{*}_{i,j} \qquad \textbf{(4.2.24)}$$

**Model setup and boundary conditions**

An orthogonal curvilinear grid of 4000*40 cells was used in this study, where 40 is the number of stream tubes across the section. In order to minimize the numerical errors and computational cost, the number of cells in the longitudinal and horizontal directions was chosen based on sensitivity analysis on the grid size. The gridding system was generated in 4 steps. In the first step, the entire surveyed reach was split into 4000 equal intervals along the studied reach. In order to eliminate the effect of local bed features on the entire depth field, the grid dimension was not refined further across the river section. Figure (4.2.3) shows part of the gridding system at the sharp bend.

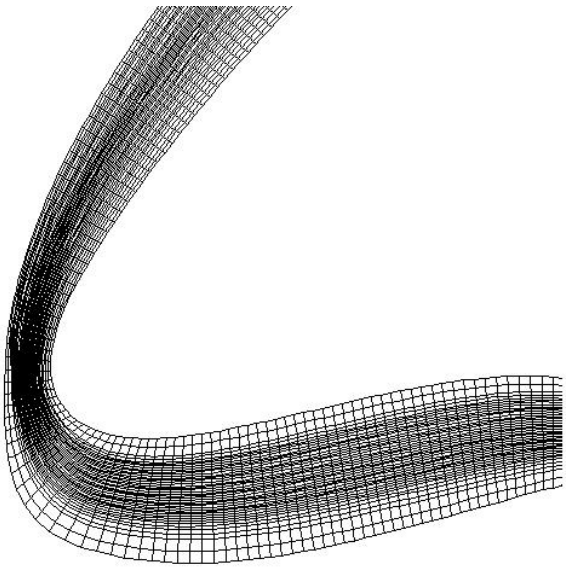

**Figure 4.4: Stream-tube orthogonal gridding system at the sharp bend**

In order to simplify the solution by eliminating the metric coefficients corresponding to the transverse velocity field, in this study governing equation was solved in an orthogonal coordinate system. This was achieved by specifying channel sections orthogonal to the banks throughout the domain; the cross-section line and associated boundary coordinates were rotated around its center point to provide an orthogonal coordinate system line and boundary coordinates that are perpendicular to the river path. With the velocity and depth field, the cross section was then split into 40 stream tubes. Finally, the obtained grid

was orthogonalised to obtain a stream-line orthogonal mesh. Details of orthogonal curvilinear grid generation in stream tube coordinates can be found in Section 4.1.

The measured concentration profile at the first surveyed section from the outfall (0.74km) was used as the left (upstream) boundary condition in (4.2.10). The fully developed condition (zero gradient) was used as the right (downstream) boundary condition. With respect to bank sides, the wall boundary condition (zero flux) has been implemented. As previously mentioned, the depth and velocity field have been provided by linear interpolation between the surveyed sections.

### 4.2.5 Results and discussion

The model results and measured data are presented in Figs. (4.2.4) and (4.2.5) for the river sections downstream of the outfall location. As the outfall was located on the right bank (facing downstream) of the river ($q_0=0$), the maximum measured tracer concentrations were found at the location of discharge. The maximum tracer concentration declined gradually along the river path as the tracer mixed with ambient water. The numerical model results are shown for the surveyed sections in Fig. (4.2.4).

The numerical model results were obtained at 40 points across each section. Although some discrepancies are observed in Fig. (4) between the measured and modeled results for the sections close to the outfall, the value of the average $r^2$=0.82 for the calibrated model shows that the model results are generally in good agreement with the measured data. The difference between the measured and modeled results for the sections close to the outfall could be attributed to the effect of various influencing processes such as dead zones (Putz and Smith 1998). This was the case in the direct observations in the present project as well because during the field survey, the bank was found to be fairly irregular, especially in the region close to the outfall, where the tracer concentration was also higher. The generated embayment caused accumulation of the tracer in this region, leading to a difference between the modeled and measured data.

In most natural channels, the main flow meanders along the channel path. The irregularities in bed formation caused by the meandering flow will generate transverse currents, especially at sharp bends (Blanckaert, 2011, Kashyap et al., 2012). This transverse velocity will move the body of the tracer back and forth within the channel section. In this study, the transverse current at the sharp bend has accelerated the movement of tracer towards the downstream left bank. The plume was observed to reach the opposite bank 6.5 km downstream of the outfall at the sharp bend. Due to high channel non-uniformities at the sharp bend, equilibrium between the velocity shear and turbulent diffusion is not attained. Thus, the concentration profile is skewed at the sharp bend and does not follow a normal Gaussian distribution (Figs. 4d and 4e for S4 and S5, respectively), and the analytical solution is therefore no longer applicable. The sharp bend also had a great influence in enhancing the mixing mechanism. The higher transverse mixing coefficient obtained from the numerical model (Table 4.2.3), especially in the end part of the bend (S5-S6), can be attributed to the presence of secondary flows and their dominance in the mixing process, which has also been reported in different studies such as Baek and Seo (2010). As another example, Seo et al. (2008) reported that in the case they studied, the dispersion coefficient in the apex was four times larger than in the straight region.

**Table 4.3: Summary of numerical model results for longitudinal and transverse mixing coefficients**

| Section | $D_{x\,(m^2/s)}$ | $D_{y\,(Numerical)(m^2/s)}$ |
|---|---|---|
| S1-S2 | 168 | 0.015 |
| S2-S3 | 288 | 0.03 |
| S3-S4 | 164 | 0.03 |
| S4-S5 | 11 | 0.06 |
| S5-S6 | 0.8 | 0.9 |
| S6-S7 | 192 | 0.01 |
| S7-S8 | 134 | 0.02 |
| S9-S10 | 104 | 0.07 |
| S10-S11 | 525 | 0.001 |
| S11- S13 | 525 | 0.01 |
| S13-S14 | 525 | 0.02 |
| S14-S15 | 525 | 0.03 |
| S15-S16 | 396 | 0.03 |
| S16-S17 | 102 | 0.04 |

In Fig. (4.2.4), three graphs have been provided, for the beginning (S4), middle (S5), and end (S6) of the sharp bend. Although the present numerical model did not reproduce the very fast response of the plume to the transverse currents in bends (Figs. 4.2.4d, 4.2.4e, and 4.2.4f), the discrepancy between the centroid location of the measured and modeled profiles has been significantly reduced by the time it reaches section S8. This shows that the employed gridding system has been successful in considering the influence of transverse velocity.

In natural rivers, topographic steering causes higher depth-averaged velocity along the thalweg stream line (Dietrich and Smith, 1983). In the present study, the thalweg was located in the channel centre for most of the surveyed North Saskatchewan River reach. As expected, increased depth-averaged velocities were observed in the center of each section (see Chapter three). Between the outfall and S8, the average flow velocities in the right bank stream tube and the one located in the middle of the section were 0.38 and 0.7 m/s respectively. As the thalweg was located in the middle of each section for most of the river, the tracer plume reached the middle part of each section sooner (see Chapter three). Considering the tracer injection starting time (10:30 AM on 26 of October) as well as the distance of the surveyed sections from the outfall and the time of the measurement (Table 4.2.2), it can be concluded that in some of the surveyed sections the tracer plume had not reached the steady state condition at the time of the measurement. For instance, in Section S4, which was located about 6.5km downstream from the outfall, and was surveyed about 5 hours after starting the injection, the tracer travel time in the right bank stream tube shows that the plume had just reached the right bank part of S4 at the time of the survey. This is also most clearly seen in sections S7 and S8. The tracer plume could not have reached the right bank part of the surveyed section at the time of the survey, which explains the measured sectional distribution of tracer concentration at these sections (Figs. 4.2.4g and 4.2.4h). In other words, sections such as S7 and S8 were located towards the front of the plume at the time of measurement. This is the reason for observing a higher maximum concentration in some downstream sections (such as S9, surveyed in the middle of the plume), than at sections further upstream (S7 and S8, which were located at the front of the plume at the

time of the survey). As previously mentioned, the tracer was injected for 13 hours at the outfall location. Therefore, for sections S13 to S17, surveyed on October 29 and located in the rear part of the plume, the tracer concentration in the middle part of the section was lower than the bankside concentration. Again, this is due to the higher advection velocity in the middle part of the section, as was explained above. The last surveyed section (S17) was located 83km from the outfall. The small difference between the tracer concentrations at the middle and the downstream left bank demonstrates that the section was close to the middle of the plume at the time of the survey.

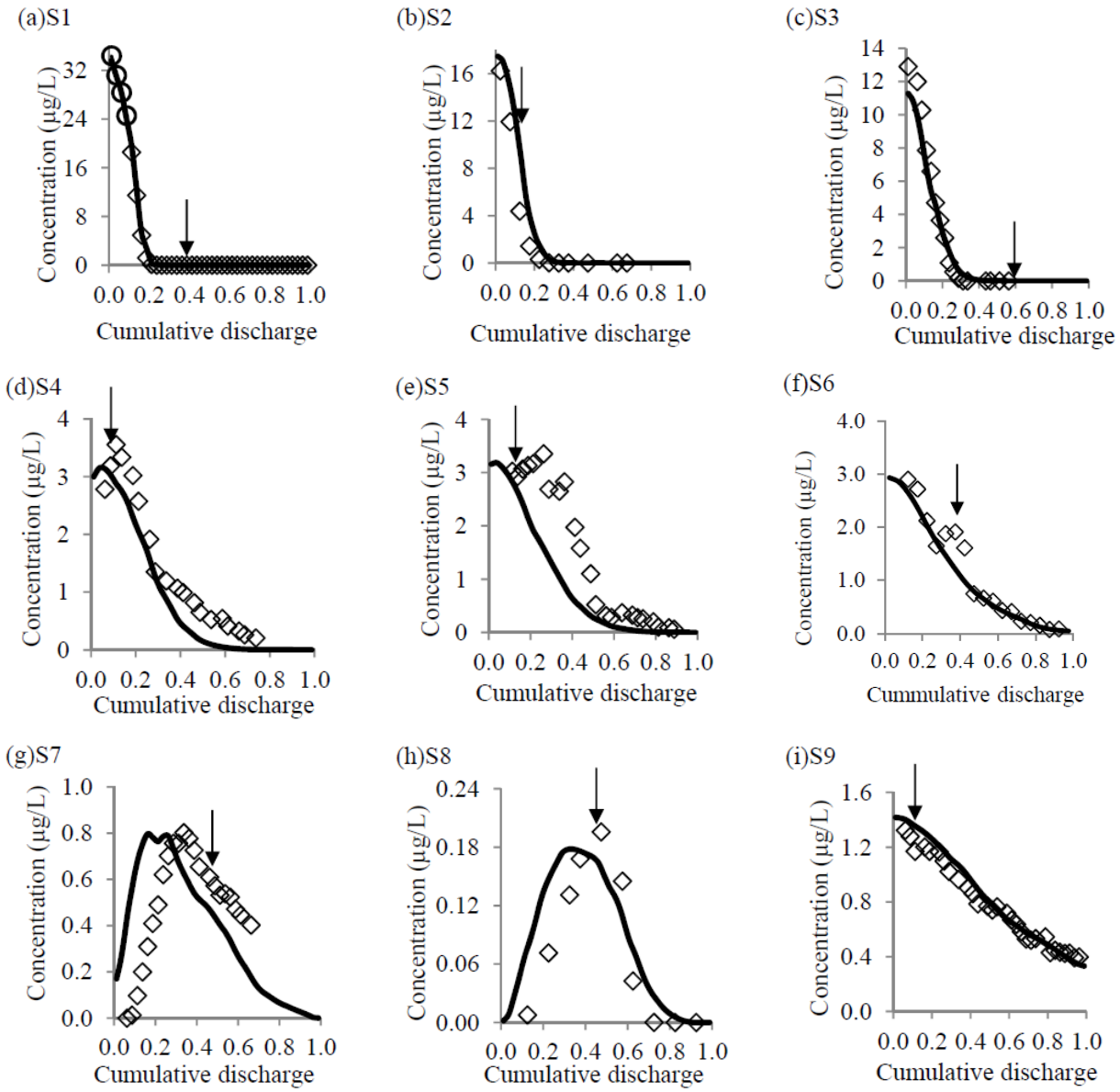

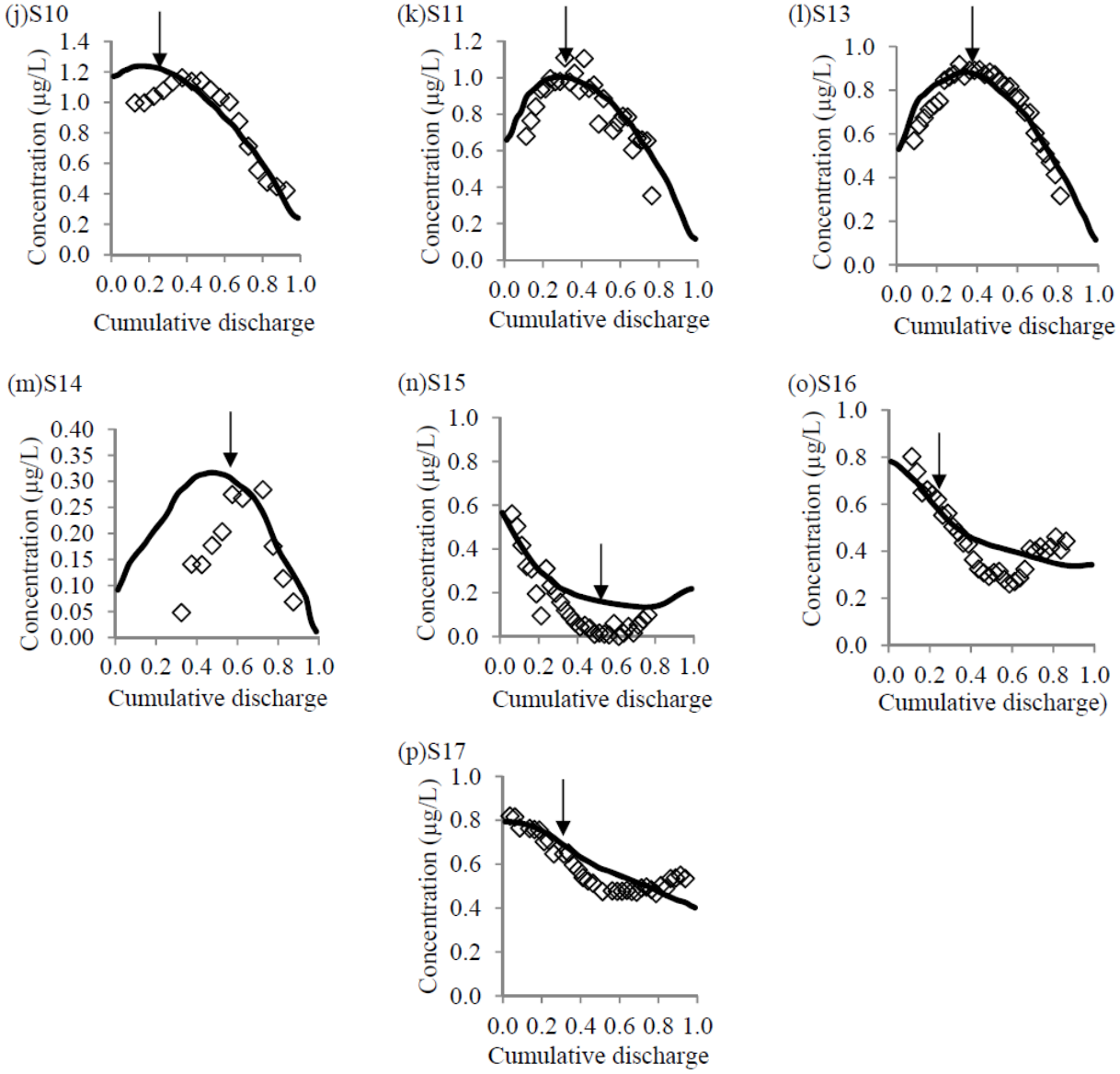


**Figure 4.5 : Numerical model and measured tracer concentration for surveyed sections S1 through S17. Discrete points represent measured data across the section, and the solid line represents the numerical model results (note that circles indicate the extrapolated points and arrows show the thalweg location). The x axis represents the normalized cumulative discharge across a section. The tracer concentration is shown on the y axis (in µg/l).**

The analytical model has only been used for the sections located at the middle of the injected plume at the time of the survey (S1, S2, S3 and S9). The modeled and measured results are presented for five sections in Fig. (4.2.5). The model graphs are a result of fitting the analytical solution of (4.2.2) on the

measured data. In order to show the effect of local bed features on the mixing process, the measured tracer data at S3 are presented for two sequential sections S3_1 and S3_2 in Fig. (4.2.5) (note that Fig. (4.2.4) shows the results at the S3_2 section). The continuous graphs from the analytical solutions were used to provide the concentration values needed in the standard and generalized methods of moment.

The calculated transverse mixing coefficients using analytical models are provided in Table (4.2.3) and Table (4.2.4). The transverse mixing coefficient provided for each section represents the average transverse mixing coefficient between that section and the next section. The estimated transverse mixing coefficient results from both the analytical and numerical approaches confirm Dow et al.'s (2009) conclusion that the mixing rate is highly variable along a meandering river.

In sub-reaches S1-S2 and S2-S3, the transverse mixing coefficients estimated from the analytical model are lower than those from the numerical model. But in sub-reach S3-S9, which is also longer, the obtained values from the numerical (0.08, Table 4.2.6) and analytical models (0.082, Table 4.2.4) are similar. The simplifying assumptions in the analytical model (eg. small local changes in depth and velocity values in equations 4.2.4 and 4.2.5) were not the case based on our direct observations. Moreover, the dead zones, which absorbed a part of injected tracer, are not included in the analytical model, but were observed close to the outfall. Since the assumptions of the model are clearly not accurate in this project, it could be reasonable to include them as potential reasons for discrepancy, among various other possible reasons, such as data collection errors.

**Table 4.4: Summary of analytical model results for transverse mixing coefficients**

| Sub-reach | $D_y$ ($m^2/s$) |
|---|---|
| S1-S2 | 0.0075 |
| S2-S3 | 0.01 |
| S3-S9 | 0.082 |

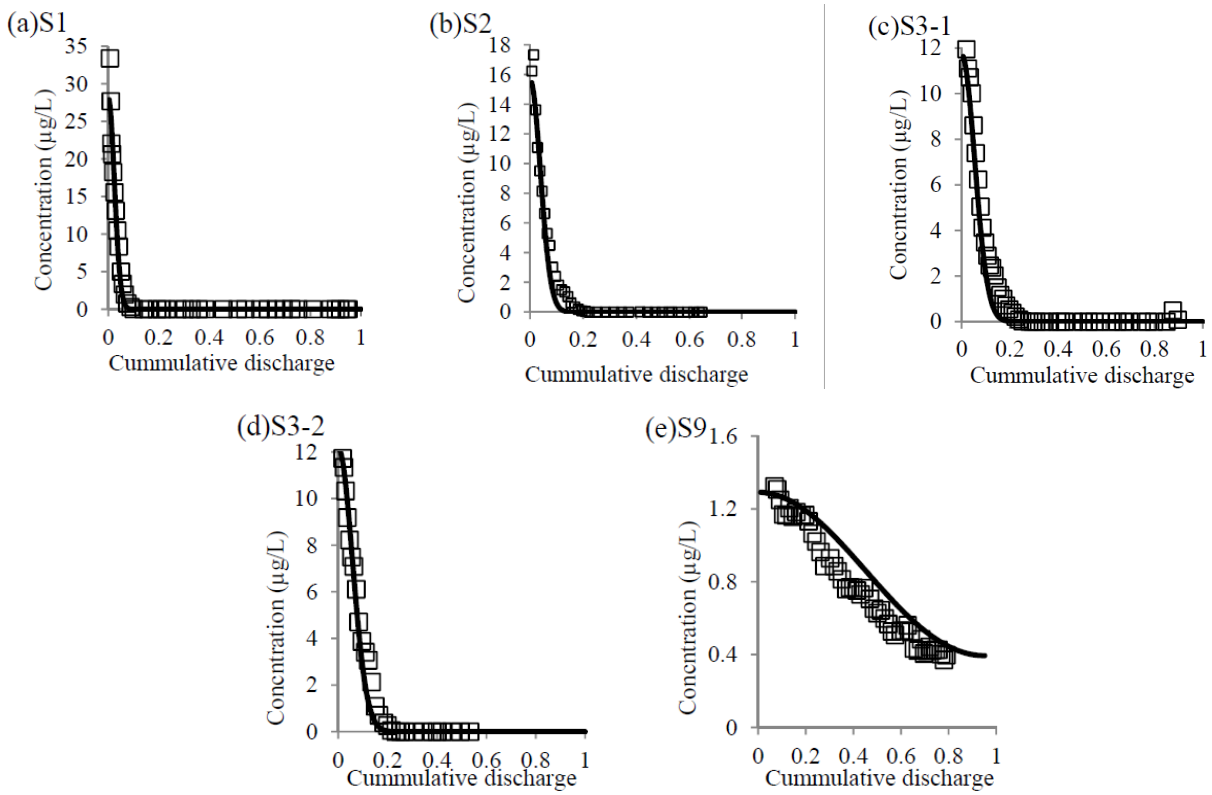


**Figure 4.6:Analytical solution and measured data for surveyed sections. Discrete points represent measured data across the section, and the solid line represents the analytical model results.**

At 3.5 km from the outfall (Section S3), two consecutive sections are shown in Fig. (4.2.6), where the transverse profiles of the depth-averaged velocity and depth are presented. The first measured section (S3_1) has a higher velocity gradient across the section. The average transverse mixing coefficient from the fitted curve and the average measured shear velocity were also found to be higher for section S3_1 than for section S3_2 (see Chapter three). This could be explained by the higher gradient in the transverse velocity profile. It also shows that in addition to the effective general parameters on transverse mixing discussed in the introduction section, local bed features have a great influence on the mixing coefficient.

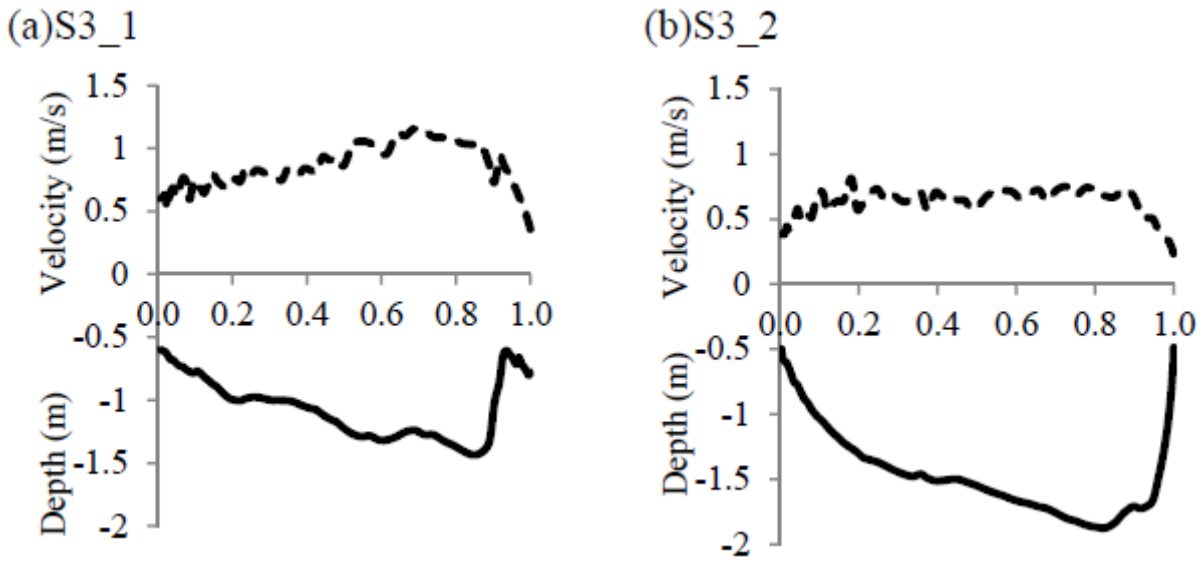


**Figure 4.7:Velocity (m/s, dashed line) and depth (m, solid line) at section S3**

Table (4.2.3) also provides the calculated longitudinal mixing coefficients for the surveyed sub-reaches from (14). The average longitudinal mixing coefficient for the surveyed reach is $D_x/(WU^*)$=33, corresponding to $D_x$=290 $m^2/s$, which falls within the range $2<D_x/(WU^*)<50$ and $0.2< D_x <1500$ $m^2/s$ mentioned in the field data reported in Rutherford (1994). It should be mentioned that the obtained value for $D_x$ is within an order of magnitude of the values estimated by some available empirical equations in the literature, such as Fischer's (1967) method, which leads to $D_x$ =1500 $m^2/s$ for this case. The observed difference could be attributed to the fact that some empirical equations for the estimation of the longitudinal mixing coefficient, such as Fischer's (1967) method, have been developed based on Taylor's dispersion theory. The main drawback of these formulas is that they have been obtained based on the link between longitudinal and transverse mixing coefficients by using a general estimation of the transverse mixing coefficient. Such general estimations of transverse mixing coefficients are not applicable in all cases, leading to inaccuracy in estimations for longitudinal mixing coefficients that are based on transverse mixing coefficients. More research is required to obtain better empirical equations.

**Table 5: Summary of hydraulic parameters for surveyed sub-reaches**

| Surveyed Date | Subreach | Average velocity (m/s) | $S_n$ | Average depth (m) | Average roughness (m) | Average width (m) | Average shear velocity |
|---|---|---|---|---|---|---|---|
| October 26 | S1-S8 | 0.66 | 1.3 | 1.15 | 0.25 | 141 | 0.06 |
| October 27 | S9-S14 | 0.50 | 1.09 | 1.56 | 0.26 | 151 | 0.05 |
| October 28 | S15-S17 | 0.68 | 1.03 | 1.28 | 0.27 | 165 | 0.08 |

Using the average hydraulic parameters from Chapter three(Table 4.2.5) for a given sub-reach, including the entire surveyed reach, the corresponding average transverse mixing coefficient was calculated from the empirical prediction methods of Bansal (1971) and Jeon et al. (2007) (Table 4.2.1). Furthermore, following Rutherford (1994) and using the transverse mixing coefficients for 15 sub-reaches from the calibrated numerical model (Table 4.2.3), the average transverse mixing coefficient over the various sub-reaches has been calculated (Table 4.2.6) as:

$$\overline{D_y} = \frac{1}{L_r}\sum_{i=1}^{M} D_{yi}\Delta x_i \qquad \textbf{(4.2.25)}$$

where $\overline{D_y}$ is the average transverse mixing coefficient, $D_{yi}$ = transverse mixing coefficient within each sub-reach $i$, $\Delta x_i$ = length of the sub-reach $i$, $M$=total number of sub-reaches, and $L_r$= total surveyed length in the river (Table 4.2.2).

Note that Table (4.2.6) also provides the average transverse mixing coefficient from both the steady and unsteady versions of the numerical model. In the steady version, the velocity field was assumed as steady and was not updated in each time step. Comparing the numerical model results from the two versions shows that the estimated transverse mixing coefficients differed by up to 75% in some sub-reaches.

However, the average transverse mixing coefficient for the entire surveyed reach in the unsteady version is only about 13.5% less than in the steady version.

**Table 4.5:Average hydraulic and transverse mixing parameters for surveyed sub-reaches**

| Section | $\overline{U}^*$ (m/s) | $\overline{U}$ (m/s) | $\overline{b}$ (m) | H (m) | $S_n$ | $\overline{D_y}$ $m^2/s$ | $\overline{D_y}$ $m^2/s$ | $\overline{D_y}$ $m^2/s$ | $\overline{D_y}$ $m^2/s$ |
|---|---|---|---|---|---|---|---|---|---|
| S1-S17 | 0.06 | 0.86 | 145 | 1.48 | 1.30 | 0.037 | 0.042 | 0.0423 | 0.170 |
| S3-S9 | 0.06 | 0.88 | 135 | 1.47 | 1.35 | 0.08 | 0.067 | 0.0428 | 0.150 |
| S1-S8 | 0.06 | 0.66 | 141 | 1.15 | 1.30 | 0.024 | 0.025 | 0.031 | 0.185 |
| S9-S14 | 0.05 | 0.50 | 151 | 1.56 | 1.09 | 0.008 | 0.014 | 0.027 | 0.147 |
| S15-S17 | 0.08 | 0.68 | 165 | 1.28 | 1.03 | 0.03 | 0.025 | 0.035 | 0.296 |

The calculated average transverse mixing coefficient from the numerical model between S1 and S17 matched the estimated value from Jeon et al. (2007) very well. Similarly, for all sub-reaches, the transverse mixing coefficients estimated with the method proposed by Jeon et al. (2007) are of similar magnitude to those estimated with the numerical model. Furthermore, the Jeon et al. method produced transverse mixing coefficients of similar order for all the various sub-reaches, and thus it appears to be a reasonably stable prediction method. All methods estimated the lowest value for the transverse mixing coefficient in the sub-reach S9-S14, which can be attributed to lower average shear velocity, velocity, and sinuosity. Although sinuosity is greater in S1-S8 than in S15-S17, the estimated transverse mixing coefficients are very close in those two sub-reaches. This can be attributed to the higher shear velocity in S15-S17 compared to S1-S8, which compensates for the effect of lower sinuosity in S1-S8 on the total transverse mixing coefficient. The calibration of the numerical model yielded the highest transverse mixing coefficient in sub-reach S3-S9, which included the sharp bend. This can be attributed to the effect of the generated secondary flows at sharp bends in meandering rivers, which play a dominant role in

transverse mixing and lead to higher transverse mixing coefficient values in such regions. The results of Bansal's (1971) equation are much higher than the values estimated with the numerical model. The better performance of the method proposed by Jeon et al. (2007) compared with Bansal (1971) can be attributed to the fact that it is more comprehensive in terms of the parameters considered in estimating the mixing coefficient.

From the measured cross-sectional tracer profile and river discharge, the tracer mass flux was calculated using equation (4.2.28) at the surveyed sections (Fig.4.2.7) as.

$$M = \int_{q=0}^{Q} C \cdot dq \qquad \textbf{(4.2.26)}$$

where $Q$ is the total river discharge. As mentioned in Section 4.2.3.2, tracer sticks to the bed material while it flows and mixes in the river. This process, in addition to the variation of discharge, caused a non-linear decrease of tracer mass flux along the river. Note that these results were utilized to estimate the sink term ($R$) in the numerical model (see Eq. 4.2.11).

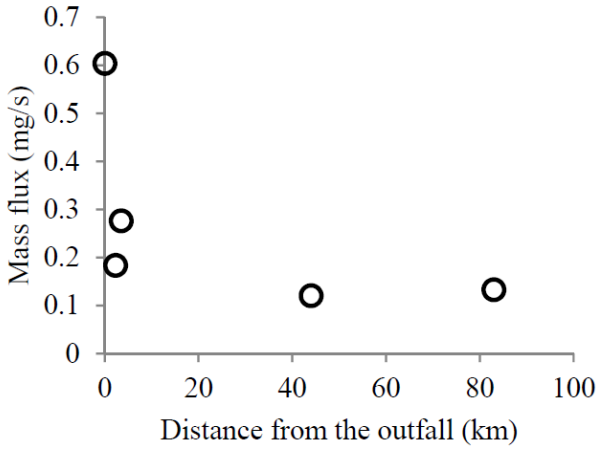


**Figure 4.8:Variation of the tracer mass flux along the river, based on sections S1, S2, S3, S9, S17**

### 4.2.6 Summary and conclusions

To better understand the environmentally important contaminant-mixing problem in natural rivers, the transverse mixing patterns of water and contaminants in a meandering river were studied using numerical and analytical approaches. A numerical model was developed for solving a depth-averaged two-dimensional advection-diffusion equation in a stream-tube orthogonal coordinate system. Due to the extended study region and in order to reduce the computational cost, a novel efficient method was proposed that coupled a numerical model with field data. Due to the availability of extensive field-measured data and in order to eliminate the metric coefficients of the general curvilinear coordinate system, the stream-tube orthogonal coordinate system was employed in the numerical model. The effect of the transverse velocity field was also eliminated in the employed stream-tube orthogonal coordinate system, which largely reduced the computational cost.

Comparing the modeled results and the field data, the transverse mixing coefficient was estimated for different sub-reaches within the study region. The results obtained from the numerical model showed that the transverse mixing coefficient can be highly variable along meandering rivers. From the transverse mixing coefficients for the different sub-reaches estimated with the numerical model, a weighted average transverse mixing coefficient of Dy=0.037 $m^2/s$, i.e., $Dy/(HU^*)$=0.39 , was calculated for the surveyed reach.

The good agreement between the measured data and simulated results using the calibrated model confirms the capability of the stream tube concept and proposed method to be employed in conjugation with measured data for estimating mixing coefficient and capturing the effect of the transverse velocity field, in spite of all implemented simplifying assumptions. The proposed model could also successfully show the distance downstream from the outfall where the tracer reached the opposite bank. Although we used an approximating method in generating the velocity field based on measured data, the proposed method could also capture faster transport of mass in the middle part of the section, where the thalweg

stream line was located. However, further improvements could be expected by using more complex models, especially in predicting the very fast response of the plume to the transverse currents in bends, albeit at the price of higher computational costs.

Higher values for transverse mixing coefficients were found in sub-reaches with a higher shear velocity and sinuosity. The highest transverse mixing coefficient from the numerical model was found at the sharp bend, which confirms the influences of secondary flow and transverse dispersion in the mixing mechanism.

The transverse mixing coefficient was also estimated from standard and general methods of moments for the sub-reaches located in the middle of the plume during the time of the survey. In these sections, tracer data were generated from an analytical solution of the governing equation for the portions of the cross-section where measured tracer data were not available. The average transverse mixing coefficient and cross-sectional velocity profile were compared for two consecutive sections, and it was concluded that the gradient in the cross-sectional velocity profile as a result of local bed features greatly affected the estimated average transverse mixing coefficient.

The average transverse mixing coefficient was also calculated with two empirical prediction methods. The Jeon et al.'s (2007) formula, which considers the sinuosity effect on transverse mixing, showed a better agreement with the empirical model for prediction of the average transverse mixing coefficient in the investigated reach. The method was also successful in finding the sub-reaches with maximum and minimum transverse mixing coefficients.

The proposed numerical modelling approach was generally successful as a practical method for modelling transverse mixing patterns. This success was achieved despite several limiting assumptions in the modelling approach. For example, the model considers neither transverse nor vertical velocities in channel sections, and thus secondary circulation patterns are not considered directly. Furthermore, the transverse mixing coefficient was assumed to be constant across the river in a given section, whereas in

natural channels the transverse mixing coefficient in the shallow parts is expected to be low near the banks. Another approximation in this study was that the bankside boundaries of the grid were smoothed to minimize the numerical instabilities caused by highly angled flow. Irrespective of these limitations, the numerical model provided acceptable results with a low computational cost. This success was achieved in part due to the use of detailed field data for flow velocity and tracer concentration across individual sections, which were used to determine the transverse mixing coefficients for those sections. It has been demonstrated that the proposed novel modelling approach is suitable for the prediction of transverse mixing in highly extended meandering rivers.

**Acknowledgments**

The research performed by A.P. and A.M. was supported by an NPRP Grant 4-935-2-354 from the Qatar National Research Fund (a member of the Qatar Foundation). The authors also wish to acknowledge Curtis Brock and Alberta Environment for supporting this work. The statements made herein are solely the responsibility of the authors.

## Appendix A

River discharge is one of the parameters which affect the mixing rate in meandering rivers (Zhang and Zhu 2011). The Hydat (Water Survey Canada) data for gauge station 05DF001, located approximately 26km upstream of the outfall, shows a river discharge variation of 30% about the mean value of 115 $m^3/s$ during the field campaign (Fig. a.1). In order to consider the effect of variation in river discharge, a 1D shallow water system is solved explicitly using a finite difference scheme over a staggered grid, with second-order accuracy in time and space.

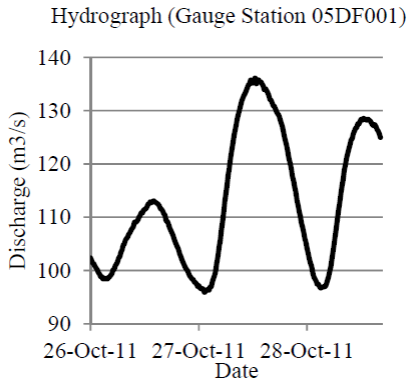


**Figure 4.9 a.1: River discharge data at the Water Survey Canada gauge station (05DF001)**

The 1D shallow water system may be written as:

$$\frac{\partial Q}{\partial t}+\frac{\partial}{\partial x}\left(\frac{Q^2}{A}\right)+gA\frac{\partial h}{\partial x}-gA(S_0-S_f)=0 \qquad \textbf{(4.2.a.1)}$$

$$\frac{\partial A}{\partial t}+\frac{\partial Q}{\partial x}=0 \qquad \textbf{(4.2.a.2)}$$

where $Q$ is river discharge, $t$ is time, $x$ is distance along the river path, $h$ is water level, and $A$ is cross-section area. The parameters $S_0$ and $S_f$ are bed slope and friction slope respectively, and are defined as:

$$S_0=-\frac{dz}{dx} \qquad \textbf{(4.2a.3)}$$

$$S_f=\frac{Q|Q|n^2P^{4/3}}{A^{10/3}} \qquad \textbf{(4.2.a.4)}$$

where $z$ is bed elevation, $n$ is the Manning coefficient, and $P$ is the wetted perimeter. The measured hydrograph (Fig. a.1) was used as the upstream boundary condition to solve Equations (a.1-a.2 ).The river discharge at the time of survey was available for the surveyed sections from Chapter three. The Manning coefficient and bed slope were adjusted using measured values to calibrate the model. A comparison of the modeled and measured values for discharge is provided in Fig. (a.2)

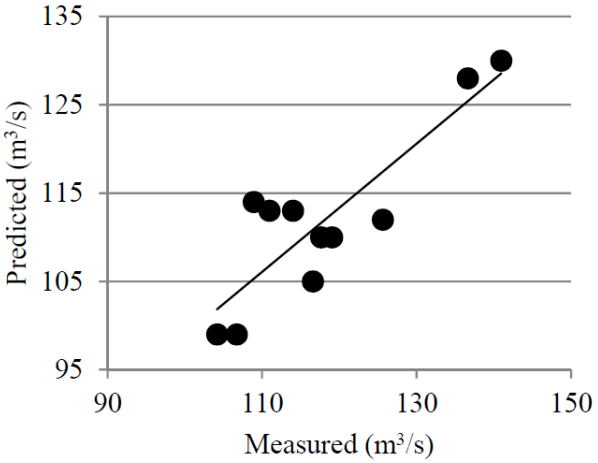


**Figure 4.10 a.2: Comparison of the modeled and measured value for discharge**

For solving the 1D shallow water system, a time-varying discharge was obtained at each river section. This modeled initial unsteady discharge at each section was calibrated with the available measured discharge data. Measured discharge was available for individual sections at a single discrete time step. The ratios of modeled to measured discharge were calculated and were used to estimate a calibration ratio throughout the model domain. The ratio field was applied to all time steps to obtain the unsteady velocity field throughout the domain.

## Appendix B

As mentioned in Section 3.2.2, this study employs the finite volume method and solves the advection part using an explicit third-order upwind scheme.

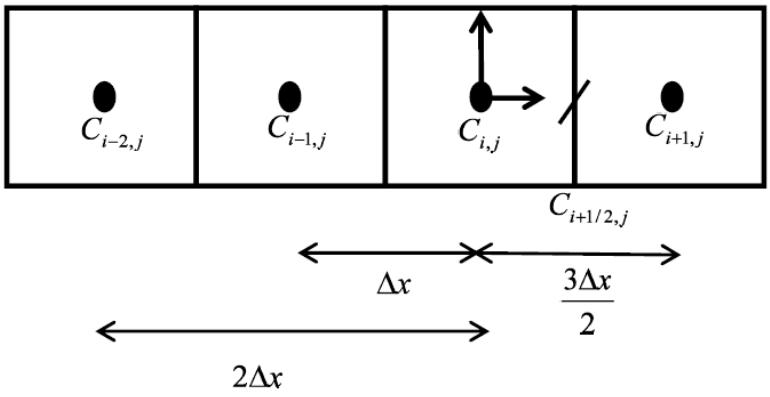


**Figure 4.11 b.1: The involved cells in the third-order upwind scheme**

The finite volume method uses advection flux at cell boundaries ( $F_{i-1/2,j}$ and $F_{i-1/2,j}$ ) for calculating the concentration at the center of a cell ($C_{i,j}$). In order to calculate the advection flux at each cell boundary, the concentration at the cell boundary is required ($C_{i+1/2,j}$). Following Mohammadian and Le Roux (2008), an explicit third-order upwind scheme is used for calculating $C_{i+1/2,j}$. This method uses four neighbor cells (Fig. a.1) and estimates the value at the boundary by third-order polynomial approximation.

$$C = ax^3 + bx^2 + cx + d \qquad \textbf{(4.2.b.1)}$$

Substituting the *x* and *C* values in four neighbor cells, one gets the following system of equations:

$$d = C_{i,j} \qquad \textbf{(4.2.b.2)}$$

$$a\left(\frac{3\Delta x}{2}\right)^3 + b\left(\frac{3\Delta x}{2}\right)^2 + c\left(\frac{3\Delta x}{2}\right) + d = C_{i+1,j} \qquad \textbf{(4.2.b.3)}$$

$$a(-\Delta x)^3 + b(-\Delta x)^2 + c(-\Delta x) + d = C_{i-1,j} \qquad \textbf{(4.2.b.4)}$$

$$a(-2\Delta x)^3 + b(-2\Delta x)^2 + c(-2\Delta x) + d = C_{i-2,j} \qquad \textbf{(4.2.b.5)}$$

Solving the system of equations, the polynomial coefficients *a*, *b*, *c*, and *d* in (a.1) can be obtained, and then the concentration at the interface ($C_{i+1/2,j}$) can be calculated using these values as:

$$C_{i+1/2,j} = a\left(\frac{\Delta x}{2}\right)^3 + b\left(\frac{\Delta x}{2}\right)^2 + c\left(\frac{\Delta x}{2}\right) + d \qquad \textbf{(4.2.b.6)}$$

# Chapter 5:

**Mixing of the Ras-Laffan desalination plant discharge; Part I. methodology and preliminary results**

**Considered to be submitted to the Journal of Environmental Fluid Mechanics**

**Authors**: Abolghasem Pilechi, Majid Mohammadian, Colin D. Rennie, Hazim Qiblawey, Gregory Lawrence, Mohammad Albeldawi, Ramadorai Kadambi

## 5.1 Abstract

An intensive field survey was conducted in the near and far fields of the Ras Laffan Industrial City (RLIC) surface outfall in Qatar, measuring temperature and flow velocities.

The observed behavior of the plume was in good agreement with various empirical formulas for surface outfalls. Spatial characteristics of the plume were studied, including the detachment point from the bed and the spatial extent of different zones of the plume including the zone of flow establishment. Longitudinal variations of the plume dilution, thickness, maximum temperature, and velocity were examined. Using the field-measured data, an entrainment coefficient of 0.67 for the jet mixing and 0.78 for the plume spreading rate were estimated.

The effects of the aspect ratio of the outfall and the shallow discharge condition on the dilution rate were also investigated. The shallow ambient water body condition was observed to reduce the average dilution of the plume. The length of the zone of flow establishment was also found to be larger under the effect of the large aspect ratio of the outfall.

A novel remote sensing technique is also introduced for the study of the near-field mixing of thermal surface plumes. Thermal infrared satellite images were calibrated using surface water temperature data

measured with the CTD probe, and the calibrated satellite images show that the proposed method can be used to investigate the dynamics of thermal plumes.

## 5.2 Introduction

Surface outfalls are among the most common outfall systems due to their simplicity, low construction cost, and high discharge capacity. Surface outfalls have been used historically in industrial compounds, especially for cooling effluents. The effluent outflows generally have a different velocity and density than the receiving water. Effluents are generally called buoyant jets (also known as forced plumes) in the literature if they are influenced by both momentum and buoyancy effects (Jirka et al. 1996). Buoyant river discharges into seas and oceans are also analogous to surface jets. Due to the popularity of surface outfalls, extensive research has been conducted in the last few decades on their mixing patterns. Some studies were more focused on investigating the parameters which influence the mixing patterns (Luketina and Imberger 1987, Whitney and Garvine 2005, Hetland and MacDonald 2008, Jones et al. 2007, Abessi et al. 2012, Nekouee et al. 2013), while others were more focused on developing empirical equations for predicting mixing rates (Lal and Rajaratnam 1977, Rajaratnam and Humphries 1984, Akar and Jirka 1995). Developing and applying numerical methods in order to model the mixing process was the subject of yet another group of mixing studies (Yankovsky and Chapman 1997, Kim and Cho 2007).

Surface jet flows can be divided into three principle regions, which are: (i) the Zone of Flow Establishment (ZFE), also referred to as the potential core; (ii) the near field; and (iii) the far field (Lin et al., 1977). The ZFE is the closest region to the outfall, and the effluent has uniform velocity and temperature profiles at the discharge location. The velocity difference between the jet ZFE and the ambient water produces shear, and consequently turbulence around the jet. The ambient water entrains the ZFE and decreases the width of this region as distance increases from the outfall. The ZFE is defined as being from the outfall location to the point that the jet centerline velocity or temperature starts to decay from the discharge value.

The next region is the near field, also known as the Zone of Established Flow (ZEF), in which the mixing is affected by the initial volume, momentum and buoyancy fluxes. Velocity, salinity, and temperature all have self-similar Gaussian shape profiles in this region. In some studies, the extent of the near-field region is defined as the point where the jet center-line velocity excess (from the ambient flow) is dissipated, but the density still differs from the ambient environment in the plume region (Lin et al., 1977). The momentum difference between the jet region and the ambient water in the near field generates shear, and consequently turbulence, which is the main mixing mechanism within the initial portion of the near field. The buoyancy-derived forces as a result of the density gradient also enhance the mixing process. The buoyant mixing mechanism is more significant when farther from the high-momentum region in the vicinity of the outfall.

Two transition zones can be defined in surface buoyant jets (Jirka, 2007). The first transition occurs within the zone of flow establishment, where the relative uniform velocity distribution is transformed into a sheared jet-like Gaussian-shaped profile. The entrainment mechanism within this region is due to the stream-wise or azimuthal shear (Jirka, 2004). As the jet gets farther from the source, it is weakened due to the momentum diffusion (Jirka et al., 1981), and the second transition zone begins. This is the region in which jet-like behavior transitions to plume-like behavior, and vertical entrainment is inhibited and buoyancy-spreading dominates the mixing process. In short, the jet-like behavior transitions to plume-like behavior. This will result in a sharp-edged vertical profile with a uniform shape in the lateral direction (Jirka, 2007).

The near-field outfall behavior can be addressed by the discharge properties, such as the discharge velocity $U_0$, discharge channel width $b_0$, depth $h_0$, channel cross-sectional area $a_0=b_0h_0$, discharge density $\rho_0$, and discharge angle relative to the channel direction $\sigma_0$. In a general designation (Jirka 2007), these parameters are defined as the initial volume flux ($Q_0=U_0a_0$), momentum flux ($M_0=U_0^2a_0$), and buoyancy flux ($J_0=U_0g_0'a_0$). The initial buoyancy acceleration $g_0'=(\Delta\rho_0/\rho_a)g$ is calculated from the initial density difference $\Delta\rho_0=\rho_a-\rho_0$, where $\rho_0$ is the discharge density, $\rho_a$ is the average ambient density, and $g$ is

gravity. Ambient water velocity $u_a$, depth $H$, and distance along the jet trajectory are other ambient water parameters that affect the near-field flow regime and the mixing pattern.

In surface wall-jet discharges in shallow water (the case investigated in this study), jet entrainment is restricted by the presence of a solid side wall and bed. The jet is initially attached to the bed in the region close to the outfall. This is the region where the inertial forces dominate, and is referred to as the turbulent core (Safaei, 1979). Linear spreading is observed within this region as a result of momentum exchange between the jet and the ambient water. This mechanism is also known as jet mixing. Flowing over a mild-slope bed, the jet reaches the maximum depth ($h_{max}$) and then detaches from the bed (Fig. 5.1). From this point, turbulence and entrainment lessen greatly; buoyancy spreading controls the mixing after this point, and the plume thickness starts to reduce to the point of uniform transverse distribution.

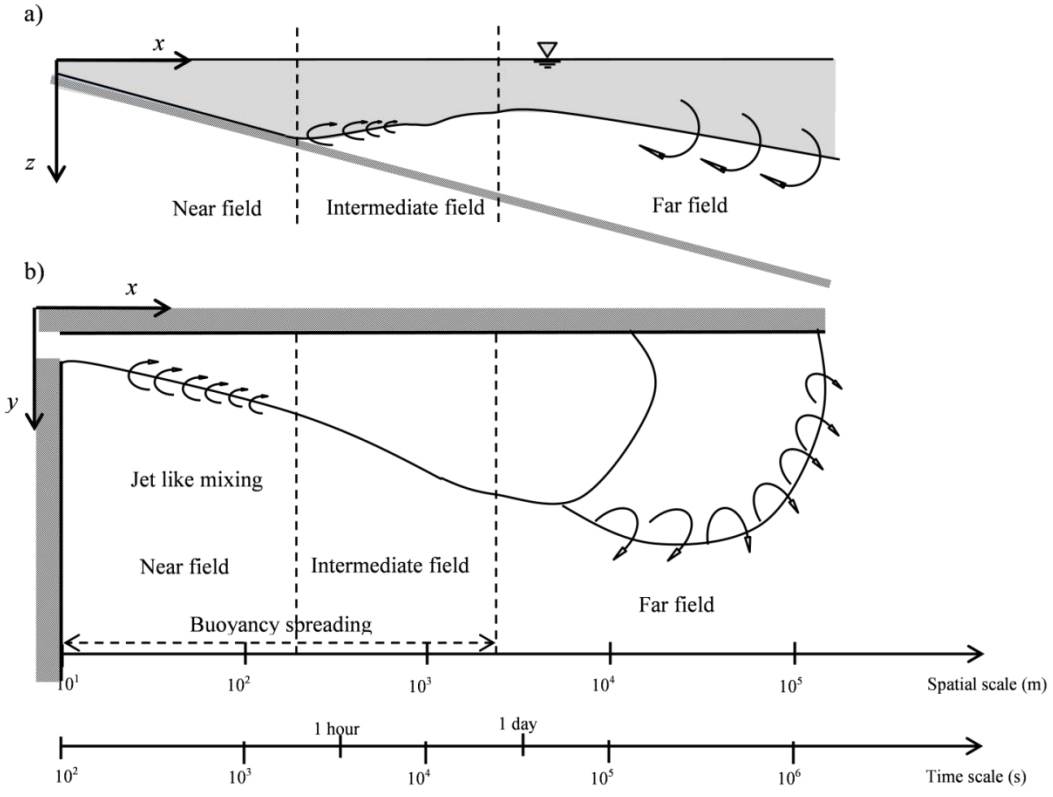


**Figure 5.1: A schematic view of the vertical-mixing processes in the present project: a) profile view; b) plan view.**

Recent advancement in remote sensing technology has greatly enhanced the popularity of employing remote sensing approaches in mixing studies, especially in regions where conducting a field survey is not convenient due to access difficulties. The idea of using remote sensing to monitor ocean outfalls dates back to the 1980s (Davis et al. 1985). These approaches are based on using remote sensors to measure the volume reflectance. The remittance may be in the visible, near-infrared, or thermal infrared wavelengths. As remote sensing sensors only measure the reflectance, they are normally used in addition to field measurements for calibration purposes. The remote sensing methods vary with respect to the sensors utilized. Thermal imaging cameras (Ali et al. 2011), ocean surface current radar (OSCR) (Chin et al. 1997), and airborne photography (da Silva et al. 2001) are some examples of using different remote sensing methods to identify the fate of discharges in rivers, coastal waters, or oceans. Due to their high spatial resolution and coverage as well as free availability of data, thermal infrared (TIR) photos have been used in previous various water surface temperature studies (Kishino et al. 2000, Donlon et al. 2002, Kumar et al. 2003, Kay et al. 2005; Becker and Daw 2005, Lamaro et al. 2012). Davies et al. (1997) used thermal infrared (TIR) imagery to map the cooling-water discharge from a power plant. In one of the most recent studies, de Boer et al. (2009) used the Sea Surface Temperature (SST) images with resolution of 1km to study the far field dynamics of the Rhine River plume. None of the mentioned studies have used high resolution satellite imageries for investigating the plume dynamics in the near-field region. In this study, remote-sensing data is used to study the *near-field* mixing process of buoyant plumes of the Ras Laffan Industrial City (RLIC) outfall in Qatar.

Relatively few field investigations have been conducted on coastal plumes compared to mathematical and experimental studies due to the complexity and large scale of the mixing process as well as the high cost of the field measurement. Most studies have been conducted in specific regions of the plume. Some of them were more focused on the near-field mixing characteristics such as Luketina and Imberger (1987), Chen et al. (2009) and MacDonald et al. (2013), while others investigated the far-field fate of the plume as a result of large-scale mixing processes (e.g., Chant et al., 2008; Horner-Devine et al. 2009).

Laval et al. (2012) used a combination of field measured (temperature and salinity) and remote sensing obtained (surface skin temperature) data in the Quesnel Lake, British Columbia, Canada to investigate the physical processes that control the seasonal mass transport in fjord-lakes. The employed MODIS Thermal Infra Red (TIR) satellite imagery in their study provided data with high temporal resolution of 5 hours. However, the corresponding large pixel size of 1km makes it incapable to capture the small scale processes in near-field mixing studies.

Nekouee (2010) investigated the dynamics of the Grand River plume in the Lake Michigan using remote sensing and field measurement approaches under different environmental forcing mechanisms. The study was more focused on the mid and far field of the plume with larger spatio-temporal scale. In one the most comprehensive studies, Roberts et al. (2011) conducted a field study on the near-field and far-field of the plume from the Boston multi-port diffuser outfall. They measured tracer concentration, salinity and temperature as well as the hydrodynamic data during their field campaign. The near-field measured data was compared with experimental results for plume dynamics close to the outfall. Wang et al (2014) used acoustic Doppler current profiler (aDcp) measured data to investigate the effect of different forcing mechanisms in the near-field turbulent kinetic energy (TKE) production of the Merrimack river plume.

In the current study, the near and far fields of the RLIC effluent plume were surveyed in the field using an aDcp and a Conductivity-Temperature-Depth (CTD) probe. The collected data from the field campaigns as well as measured data from three environmental buoys outside the port were used in calibrating LandSat7 thermal infrared images of the jet plume. The novel aspect of this study is in combining a remote-sensing approach and a field measurement technique to study the near-field mixing process. The real-time measurements used in this study allowed for on-the-fly optimization of the survey path to best characterize the effluent plume. The current study is also distinctive for the size of the outfall investigated. The investigated outfall in this study has an aspect ratio (the ratio of width to depth) of about

400, which makes it a unique geophysical case (Hetland 2010) compared to similar previous studies such as Nekouee et al. (2013) (A=16) and Pritchard and Huntley (2002, 2006) (A=40).

This paper is organized as follows. In the next Section, the employed methodology in this study is discussed in detail. Section 5.3 presents the observed data from the field measurement and remote sensing approach. Different characteristics of the observed plumes are discussed in Section 5.4. The conclusion of the study completes the work in Section 5.5.

## 5.3 Methodology

This section presents the methodology employed in the data collection using direct field measurements and remote sensing.

### 5.3.1 Field survey

RLIC has a surface outfall located at 25° 53.480' North (latitude) and 51° 34.483' East (longitude), discharging into the sea at about 222 $m^3/s$ (Fig. 5.2). Intensive field surveys were conducted at the RLIC outfall on March 19 and 24 and May 15, 17, 18, and 19, 2014. The near-field and far-field temperatures of the RLIC effluent plume were surveyed from a boat moving both across and along the plume using a CTD probe. The hydrodynamics parameters (water velocity and depth) of the near-field of the plume were also measured simultaneously using an aDcp on May 18 in ten sections across the outfall. The distance between the surveyed sections ranged from 10 m at the outfall to 100 m in the last surveyed section about 1km downstream the outfall. It should be noted that the aDcp measurements were conducted for the entire surveyed path with the CTD on the other days. However, due to the weakness of the ambient tidal currents in the basin and low accuracy of the measured velocity for the current velocities lower than 0.1m/s, the collected data from other regions of the outfall were not used in this study.

The CTD used in the present study was a Seabird SBE19-Plus Conductivity-Temperature-Depth (CTD) probe. This CTD can detect temperatures ranging from -5℃ to 40℃ with a resolution of

0.005°C. The temperature data were recorded with a sampling frequency of 4Hz. The CTD data were collected from the moving boat at approximately one meter depth from the water surface. Stationary vertical temperature profiles were also collected with the CTD at the middle of each surveyed section.

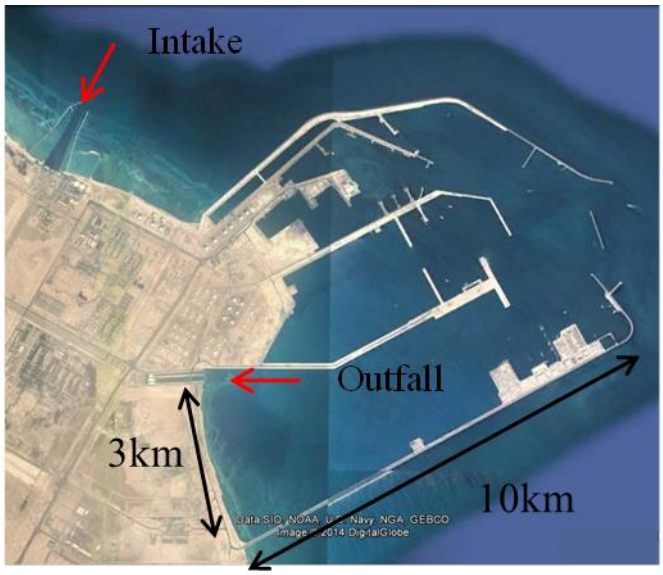


**Figure 5.2:Ras Laffan Industrial City Port. Adapted photo from Google Earth**

The outfall hydrodynamics were measured using a Teledyne RiverRay acoustic aDcp. The aDcp measured the depths and vertical profiles of three-dimensional water velocity at a 1Hz sampling frequency, using bottom-tracking for the boat velocity reference. The CTD and aDcp data were collected simultaneously and synchronized by means of Global Positioning System (GPS) position and time-stamp data that were integrated into the data streams collected by the CTD and the aDcp. An S320 Real-Time Kinematic Global Differential Positioning System (GPS) manufactured by Hemisphere was used on the boat to locate the measurement locations. Position data were collected at 10Hz. The measurements were conducted continuously while moving away from the outfall in a zig-zag pattern.

### 5.3.2 Remote sensing

The thermal infrared (TIR) band (Band 6) Land Sat7 photos from the USGS were used in the remote-sensing approach for this study. LandSat7 images have eight spectral bands. The wavelength of Band 6 is 10.40-12.50 micrometers and is available in 30-meter resolution for products processed after 2010. TIR images are available in low-gain band (B6L) and high-gain band (B6H). Following Chande et al. (2009) and Lamaro et al. (2012), the low-gain band was used in this study due to its greater range and lower saturation. Water surface temperature "at-satellite" values can be estimated from TIR images using the relationships available in the LandSat7 handbook; however, those values may differ from actual water surface temperatures depending on the effective climatic parameters such as cloud coverage, humidity, etc. The water surface temperature can be calculated using different methods such as the Single Channel Generalized Method (SCGM; Jiménez-Muñoz and Sobrino, 2003) or Radiative Transfer Method (RTM) (Srivastava et al. 2009). Lamaro et al. (2012) compared these two methods and found the SCGM method better than the RTM with respect to estimating rather small temperature differences.

In the present research, TIR images were converted to surface temperature by developing a calibration curve with available ground-truth data. The LandSat photos are taken every 8 days at 10:00 AM local time in the RLIC outfall region. Of the many archived TIR photos between 2013 and 2014, only the photos with zero cloud cover were used for the calibration. Due to the concurrency of one of the field survey dates (May 15) to the satellite photographs, the measured CTD temperature data in the near field of the outfall on May 15 were used for calibrating the satellite images. More temperature data were also available from three surface environmental buoys outside the port (Fig. 5.3), and were employed to calibrate other available 2013-14 TIR images.

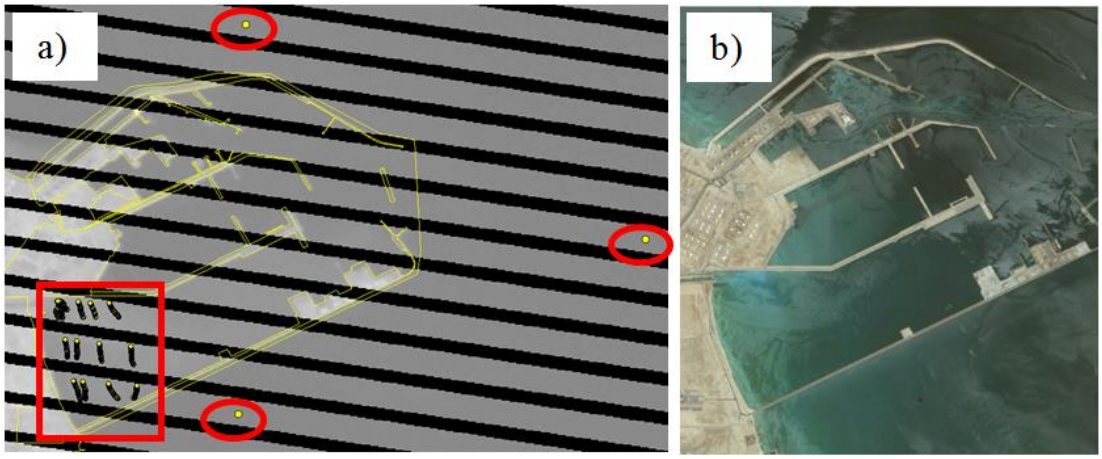


**Figure 5.3: a) Raw LandSat7 imagery and; b) Google Earth photo. The red ellipses show the location of the environmental buoys mounted outside the port. The discrete points in the red rectangle represent the measured data from the May 15 survey**

The pixel value of the measured points from May 15 as well as the environmental buoys were extracted from the geo-referenced LandSat7 TIR photos for May15 and all LandSat7 satellite photos with zero cloud coverage from 2013 until May 2014. The pixel values were then plotted against the measured temperature at the corresponding location (Fig. 5.4).

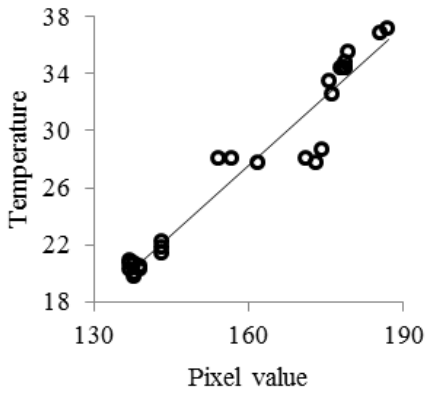


**Figure 5.4: Calibration Curve (The calibration curve has been prepared using water surface temperature measured with the CTD during the May 15 survey, as well as temperature data collected at environmental buoys during 2013-2014 dates with available LandSat7 photos**

## 5.4 Results

In this section, the data collected from direct field measurements as well as the sample data from the introduced remote sensing approach are presented.

### 5.4.1 Data from direct field measurements

The entire area surveyed in May 2014 is shown in Fig. 5.5a. Integrating the GPS position data with the CTD data in real time allowed for measurement of the spatial distribution of temperature, which consequently helps in investigating the near-field mixing process of the outfall.

The field-measured data, including salinity and temperature coordinates of the measured points, were imported into GIS and superimposed on the geo-referenced Google Earth images. The imported data were interpolated using the kriging method, and the spatial distribution of the effluent jet-plume temperature was obtained for each survey date (Fig. 5.6), which will be discussed in Section 5.4. The six hour averaged wind speed and direction before the time of data collection are also presented as a scaled vector for each survey date in Fig. (5.6). Moreover, the vertical profiles of temperature at multiple points in the center of the plume throughout the depth were collected, and will also be discussed in Section 5.4. Figure 5.5a shows the survey path. The locations of the stationary measurements for vertical temperature profiles are also presented in Fig. 5.5b. Such data can significantly help in understanding mixing processes and evaluating the accuracy of prediction methods, which are mostly based on laboratory studies.

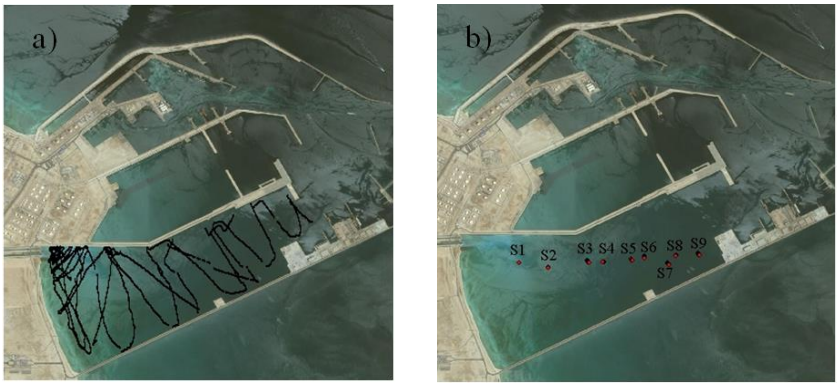


**Figure 5.5: a) The survey path; and b) the location of the stationary measurements for vertical temperature profiles**

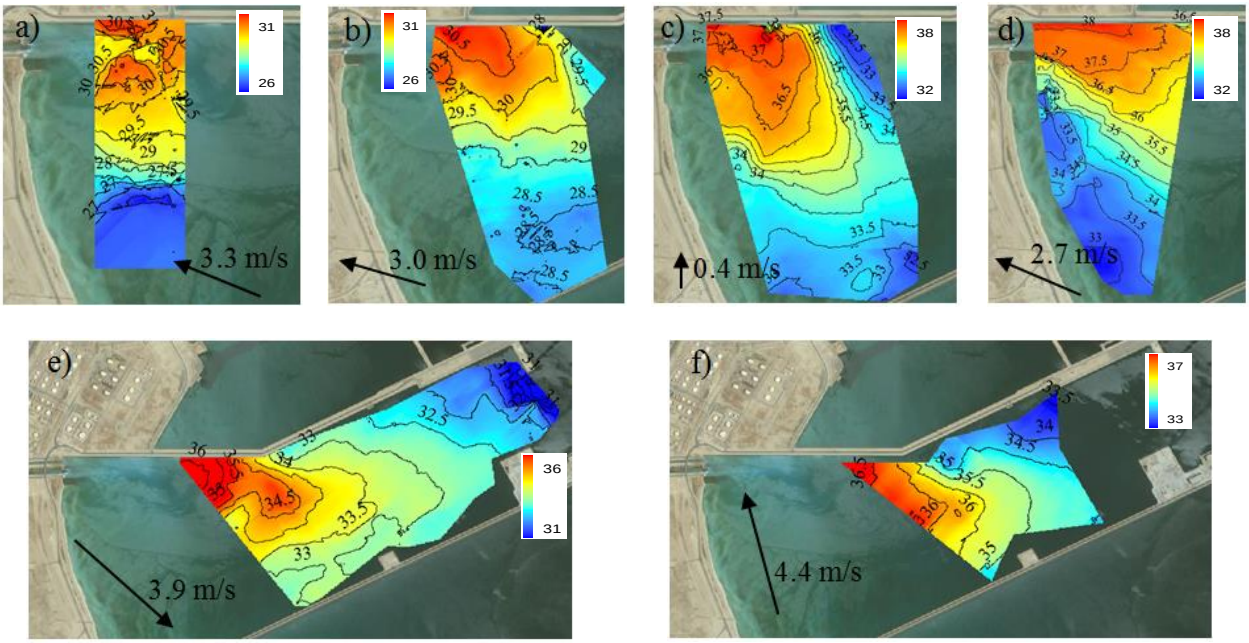


**Figure 5.6: Measured temperature fields from CTD. a)March 19,2014; b)March 24, 2014; c)May 15, 2014; d)May 18, 2014; e)May 17, 2014; f)May 19, 2014. The six hour averaged wind speed and direction before the time of data collection are presented as a scaled vector**

### 5.4.2 Data obtained from the remote sensing approach

Using the linear equation denoted in the remote-sensing section, the TIR LandSat7 photo was converted to a thermal image. Figure (5.7) presents two samples of the thermal photos obtained from the remote-sensing approach discussed in Section 5.2.2, based on two days for which LandSat images with zero

cloud coverage were available. The May 15 case (Fig. 5.6.a) coincided with a field survey date, and the plume presented in Fig. (5.6.a) is in general agreement with the field-measured data presented in Fig. (5.5.c). Figure (5.7.b) presents the results of the calibrated LandSat7 images from April 14, 2013.

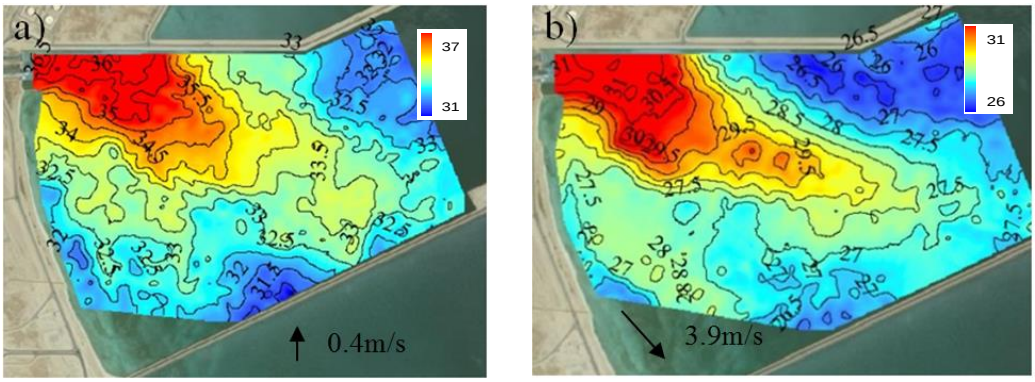


**Figure 5.7: Calibrated LandSat7 photos for: a) May 15, 2014; and b) April 14, 2013**

As can be observed, there is the same dispersion pattern on May 15, which is a proof of the concept that remote-sensing data can be used to study the longitudinal and transverse mixing and dilution of thermal plumes in the near field. Using the remote sensing approach has made it possible to have the entire shape of the plume (near-field and far-field) at the same time. This is very helpful, especially for coastal plumes for which large extent precludes field measurement in the near-field and far-field of the plume in the same tidal phase. In this study the plume has detached from the side jetty by the end of its near-field and inclined towards the southern jetty. The ZFE with a uniform "top hat" shaped lateral distribution of the temperature can also be seen close to the outfall. A transition region to ZEF with high lateral spreading of the plume is observed farther downstream. The compact contour lines of the temperature at the outfall have become wider as the plume flowed and mixed with the ambient water. The effect of wind action on the plume trajectory is also observed by the end of the ZFE. Further analysis of the remote sensing results is beyond the scope of this paper. A subsequent paper will use the remote-sensing data to evaluate the impact of tidal currents and wind on plume dispersion dynamics.

## 5.5 Plume characteristics

The longitudinal and transverse mixing and dilution of the plume as it flows into the ambient environment is clearly observed in Figs. 5.6 and 5.7. Variations of maximum temperature and velocity along the jet are consistent with theoretical predictions, as will be explained in this section. Also in this section, some specific characteristics related to longitudinal variations of the plume will be discussed, including entrainment characteristics, detachment point, spatial extent of different zones of the plume (e.g., length of the zone of flow establishment and near field), and plume thickness, as well as variations of the maximum temperature and velocity along the jet plume.

### 5.5.1 Entrainment

If the initial momentum of the outfall is significant, the near-field mixing process can be categorized as jet-like mixing, and if the outfall is buoyant, the regime may change to plume-like mixing further downstream. Two main flow regimes are therefore expected to be observed in the case of high-momentum buoyant jets. The first regime includes horizontal and vertical jet-like mixing, which results in growth of the jet (in all directions) in the near-field. Due to the large aspect ratio of the outfall, dilution is controlled by the vertical mixing in the geophysical scale cases (Hetland 2010, Horner-Devine et al. 2015). The second regime includes a decrease in plume thickness as a result of buoyancy-induced spreading (Luketina and Imberger 1987). In positively buoyant cases, a detachment point is observed beyond which the buoyant spreading dominates and the turbulence intensity is greatly reduced.

In the current study, using the entrainment coefficient concept and the field-measured data, the mixing mechanisms were investigated separately. The jet mixing mainly occurs due to the high momentum exchange between the jet and the ambient water close to the outfall. The ambient water entrains in the jet due to the momentum difference between the inside and outside of the jet, and increases the jet flow. The high jet momentum declines with distance from the outfall, and the jet flow discharge approaches its

asymptotic value. Along the jet trajectory, the ratio of the jet flow, including entrained ambient water ($Q$) to the initial jet flow ($Q_0$), is defined as the volumetric/mean dilution ($S_{mean}$), i.e.,

$$S_{mean} = \frac{Q}{Q_0} \tag{5.1}$$

The dilution at the point where the jet flow discharge does not further change downstream has been referred to as "stable dilution" by Kaufman and Adams (1981), and the jet adopts a plume-like behavior after reaching this point of asymptotic discharge.

In this study, the jet flow was calculated from the aDcp-measured data. Figure 5.8 shows that the initial jet discharge (222 $m^3/s$) increased to 408 $m^3/s$ by 500 m from the outfall, which implies a bulk entrainment ratio of 1.8. The discharge remained constant after this point, and buoyant spreading dominated the mixing process. Therefore, the transition from jet-like to plume-like behavior can be considered to have occurred between 400 and 500 m from the outfall. Based on Stolzenbach and Harleman's (1971) model, Kaufman and Adams (1981) estimated the transition distance ($x_t$) from the jet-like to the plume-like behavior as:

$$x_t = 12 L_0 U_0 / \left(g'_0\right)^{1/2} \left(h_0 b_0 / 2\right)^{1/4} \left(h_0 / b_0\right)^{-1/5} \tag{5.2}$$

From the measured data, using $U_0$=0.5 m/s, $b_0$=500 m, and $g_0'$=0.026 $m/s^2$, $x_t$=550m was calculated from Eq. (5.2) in the current study. The calculated transition distance ($x_t$) is for a densimetric Froude number ($F_0 = U_0/(g_0' L_Q)^{1/2}$) of around 3 (Fig. 9), where $L_Q=(h_0 b_0)^{1/2}$ is the discharge length scale. This is in agreement with Chu and Jirka (1986), who reported $F_0$=3 as the transition limit from jet-like ($F_0$>3) to plume-like ($F_0$<=3) behavior.

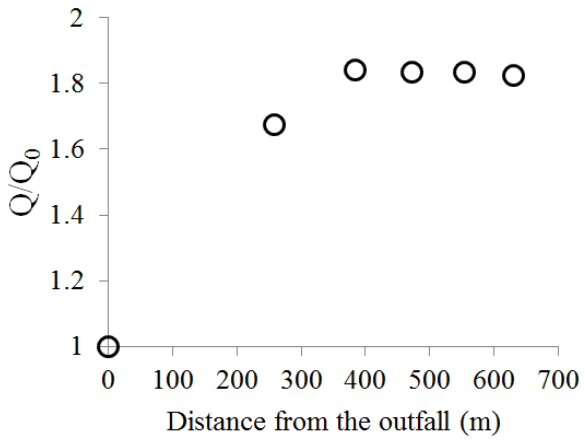


**Figure 5.8: Variation of the jet flow with distance from the outfall**

The graph presented in Fig. (5.8) has a shape similar to the results reported in Vanvari and Chu's (1974) experimental study. The average dilution can also be obtained from empirical formulas. Some of the available relationships for estimating the average dilution in ZFE are presented in Table (5.1). The formula proposed by Stefan et al. (1975) estimates $S_{mean}$=3.7 between the outfall and the transition region, which is around two times greater than the estimated value from Fig.5.7. The formula proposed by Stefan et al. (1975) is based on their experimental results (engineering scale, Hetland 2010) on the dilution of a heated surface jet for $F_0$=3.5 and an outfall aspect ratio of 10 for unconfined outfalls and deep ambient water conditions. However, in this study, the outfall was located in shallow water and was confined on one side. The equation by Rajaratnam (1965) also overestimates the stable dilution ($S_{mean}$=14). The lower observed average dilution in the present study as compared to Stefan et al. (1975) and Rajaratnam (1965) can be attributed to the confinement effects, which did not allow ambient water entrainment from the bottom and left side of the jet. The restrictive effect of the shallow ambient condition on the dilution rate has been previously reported in different studies (e.g., Sobey et al. 1988, Chen et al. 1999, Shinneeb et al. 2011). Johnston and Volker (1993) also reported that the vertical position of the jet in a shallow environment can reduce the centerline dilution of the jet by up to 50%. Giger et al. (1991) proposed Eq. (3) for predicting the ultimate volume flux of non-buoyant jets in shallow water, as follows:

$$\frac{Q}{Q_0} = 1.1e^{-0.5} I_1 \left( \frac{C_b}{I_2} \frac{H}{W} \frac{8}{f} \right)^{1/2} \quad \textbf{(5.3)}$$

In Eq. (3), $I_1 = \int f(\eta) d\eta$, $I_2 = \int f^2(\eta) d\eta$ and $f(\eta)=U/U_m$ is the distribution function of the $U$-velocity, $C_b$ is the geometrical spreading factor calculated as 0.78 from the measured data in the following, and $f$ is the friction factor. Using $I_1$=1.4 and $I_2$=0.9 from the measured data and assuming $f$=0.01 for the friction factor, $Q$=336 m$^3$/s was estimated for the ultimate volume flux, implying a bulk entrainment coefficient of 1.5, which is comparable with the value 1.8 obtained in this study, as mentioned above. The estimated value from Eq. (5.3) confirms the restrictive effect of the confinement on the mixing potential of the outfall as also mentioned in Hetland (2010) and Horner-Devine et al. (2015).

**Table 5.1:Empirical formulas for estimating the average dilution in ZFE**

| Reference | Empirical relationship | Estimated $S_{mean}$ |
|---|---|---|
| Stefan et al. (1975) | $\frac{Q}{Q_0} = 1 + \left[ 0.087 \left( \frac{x}{2h_0} \right)^{\frac{2.35+0.75A}{0.9+A}} \right] \left[ 1 - \frac{0.52}{F_0^{0.41}} \right]$ | 3.7 |
| Rajaratnam (1965) | $\frac{Q}{Q_0} = 1 + 0.04 \frac{x}{h_0} + 0.0046 \left( \frac{x}{h_0} \right)^{0.8}$ | 14 |

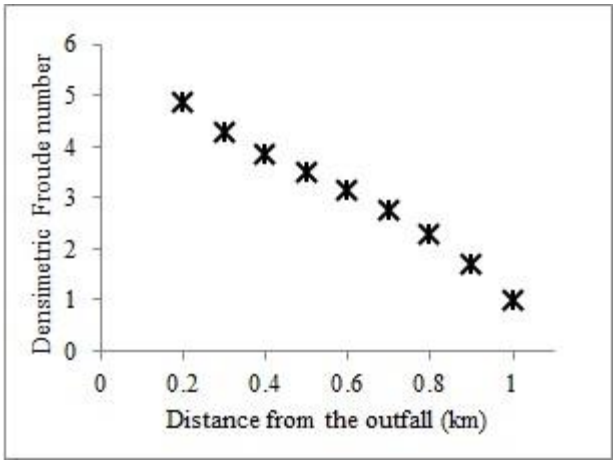


**Figure 5.9:Variation in densimetric Froude number with distance from the outfall**

As the discharge has a higher temperature ($T_0$) than the ambient water ($T_a$), it is expected that farther from the outfall, buoyancy effects will force the effluent to detach from the bed, and buoyancy-induced mixing will widen the plume and decrease the plume thickness (Luketina and Imberger 1987). The plume spreads laterally within this region due to the difference in density with the ambient water.

Figure (5.10) shows lateral plume-spreading in the near field for May 15 and May 18. The linear growth in the plume width is consistent with other studies (e.g., Giger et al. 1991), and implies a plume width expansion rate (also referred to as entrainment rate) of 0.78 for the buoyancy-mixing mechanism. The vertical density gradient can reduce vertical mixing, resulting in enhanced horizontal mixing. The enhancement in horizontal spreading in response to buoyancy forces and vertical confinement in shallow water has been reported by Chen and Jirka (1999) and Sobey et al. (1988). This has resulted in a relatively high rate of plume width expansion compared to the values reported in Giger et al.'s (1991) and Darcos et al.'s (1992) experimental studies (0.106 to 0.96).

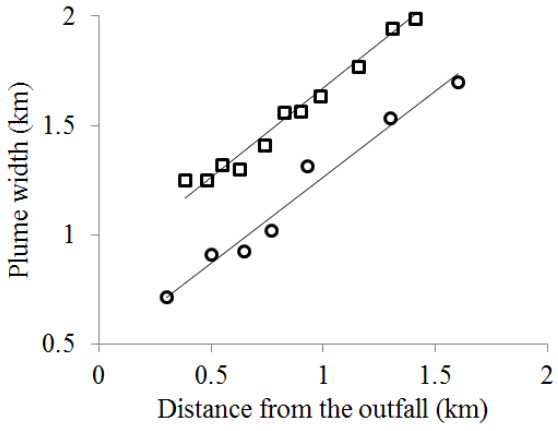


**Figure 5.10: Variation of the plume width with distance from the outfall for May 15 (square) and May 18 (circle)**

### 5.5.2 Spatial extent of different zones of the plume

The zone of flow establishment is the closest region to the outfall with a uniform velocity distribution across the jet. The minimum dilution is close to 1 in this region, as the maximum velocity and

concentration are nearly constant. The length of the ZFE is an important parameter, as the velocity distribution gets self-similar and follows a Gaussian shape at the end of this zone. The length of the ZFE is affected by various parameters such as the discharge densimetric Froude number ($F_0$) and outfall aspect ratio (Shirazi and Davis 1976). The length of the ZFE is shorter in shallow water due to the friction effect from the bed (Johnson and Volker 1993).

In this study, variation of the maximum velocity along the jet axis ($U_m$) was obtained from the aDcp-measured data (Fig. 5.11), and the length of the ZFE can be inferred to be approximately 400 m. Variation of the velocity along the jet axis will be discussed in detail in Section 5.4.5.

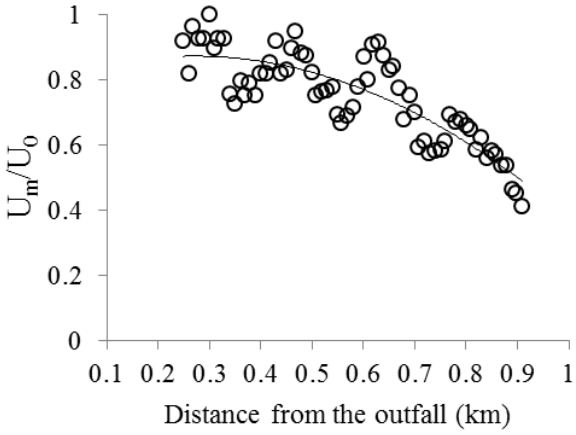


**Figure 5.11: Variation of velocity along the jet axis. (The discrete points shown by the cross symbols in Fig. (10) are extrapolated, as the aDcp-measured velocities were not found to be accurate for values less than 0.1 m/s.)**

The extent of the ZFE has been reported in different studies as being from 10 to 15 times the outlet length scale downstream of the source (Chen and Nikipolous, 1979; Schlichting and Gertsen, 2000). Various formulas have been proposed for estimating the length of the ZFE, and in this study, the length of the ZFE has been estimated from various semi-empirical equations in Table 5.2. As previously mentioned, due to the difference in buoyancy with the ambient water, the outfall is categorized in this study as a buoyant surface jet. Therefore, the densimentric Froude number is also expected to be effective over the extent of the ZFE. From the various formulas presented in Table 5.2, the formulas proposed by

Shirazi and Davis (1976) and Jirka (2004) estimated more reasonable values compared to the observed value for the length of the ZFE. It should be noted that some of the formulas in Table 2 are based on certain assumptions/conditions with respect to the outfall shape, the aspect ratio and discharge depth that do not necessarily apply to the present case. The better performance of Shirazi and Davis' formula can be explained by considering the aspect ratio effect of the outfall and the fact that it was developed for a rectangular surface outfall. Deo and Nathan (2007) reported an asymptotic-like increase in the length of the ZFE with an increase in the outfall aspect ratio.

**Table 5.2: Length of the Zone of Flow Establishment**

| Shirazi and Davis (1972) | Jirka (2004) | Rajaratnam (1976) | Motz and Benedio (1971) | Pyrch (1972) | Observed value (m) |
|---|---|---|---|---|---|
| $5.4b_0\left[\left(\frac{b_0}{h_0}\right)F_0'\right]^{\frac{1}{3}}$ | $8.0L_Q e^{\frac{-5}{F_0^2}}$ | $7L_Q$ | $2.2Ah_0$ | $4D_0$ | - |
| 455 | 200 | 178 | 1540 | 100 | 400 |

$D_0$: the equivalent diameter of a semicircular outlet channel

### 5.5.3 Plume Thickness

In this study, the very high discharge value and shallow depth at the outfall generated a wall-jet flow regime at the outfall, which is discharged into a nearly stagnant ambient water body. In contrast to buoyancy-induced forces, which tend to detach the jet from the bottom, high momentum close to the outfall enhances vertical mixing and thickens the plume in the near-field of the jet (Horner-Devine et al., 2015).

Figure 5.12 presents the vertical profile of the temperature at stationary measurement points along the plume axis (Fig. 5.6b). As is seen in Table 5.2, the vertical profiles were not all measured in the same date. Figures 5.12.a and 5.12.b are from the near-field survey on May 15, Fig. 5.12 (c, e, g, and i) presents the collected data from May 17, and Fig. 5.12 (d, f and h) shows the results of the May 19 survey.

Therefore, there is a shift in the maximum measured temperature with respect to distance from the outfall, which can also be seen in Fig. 5.13 and explained as a result of tidal currents. Evaluation of the plume dispersion under different tidal and wind conductions is the subject of a forthcoming paper by the authors.

As previously mentioned, jet-like mixing close to the outfall enhances vertical mixing and increases plume thickness. Conducting a wide range of experiments on the dilution of turbulent jets (Fig. 5.1), Moawad (1998) reported a curvilinear pattern for the increase in jet thickness in deep ambient conditions. Kim and Cho (2006) provided estimations for the maximum plume thickness ($h_{max}$) and the distance from the outfall to the maximum plume penetration region ($x_{max}$), as:

$$h_{\max} = 0.42F_0'\sqrt{h_0 b_0} \quad \textbf{(5.3)}$$

$$x_{\max} = 5.5F_0'\sqrt{h_0 b_0} \quad \textbf{(5.4)}$$

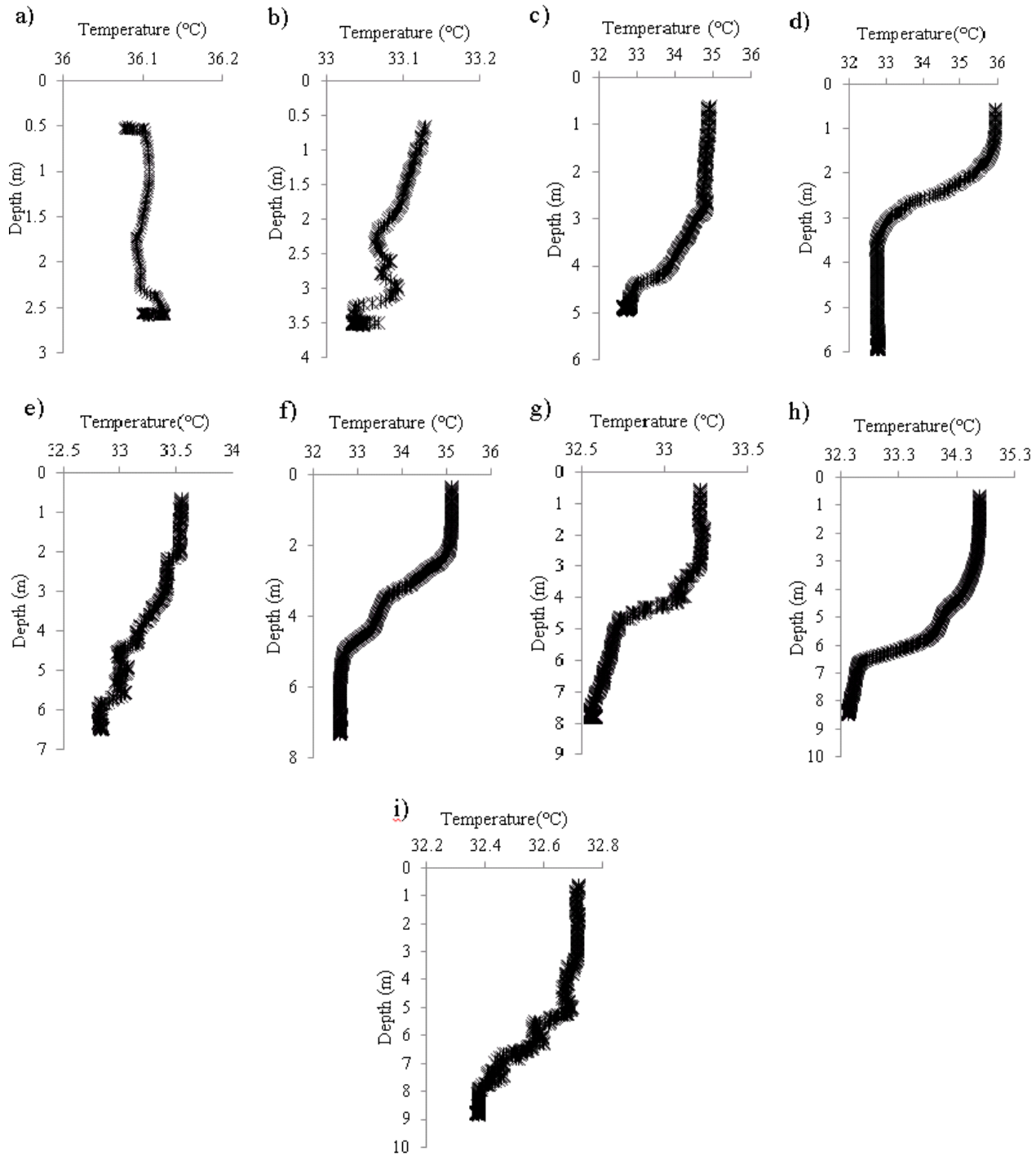


**Figure 5.12: Vertical profile of temperature in the centerline of the plume at the stationary measurement point from Fig. (5.b) (note the unequal scaling)**

Equation (5.3) predicts the value $h_{max}$=5.8 m as the maximum plume thickness expected to be seen at $x_{max}$=100 m from the outfall (Eq. 5.4). However, Eq. (5.3) is applicable to discharges in deep ambient conditions, while the case under study in this project is shallow. Indeed, the shallow water depth in this study does not allow observation of the plume at its maximum thickness, but the shallow depth is expected to reduce the dilution rate in the plume. Kaufman and Adams (1981) used a criterion for determining the shallow ambient condition, e.g., if $h_{max}/H$>0.75, the situation is considered to be shallow, where $H$ is the water depth at the $x_{max}$. At $x_{max}$=100 m, based on our field data, we obtained $H$=1 m, leading to $h_{max}/H$=*5.8*, which is considerably larger than 0.75. Therefore, the ambient water body in this case is shallow, and $h_{max}$ is limited by the water depth. The fact that the ambient water is shallow will be considered in the next section, using a shallowness correction factor in the calculation of dilution.

After rising from the bed, the thickness of the plume starts to decrease due to the buoyancy-induced spreading. This is the result of competition between the vertical mixing and lateral spreading (Jay et al. 2009). Conducting a field survey on the Grand Haven River plume in Lake Michigan, Nekouee (2010) reported the same pattern for variation of the plume thickness after the detachment point. The thickness of the plume starts decreasing from the maximum penetration point and reaches its terminal thickness at a certain distance downstream (Baddour et al. 1989). This is the region where the vertical mixing and lateral spreading become balanced. This is in agreement with the results of the present measurements, where the density gradient has reduced vertical mixing and enhanced lateral spreading, resulting in a reduction of the thickness and reaching a terminal thickness, as can be observed in Table 5.2. Stolzenbach and Adams (1971) proposed the following formula for estimating the far-field thickness of the plume:

$$h_{far} = 0.21F_0'\sqrt{h_0 b_0 / 2} \qquad \textbf{(5.5)}$$

Considering $F_0'$=0.9, $b_0$=500 m and $h_0$=1, the plume thickness in the far field is calculated to be 2.8 m, which is in reasonable agreement with the measured data (2.5 – 3 m) as presented in Table 5.3 and Fig.

5.12. The thickness of the plume began increasing at the end of the near field due to the effect of ambient water turbulence, and reached the full vertical-mixing condition by 5.4 km from the outfall (S9).

### 5.5.4 Detachment point

The detachment point is important in describing the mixing behavior of the plume. Vertical mixing is greatly diminished after this point, and buoyant lateral spreading controls the mixing process. The detachment depth is generally scaled by the jet-to-plume-length scale ($L_M = M_0^{3/4} / J_0^{1/2}$) and is influenced by different parameters such as the discharge densimetric Froude number ($F_0$), outfall aspect ratio ($A$), bed slope ($S$), and bottom friction ($f_b$) (Jirka 2007). Atkinson (1993) provided a comprehensive review of the available formulas for estimating the detachment location distance from the outfall, some of which are presented in Table 5.4.

In this study, the vertical profile of the plume was measured at different locations along the jet axis of the plume, and a summary of the plume thickness at each of the measured points along the plume axis is provided in Table 5.3.

**Table 5.3:Summary of the stationary measurement points along the plume axis**

| Point | S1 | S2 | S3 | S4 | S5 | S6 | S7 | S8 | S9 |
|---|---|---|---|---|---|---|---|---|---|
| Date | May 15 | May 15 | May 17 | May 19 | May 17 | May 19 | May 17 | May 19 | May 7 |
| Distance (km) | 1.4 | 2.1 | 2.9 | 3.3 | 3.9 | 4.2 | 4.7 | 4.9 | 5.4 |
| Thickness (m) | 2.5 | 3.5 | 3 | 2.5 | 3 | 2.5 | 3 | 6 | 5 |
| Depth (m) | 2.5 | 3.5 | 5 | 5.6 | 6.1 | 7.3 | 7.8 | 8.5 | 8.8 |

The measured data show that the plume detached from the bed at approximately 2.8 m depth between 2.1 and 2.9 km from the outfall. This parameter has also been estimated from different empirical formulas (Table 5.4). Detailed discussion on these formulas can be found in Atkinson (1995). Safaei's (1974) equation was developed for a slope rate of 1% <S<4%, and it better predicted the detachment depth ($h_d$) compared to the other formulas presented in Table 5.4. It should be noted that Safaei (1974) used $L_s=U_0^2/g_0'$ as the length scale. However, Atkinson (1995) used the $L_s$ presented in Table 4, based on Arita et al. (1986). The later definition of $L_s$ provided better estimation of $h_d$ in this study.

**Table 5.4:Estimation of the plume detachment point**

| | Proposed formula for estimating the detachment depth | Length scale | Detachment depth (m) |
|---|---|---|---|
| Hauenste (1983) | $h_d = L_M(0.6\pm0.3)S^{1/4}$ | $L_M = M_0^{3/4}/J_0^{1/2}$ | 1.5 |
| Chu and Jirka (1986) | $h_d = 0.6L_sS^{1/4}$ | $L_s = h_0\left(\frac{(2F_0^2+1)^{3/4}}{2^{3/4}F_0^{1/2}}\right)A_s^{-1/4}$ | 1.5 |
| Safaei (1974) | $h_d = 0.914L_sF_0^{-3/2}$ | $L_s = h_0\left(\frac{(2F_0^2+1)^{3/4}}{2^{3/4}F_0^{1/2}}\right)A_s^{-1/4}$ | 2.7 |
| Observed Value | - | - | 2.8 |

Various studies have discussed the relationship between bottom detachment and the local densimetric Froude number. It is generally argued that bottom detachment occurs when the local densimetric Froude number falls below a critical value ($F_{cr}$), leading to the dominance of buoyancy effects as compared to momentum effects. Safaei (1979) reported that the jet was attached to the bed for $F_0 \geq 2.5$. Jirka (2007)

used $F_{cr}$=1.5 based on the results of Almquist and Stolzenbach (1980). In this study, the bottom detachment was observed with a densimetric Froude number lower than 1.

### 5.5.5 Variations of maximum temperature and velocity along the jet

Variations of velocity and temperature along the plume determine the minimum dilution of the jet ($S_{min}$). The minimum dilution parameter ($S_{min}$) for temperature is defined as the ratio of excess temperature on the jet centerline ($\Delta T_m = T - T_a$) to the maximum excess temperature at the outfall ($\Delta T_0 = T_0 - T_a$). For velocity, $S_{min}$ is the ratio of the velocity on the jet axis ($U_m$) to the discharge velocity ($U_0$).

The minimum dilution rate could also be related to the averaged dilution ($S_{min} = \alpha S_{avg}$). The parameter $\alpha$ is determined based on the discharge condition and outfall geometry, e.g., $\alpha$=0.72 (Rajaratnam 1976) and $\alpha$=0.83 (Fischer et al. 1979). Figure (5.13) presents the variation of temperature along the plume axis from the field-measured data from different dates. As the surveys were carried out in different regions, the horizontal extent of the presented graphs is not the same for all of the survey dates. Variation of the temperature profiles from the successive survey dates are very similar up to around 700 m from the outfall. This is the limit which may be considered as the ZFE for the temperature. The length of the ZFE for temperature has typically been reported to be shorter than that for velocity due to the higher turbulent diffusion coefficient for temperature (Lin et al. 1977). However, in our case, the bed friction can be considered as the main reason for having a shorter ZFE length for velocity than for temperature.

The May 18 survey was mostly focused on the near-field part of the plume, and the presented data for this date are in alignment with the May 19 data. The deviation in results from different survey dates can be attributed to different discharge and ambient climate conditions, particularly wind speed and direction. The differences in the reults start to rise between 2 and 3 km from the outfall location, and therefore, this region can be considered as the transition region from the near-field to the far-field of the plume.

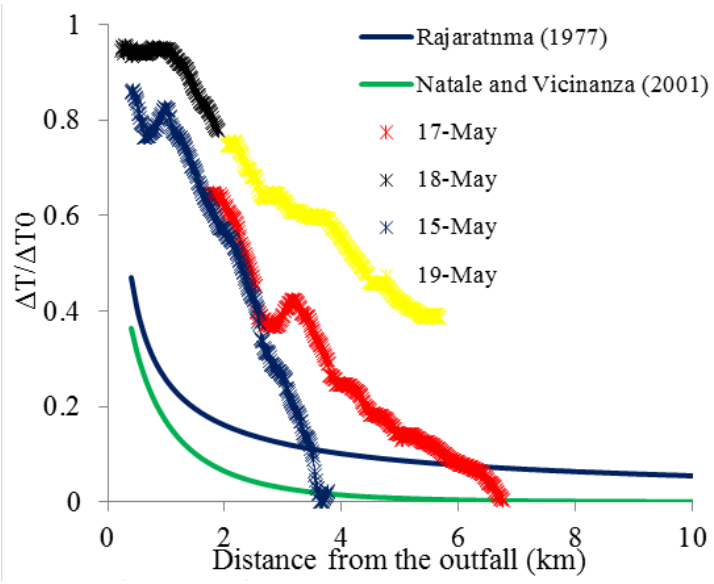


**Figure 5.13: Variation of maximum temperature along the plume**

Various formulas have been proposed in the literature for estimating variations in temperature and velocity along the jet axis, as summarized in Table 5.5 and Table 5.6. The formulas mostly have a general form, with different constants corresponding to the specific discharge conditions. However, it should be noted that these formulas were developed based on deep condtions where the sea bed does not limit the vertical spreading of the jet and the corresponding vertical entrainment of the ambient water which controls the dilution in the geophysical scale cases (Horner-Devine 2015). As explained earlier, the outfall in the present study is confined on the bottom and one side. Jirka et al. (1981) defined the shallow water dilution factor ($r_s$) as the ratio of the observed dilution in the shallow water ($S_{min}$) to the predicted dilution in the deep water ($S'_{min}$), i.e., $r_s=S_{min}/ S'_{min}$, in order to incorporate the reducing effect of shallowness on the dilution rate. They proposed the following equation to estimate $r_s$ :

$$r_s = \left( \frac{0.75}{h_{\max} / H} \right)^{0.75} \qquad \textbf{(5.7)}$$

Using $H_{max}$=5.8 m, obtained from Eq. (5.3), and $H$=1 m as the depth at $x_{max}$=100 m obtained from (5.4), the ratio $r_s$=0.2 was estimated in this study. This coefficient will be applied to the values predicted

by the formulas provided in Table 5.5, where $R_{i0}$ represents the Richardson number ($R_{i0}= Fr_0^{-0.5}$) which is equal to 0.56 and λ is the bed slope.

From Fig. 5.13, an average dilution of 0.65 can be estimated by the detachment point for the plumes observed in the May surveys. However, the average calculated dilution from the Table 5.5 formulas is about 0.19. After applying the shallowness correction factor ($r_s$=0.2), the average dilution was estimated to be 0.68, which is in good agreement with the observed value of 0.65.

**Table 5.5: Variation in temperature along the buoyant jet axis**

| | Formula | Shallowness modified dilution | Observed value |
|---|---|---|---|
| Rajaratnam (1977) for $R_{i0}$ = 0.15 to 0.56 | $\frac{\Delta T_m}{\Delta T_0} = 4.42 \frac{R_{i0}^{1/3}}{\left(x/L_Q\right)^{2/3}}$ | 0.8 | 0.65 |
| Natale and Vicinanza (2001) | $\frac{\Delta T_m}{\Delta T_0} = e^{-0.15\left(-\frac{x}{L_Q}\right)^{0.62}}$ | 0.68 | 0.65 |

The variation in the depth-averaged velocity along the jet axis has been compared with some of the empirical formulas provided in Table 5.6. The measured data were generally found to be in the same form as the equation proposed by Rajaratnam (1976). However, the discharge length scale ($L_Q$) was found to be a better choice than $b_0$ when used as the length scale. This can be explained as a result of the high aspect ratio of the outfall in this study. Fitting the measured data and the modified form of Rajaratnam's formula, an optimum value of $C$=4 was obtained. The higher value for the C coefficient (compared to the typical value of 3.1) is due to the lower declination rate for the jet velocity. This could be a result of the shallow ambient condition and the confinement of the jet on one side, which restricts the entrainment of

the ambient water and consequently reduces the dilution rate (Volker 1993, Shinneeb et al. 2011). Moreover, the present results are consistent with Deo and Nathan (2007), where a lower rate of minimum dilution downstream of the outfall location was reported for a discharge channel with a large aspect ratio.

**Table 5.6:Variation of velocity along the buoyant jet axis**

| | Formula | Corresponding assumptions |
|---|---|---|
| Rajaratnam (1988) | $\frac{u}{u_m} = 15.3\frac{R_{i0}^{1/10}}{x/L_Q}$ | x/LQ>30 and Ri0>0.5 |
| Rajaratnam and Humphries (1984) | $\frac{u}{u_m} = \frac{C}{\sqrt{x/b_0}}$ | * Surface jet |
| Rajaratnam (1977) | $\frac{u}{u_m} = 5.68\frac{R_{i0}^{1/3}}{\left(x/\sqrt{A_0}\right)^{2/3}}$ | Ri0 = 0.15 to 0.56 |
| Natale and Vicinanza (2001) | $\frac{u}{u_m} = e^{-0.03\left(\frac{x}{\sqrt{A_0}}\right)^2}$ | |
| Rowland et al. (2009) | $\frac{u}{u_m} = \left(\frac{x}{B}\right)^{-1/2}$ | |
| Rajaratnam (1976) | $\frac{u}{u_m} = D\frac{L_Q}{x}$ | ** for x>ζ0 |

*C: experimental coefficient

**D: experimental coefficient

## 5.6 Conclusions

In order to investigate the near- and far-field mixing patterns of surface outfalls, an intensive field study was conducted on the Ras Laffan Industrial City surface outfall in Qatar, which has an aspect ratio of about 400. The spatial distribution of the thermal plume effluent and the jet velocity were mapped using data from CTD, aDcp, and GPS. The employed real-time field measurement of the hydrodynamic and

temperature field made it possible to examine various aspects of mixing processes that have been rarely conducted in previous field studies. The investigated outfall in this study is unique due to its very large aspect ratio, shallow water depth leading to vertical confinement effect, and also the presence of lateral confinement effect. Using the measured data, a comprehensive three-dimensional perspective of the mixing processes in the near-field and the far-field (3km*5km region) of the outfall was developed. This consequently provided us with the opportunity to investigate different aspects of the effect of the outfall geometry on the mixing processes and to investigate the jet-like and plume-like mixing processes separately.

Various plume characteristics were discussed in this study, such as longitudinal variations of the plume, entrainment characteristics, detachment point, and spatial extent of different zones of the plume (e.g., length of the zone of flow establishment and near field), and plume thickness, as well as variations in maximum temperature and velocity along the jet. Variation of the plume thickness under the jet-like and plume-like mixing mechanisms in the near-field and far-field regions of the shallow outfall was investigated separately and the full vertical mixing region was determined. The mixing characteristics due to various mechanisms were quantified in different regions of the outfall separately. The entrainment coefficients of 0.67 and the plume spreading rate of 0.78 were estimated for the jet-mixing and buoyant-spreading processes, respectively.

The vertical confining effect of the shallow ambient water body condition was found to halve the average dilution of the jet plume. The increase in minimum dilution was also found to be affected by the high aspect ratio of the outfall and the shallow ambient water body condition. The effect of outfall confinement on the average dilution in the jet-like mixing region was investigated and the inhibitive effect of shallow ambient condition on mixing was quantified using a shallow water dilution factor ($r_s$=0.2). The estimated value showed that the shallow discharge condition of the outfall reduced the minimum dilution potential of the outfall to one fifth.

The extents of the different regions of the jet were determined from different approaches based on the measured temperature field. It was also concluded that the length of the ZFE was greatly influenced by the aspect ratio of the outfall. Bed friction was also found to be effective in shortening the length of the ZFE for velocity with respect to temperature.

A remote-sensing method was also proposed to study the mixing process of thermal plumes. LandSat7 thermal infrared satellite images were calibrated using the temperature data measured with a CTD on May 15, 2014 as well as the data from environmental buoys. The good agreement between the temperature contours from the field survey and the calibrated satellite photos showed that the proposed method can be used to study the near- and far-field mixing of the thermal plume as well as to investigate the parameters affecting the plume shape, such as dominant wind speed and direction. Using the field-measured data and calibrated satellite photos, the effects of tidal currents and wind-generated waves on the near- and far-field fates of the plume can be studied, and is the subject of a subsequent paper.

**ACKNOWLEDGEMENTS**

This publication was made possible by NPRP Grant 4-935-2-354 from the Qatar National Research Fund (a member of the Qatar Foundation). The statements made herein are solely the responsibility of the authors.

# Chapter 6:

## Mixing of the Ras-Laffan desalination plant discharge; Part II. wind effects on the near-field plume dynamics

**Considered to be submitted to the Journal of Environmental Fluid Mechanics**

**Authors**: Abolghasem Pilechi, Colin D. Rennie, Majid Mohammadian, Hazim Qiblawey

### 6.1 Abstract

The effect of wind on the near-field dynamics of a surface thermal plume was investigated using a combination of remote sensing and numerical modelling approaches. Temperature maps of the Ras Laffan Industrial City (RLIC) effluent plume were generated from LandSat thermal infrared (TIR) imageries collected on multiple days in 2013 and 2014. A numerical simulation was also carried out for validating the relative importance of the tidal and wind driven currents on plume characteristics. In contrast with previous studies that ignored the wind effect in the near-field region, the long-shore and cross-shore winds were found to affect the plume trajectory and the mixing rate in the near-field of the plume. Comparison of deflection angle of the plume in different wind conditions showed that the plume trajectory was sensitive to the long shore wind higher than 2 m/s. The off-shore wind also enhanced the near-field mixing up to 20%. A previous method by Nekouee et al. (2013) for classifying the plume under wind action was not found to be effective for shallow water cases due to the influence of bed shear. Instead, two non-dimensional parameters, $WI_1=U_{wl}/U_0$ [ratio of the long-shore wind speed ($U_{wl}$) to the discharge velocity ($U_o$) ]and $WI_2= U_{wc}/U_0$ [ratio of the cross-shore wind ($U_{wc}$) to the discharge velocity] have been defined for quantifying the relative importance of wind and discharge momentum on the plume deflection and the dilution.

Keywords: Wind - Mixing - Surface outfall- Remote sensing

## 6.2 Introduction

Coastal mixing is an important area of research in environmental hydraulics due to the great number of river and industrial discharges into oceans, seas and lakes. The diversity of the ecosystem services provided by coastal ecosystems and their influence on human life makes understanding of coastal mixing essential. Coastal mixing is complicated by the variety and unsteadiness of environmental forces influencing the mixing process. Tidal currents and wind are critical parameters in the coastal mixing process. The wind influence on the coastal mixing process can be considered by looking at wind-generated waves or wind-driven currents.

The spatial and temporal scale of the mixing process varies with respect to the dominant active forces in different distances from the outfall. Different regions of the outfall are consequently named and categorised based on the mechanism controlling mixing. The mixing process can thus be studied in the near-field, mid-field and the far-field of an outfall. The near-field momentum balance of the plume considers discharge momentum, barotropic and baroclinic pressure, and turbulent interfacial stress between the plume layer and the ambient water or the bed (in a shallow water case) (Horner-Devine et al. 2015).

Coriolis force, generated by the earth rotation, is assumed as a secondary forcing factor and is ignored in the near-field mixing process (Hetland 2010). The maximum distance that a particle can travel before being affected by the earth's rotation is determined by the Rossby Radius ( $R = \sqrt{gh} / f$ ) where $g$=9.81$m^2/s$ is the gravity acceleration, $h$ is depth and $f$ is the Coriolis parameter (Cushman-Roisin and Beckers 2011). Considering the average depth ($h$) of 5 m and $f = 1\times14{-}4\ s^{-1}$, the Rossby Radius is estimated to be approximately 61.5 km in this study. As the extent of investigated region (see Chapter 5) is much smaller than the Rossby Radius, the Coriolis effect is considered to be negligible.

In general, for a large river or outfall plume in a coastal water the near-field region is within the Rossby Radius from an outfall before the turning due to the earth's rotation affects the plume trajectory (Hetland

and Hsu 2013). The Coriolis force increasingly dominates the plume dynamics in the mid-field which is the transition region between the near-field and the far-field (Jirka et al., 1981). The plume is not affected by the discharge momentum in the far-field and its dynamics is governed by the earth rotation, wind stress, buoyancy, the ambient flow and possibly the bed stress (Horner-Devine et al. 2015).

The mixing process in the near-field has lower temporal and spatial scale than in the far-field where the mixing is controlled by the ambient water conditions (Nekouee 2010). Understanding the near-field mixing of plumes is important because the near-field has the highest concentration of the discharged material and thus the greatest potential concern for short-term immediate toxicity of the disposed materials. Moreover, mixing is more vigorous in the near-field region, and this mixing determines the distance to the far-field region with relatively low dilution (Hetland 2010).The plume dynamics in the near-field region is associated with rapid spreading due to entrainment of ambient water of different density into the discharge flow. The turbulence generated as a result of momentum difference between the discharge and receiving water body causes entrainment of the low-momentum ambient water in both horizontal and vertical directions into the jet (Wang et al 2015). This process is also known as jet-like mixing (Jirka, 2004) and results in a high dilution rate in this region.

The wind influence on the horizontal and vertical structure of coastal plumes as a result of upwelling and downwelling processes within the Ekman transport have previously been studied in the field (Hickey et al., 1998, Sander and Garvin 2001, Horner-Devine et al., 2009) and numerically (Whitney and Garvine 2005, Choi and Wilkin, 2007). Whitney and Garvin (2005) introduced a wind strength index (Ws) as the ratio of the wind-driven and buoyancy driven velocity scales to determine the wind effect on the plume shape for the Delaware Coastal estuary buoyant outflow. The wind effect is generally assumed negligible up to the end of near-field where the initial discharge momentum is diminished (Kakoulaki 2014). Consequently, previous studies on river plumes have mostly disregarded the influence of wind on the near-field dynamics, considering the influence of wind only in the far-field region (e.g. Jones et al. 1996, Horner-Devine et al. 2009, Zhang et al. 2009, Hetland 2010). The wind strength index proposed by

Whitney and Garvin was also defined for large scale mixing process in the far-field, where Coriolis forces also affect the plume dynamics.

Nekouee et al. (2013) developed a general classification method for determining the effect of wind on plume dynamics (see Fig. 2.3). They used a modified Richardson number ($Ri^* = g_0' h_0 / W^{*2}$) based on the wind shear stress ($W^*$), where $h_0$ is the initial plume thickness. The modified gravity attributable to buoyancy $g_0' = g\Delta\rho_0/\rho_a$ depends on the initial density difference ($\Delta\rho_0 = \rho_a - \rho_0$) between initial discharge ($\rho_0$) and the ambient water ($\rho_a$). The wind shear stress is calculated as $W^* = \left| C_D \rho_{air} / \rho_a \, W_{10}^2 \right|^{1/2}$ where $C_D$ = 0.0013 is the drage coefficient, $\rho_{air}$ is the air density and $W_{10}$ is the onshore/offore wind component at 10m from the water surface. The wind effect on the plume was classified in three groups of $Ri^* > 4.5 \times 10^6$ for no-wind influence, $5.5 \times 10^3 < Ri^* < 4.5 \times 10^6$ for moderate wind influence in which the plume was affected by the wind action without shore-line attachment, and $Ri^* < 5.5 \times 10^3$ for shore-line attachment under wind action. However, their method was for the far-field region, thus they did not consider the interaction of the discharge momentum. In addition, the mixing rate under wind action was not investigated in their study.

Kakoulaki et al. (2014) investigated the importance of the wind on the near-field of the Merrimack River plume using a drifter tracking approach. They reported the influence of wind on the near-field dynamics of the plume for wind speed > 4 m/s. However, like the Nekouee et al. study, the employed approach in their study did not permit investigation of the effect of wind on the near-field mixing rate. As previously mentioned, turbulence is one of the main mixing sources in the near-field region. In one of the most recent studies, Wang et al. (2015) studied the wind influence on the near-field of the Merrimack River plume. They proposed a modified Turbulent Kinetic Energy (TKE) production term to consider the effect of currents and wind forcing mechanisms in addition to the discharge momentum and buoyancy. They reported that the river discharge and the magnitude of the onshore wind had a similar importance, and both were more significant than the tidal range on the turbulence intensity in the near-field of the Merrimack River plume. These recent studies have demonstrated that wind is more significant than

previously considered in the near-field mixing process. This consequently implies that more dedicated studies should be conducted on the effect of wind on the near-field dynamics of coastal plumes.

The goal of this study is to provide insight on the relative importance of the wind with respect to the discharge and ambient flow in the near-field mixing of shallow buoyant coastal plumes using an inexpensive and practical remote sensing method. This paper is the next stage of the research conducted in Chapter 5 on the Ras Laffan Industrial City (RLIC) effluent in Qatar (Fig. 6.1). RLIC has a surface outfall located at 25° 53.480' North (latitude) and 51° 34.483' East (longitude) with average annual discharge rate of 200 $m^3/s$. The outfall is located inside the Ras Laffan port. The outfall width is about 300 m and is discharging in shallow water (1m depth at the outfall) which is analogous to a medium size river plume case. The plume was reported as vertically uniform and attached to the bed up to the 3m depth contour (about 2.5 km from the outfall)in Chapter five. Due to the large aspect ratio of the outfall, vertical mixing is often dominant in geophysical scale outfalls (Horner-Devine et al. 2015). However, the shallow water condition in this case restricted vertical mixing. The horizontal advection of the plume is also controlled by buoyancy currents generated by the density difference between the plume and the ambient water, discharge momentum, and the ambient flow. In this study lateral mixing is restricted by the large aspect ratio of the outfall (Chen and MacDonalds 2006) as well as lateral confinement on one side by a jetty. Therefore, the case can be categorised as a confined jet.

In this study, various forcing factors that determine the plume dynamics and affect the mixing process are evaluated. The effects of tidal currents and wind are investigated using thermal plume images obtained using the method proposed in Chapter five as discussed in Section 6.2. The relative importance of wind and tidal currents on the plume dynamics during the tidal cycle are investigated using a numerical simulation.The measured wind, water level, and temperature data are used for applying the environmental forces in the numerical model


**Figure 6.1: Ras Laffan Industrial City Port. The photo was adopted from Google Earth**

This paper is organised as follows. In Section 6.2 the methodology of this study is explained including the employed remote sensing technique and the numerical model. The results obtained from the remote sensing and numerical approaches are presented in Section 6.3. The discharge and wind condition have also been summarised as the effective driving sources in the mixing process. Section 6.4 provides discussion on the relative importance of the investigated parameters on plume characteristics. In this section, the effect of wind on the near-field plume dynamics is investigated using two innovative non-dimensional parameters. Some concluding remarks including the effect of different wind components on the plume dynamics and dilution complete the study in Section 6.5.

## 6.3 Methodology

The remote sensing approach proposed in Chapter five for using LandSat 7 satellite TIR imageries was employed for investigating the dynamics of a surface thermal plume. The method has been previously successfully validated on the RLIC outfall using ground truth data of surface water temperature. In this study, this method was used for investigating the relative importance of wind and tide on the dynamics of the RLIC thermal plume. In the first step, thermal spatial maps of the RLIC thermal effluent plume were generated from the available LandSat TIR images with zero cloud coverage for the period January 2013 until May 2014. Measured wind data were also obtained from environmental buoys located close to the entrance of the port.

The hydrostatic version of the three-dimensional open-source Delft3D-Flow hydrodynamic model (Morelissen et al., 2013) was also used to validate the observed results from the remote sensing approach for a high wind condition case. The model had ten vertical layers in the sigma coordinate sytem (Phillips 1957) and covered the entire port region with an expanding orthogonal curvilinear grid with minimum grid size of 30m at the outfall. The k-ε turbulence model was used for modelling the turbulence mechanism. Measured water level, temperature and salinity data were used for setting up the model. The water level in the port varies during the semidiurnal tidal cycle with a tidal range of 3 m. Observed tidal ranges were used to drive the numerical model. Based on measured field data (Chapter five), the salinity was assumed uniform. The measured time series of effluent discharge rate and temperature were used as the discharge condition.

## 6.4 Results

### 6.4.1 Remote Sensing

Thermal images of the RLIC effluent plume were generated from the LandSat7 TIR images for the period January 2013 until May 2014. Fig. (6.2) presents some of the thermal images obtained from the remote-sensing approach. The LandSat images were taken every 8 days in the RLIC region. However, the presented images in Fig. (6.2) are for the dates with zero cloud coverage. The duration of a wind event for generating a fully developed current is an important parameter when investigating wind driven current. This parameter is a function of the water depth and the wind speed (Whitney and Garvine 2005) and should be long enough to generate a developed current. Following Nekouee (2010), six-hour averaged wind speed and direction (with respect to the North) before the satellite image capture times were used in this study (Table 6.1). The wind data are presented by a scaled vector on each contour plot in Fig. (6.2). The effluent discharge rate and the discharge densimetric Froude number for each image are also provided in Table 6.1. Discharge densimetric Froude number ($Fr_0 = U_0/(g_0'(h_0 b_0)^{1/2})^{1/2}$) represents the ratio of momentum to the buoyancy force scales at the discharge where $U_0$ is the discharge velocity, $h_0$ is the discharge depth and $b_0$ is the outfall width. The $g_0' = (\Delta\rho_0/\rho_a)g$ parameter is the initial buoyancy

acceleration where g is gravitational acceleration, and $\Delta\rho_0 = \rho_a - \rho_0$ is the difference between the discharge density ($\rho_0$) and the receiving water body density ($\rho_a$).

**Table 6.1 Discharge and wind condition at the image capturing time**

| Date | 6 hour averaged wind speed (m/s) | 6 hour averaged wind direction (degree) | $WI_1$ | $WI_2$ | Discharge ($m^3/s$) | $Fr_0$ | Deflection | Dilution by 3km | Ri* |
|---|---|---|---|---|---|---|---|---|---|
| 4/13/2014 | 3.87 | 328.82 | 4.32 | 2.61 | 230.00 | 5.55 | 20.4 | 0.55 | 849 |
| 2/5/2013 | 5.80 | 311.72 | 5.02 | 5.63 | 230.55 | 5.25 | 48.4 | 0.5 | 422 |
| 2/21/2013 | 7.80 | 318.28 | 7.84 | 6.99 | 222.78 | 4.43 | 28.3 | 0.38 | 303 |
| 6/13/2013 | 7.88 | 306.33 | 5.84 | 7.94 | 239.72 | 5.41 | 43.2 | 0.63 | 232 |
| 3/9/2013 | 3.87 | 315.94 | 3.86 | 3.73 | 216.39 | 4.87 | 23.9 | 0.55 | 962 |
| 3/28/2014 | 2.15 | 218.90 | -2.22 | 1.79 | 225.83 | 4.46 | 19.2 | 0.37 | 4038 |
| 5/12/2013 | 3.78 | 300.23 | 2.40 | 4.12 | 237.78 | 4.87 | 17.4 | 0.58 | 1215 |
| 5/15/2014 | 0.39 | 180.00 | -0.50 | 0.00 | 234.44 | 4.58 | 23.8 | 0.5 | 125645 |
| 5/28/2013 | 1.20 | 199.69 | -1.41 | 0.50 | 240.83 | 4.20 | 11.6 | 0.23 | 16625 |
| 9/1/2013 | 2.73 | 124.69 | -1.92 | -2.77 | 243.33 | 4.94 | 6.1 | 0.38 | 2378 |

In order to investigate the effect of tide on the plume dynamics the daily tidal graphs are provided for each presented image in Fig. (6.2). The tidal phase at the capturing time of each satellite image is also shown on each tidal graph (red arrow). The satellite photos were all taken at 10 AM local time for Doha, Qatar. However, the gradual shift in the tidal cycle has caused different tidal phase in the captured thermal effluent plumes.

a) Sept 1, 2013

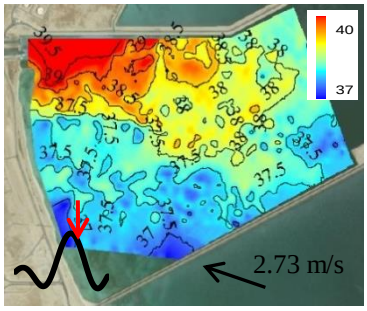


b) May 15, 2014

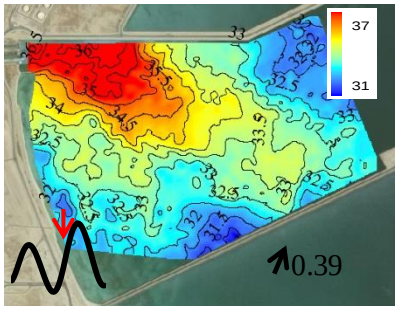


c) Mar 9, 2013

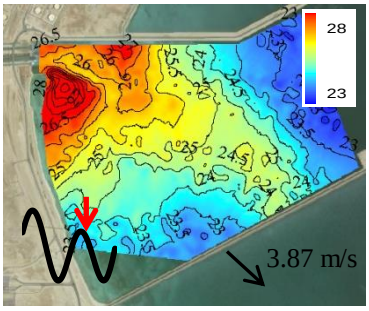


d) May 12, 2013

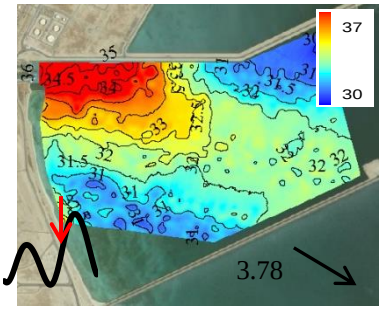


e) March 28, 2014

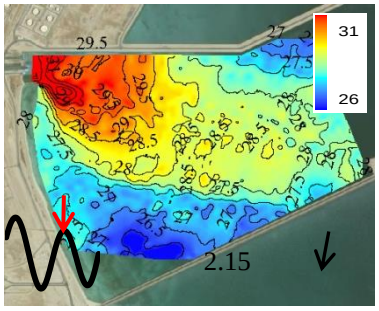


f) Feb 21, 2013

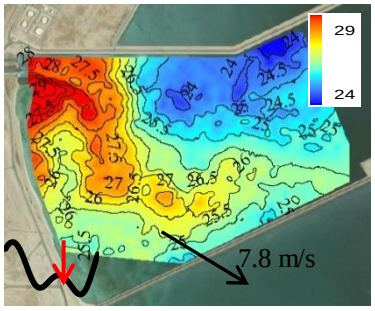


g) Jun 13, 2013

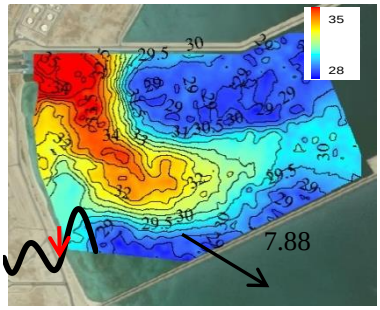


h) Feb 5, 2013

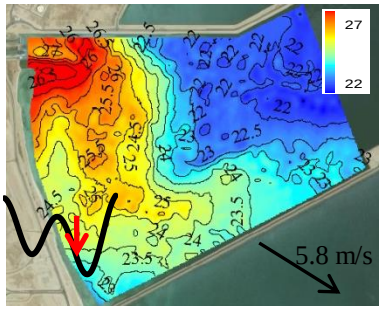


i) April 13, 2014

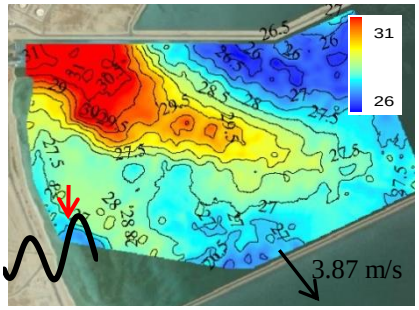


j) May 28, 2013

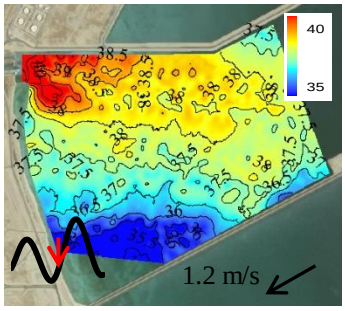


**Figure 6.2:Temperature field for Las Raffan outfall plume generated from TIR imagery for various days between February 5th, 2013 and May 15, 2014. The wind speed and direction and tidal phase at the time of data collection are indicated. The underlying image is adopted from Google Earth**

## 6.5 Numerical model

Considering the small variation in the effluent discharge rate (less than 15%, see Table 6.1), the observed variation in the jet deflection in Fig.(6.2) can be attributed to the tidal and wind conditions. In order to investigate the relative influence of wind and tidal current on the plume trajectory, numerical simulations were conducted for different cases in Fig. 6.2. Due to the outfall location (inside the port) and the preliminary simulation results, the effect of wave action was assumed negligible. Fig. 6.3 presents simulation results for the depth averaged velocity for Feb 21, 2013 as a case with high wind and low discharge condition in scenarios with and without wind. Comparing the directions of the depth averaged velocity (Fig. 6.3) and the wind (Fig. 6.2), it can be clearly seen that the wind driven currents controlled the trajectory of the plume. Compared to the case with wind forcing (Fig. 6.3b), the scenario without wind forcing (Fig. 6.3a) plume current dissipates quickly and no flow recirculation cell is generated along the southern jetty. Tidal currents are strongest during ebb and/or flood conditions. However, the simulation results showed that the tidal currents were not strong enough to change the trajectory of the plume and only moved the plume front back and forth during a tidal cycle.

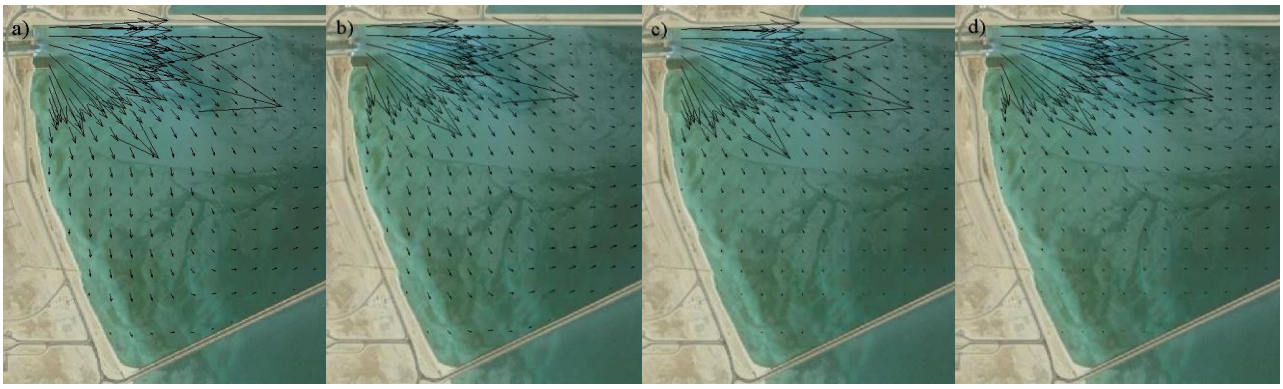


**Figure 6.3: Simulated depth averaged velocity field on Feb 21, 2013: a) with wind and tide b) with wind only c) with tide only d) with neither wind nor tide (Compare to observed temperature field shown in Fig.6.2f. The wind speed (7.8 m/s) and direction (318°) on Feb 21, 2013, was used in Fig.6.3a and Fig.6.3c)**

## 6.6 Discussion

The thermal effluent in this study is lighter than the ambient environment and flows on the water surface when discharged from the surface outfall. Consequently, the outfall plume will spread under the combined action of discharge momentum flux, buoyancy flux, and wind forcing. However, momentum flux will dominate in the near-field. Furthermore, based on $W_s=u_{wind}/u_{dis}$, where $u_{wind}$ is the estimated wind-drive spreading velocity of the plume and $u_{dis}$ is the estimated buoyancy driven spreading velocity (Whitney and Gervine 1995), wind will spread this particular plume more than buoyancy if the wind exceeds 1.5 m/s. Therefore, the effect of buoyancy-driven flow on the plume dynamics is considered negligible with respect to both discharge and wind in the following discussion.

The thermal images (Fig.6.2) show that the near-field trajectory of the plume varied dramatically as a function of the wind. The discharge momentum drove the plume trajectory along and spreading away from the northern confining jetty, as observed under no-wind conditions (Fig.6.2b). The observed plume on May 15 (Fig.6.2b) had the lowest wind and one of the highest observed discharge conditions. Therefore, the plume trajectory in this case can be considered as the no-wind condition case. The plume detached from the side jetty at about 2 km downstream of the outfall. This could be attributed to the shear effect by the confining jetty and the bathymetry features. On other days with stronger wind, the wind component orthogonal to the discharge angle diverted the plume towards the dominant wind direction. Thus, in contrast with previous assumptions, wind influence is significant in the near-field region of the plume where the discharge momentum has not been completely dissipated. Furthermore, the wind action caused shore attachment close to the outfall in some cases (e.g. Fig. 6.2c,f,h). This could be very important from an environmental engineering point of view, because an effluent that remains close to shore can more readily contaminate coastal communities and ecosystems.

The February 21 (Fig. 6.2f) and June 13 (Fig.6.2g) cases both had a similar wind condition; however, shore attachment was observed on February 21 but not on June 13. This is attributed to the lower discharge rate on February 21 and implies that the effect of wind and discharge momentum on the plume

trajectory should be considered together. Therefore, in this study a scale parameter $WI_1=U_{wl}/U_0$ was defined as the ratio of the long-shore wind speed ($U_{wl}$) to the discharge velocity.

The deflection angle from the initial discharge by 3 km downstream the outfall was calculated for each plume in Table 6.1.The distance was chosen based on the reported range in Chapter five for the near-field region. Variation of the plume deflection angle from the initial discharge with $WI_1$ is provided in Fig. (6.4). Due to the confinement of the plume on one side, the cases in which the wind pushed the plume against the confining jetty (negative $WI_1$) have not been presented in Fig.(6.4). The minimum effective wind speed on the plume dynamics was 2 m/s (Fig.6.2). This is about half of the reported value by Kakoulaki (2014) (4 m/s) for the Merrimack River plume. The lower effective wind speed in this study is attributed to the shallow discharge condition which has caused faster dissipation of the discharge momentum and moved the intermediate field closer to the outfal, and the higher discharge rate of the Merrimack river plume.

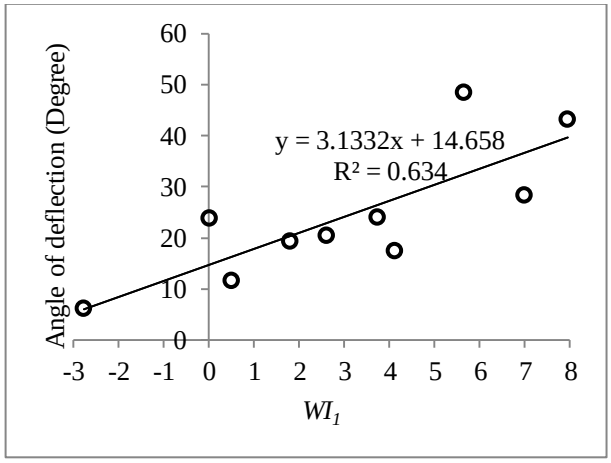


**Figure 6.4: Deflection angle of the plume with respect to normalized long-shore wind speed**

A major part of the mixing process occurs in the near-field of an outfall due to the turbulence generated by the momentum difference between the discharge flow and the ambient water, which is also known as jet-like mixing (Jirka, 2004). The dominance of the turbulence mixing process depends on the discharge densimetric Froude number ($Fr_0$) which represents the ratio of the discharge momentum to the buoyancy flux. Using the surface temperature fields shown in Fig. 6.2, the minimum dilution ($Sc=1-\Delta T/\Delta T_0$) at the

end of the near-field was calculated for each case where $\Delta T$ and $\Delta T_0$ are respectively the temperature differences between the plume axis and the ambient water ($T_a$) at the end of the near-field ($T$) and at the outfall location ($T_0$). Fig. 6.5 presents the variation of the minimum dilution at the end of the near-field with respect to $F_0$. As expected, a positive correlation was observed between $Sc$ and $F_0$, which demonstrates that higher discharge velocity resulted in higher dilution by the end of the near-field. This confirms the enhancing effect of increased discharge velocity on jet-like mixing rate in the near-field.

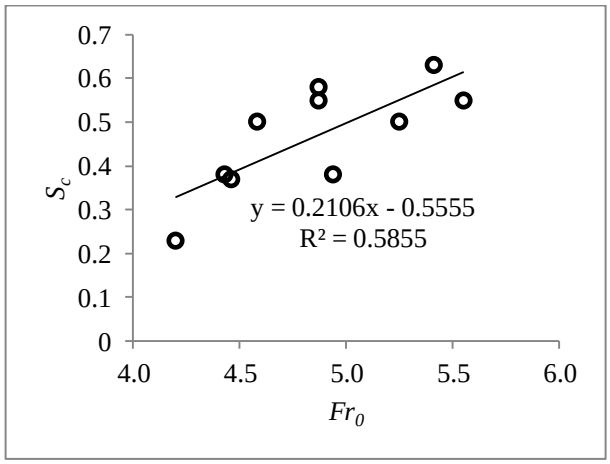


**Figure 6.5: Minimum dilution ($S_c$) at the end of the near-field with respect to the discharge densimetric Froude number ($Fr_0$)**

The initial momentum dissipates gradually with distance from the outfall while the wind stress and buoyancy forces become more significant. As previously mentioned, Wang et al. (2015) found that the wind influence is also essential in producing turbulence in the near-field of Merrimack River plume. In order to investigate the wind effect on the near-field mixing process, in this study $WI_2 = U_{wc}/U_0$ was defined as the ratio of the cross-shore wind ($U_{wc}$) to the discharge velocity. Variation of Sc with $WI_1$ and $WI_2$ is shown in Fig. 6.6.

a) b)

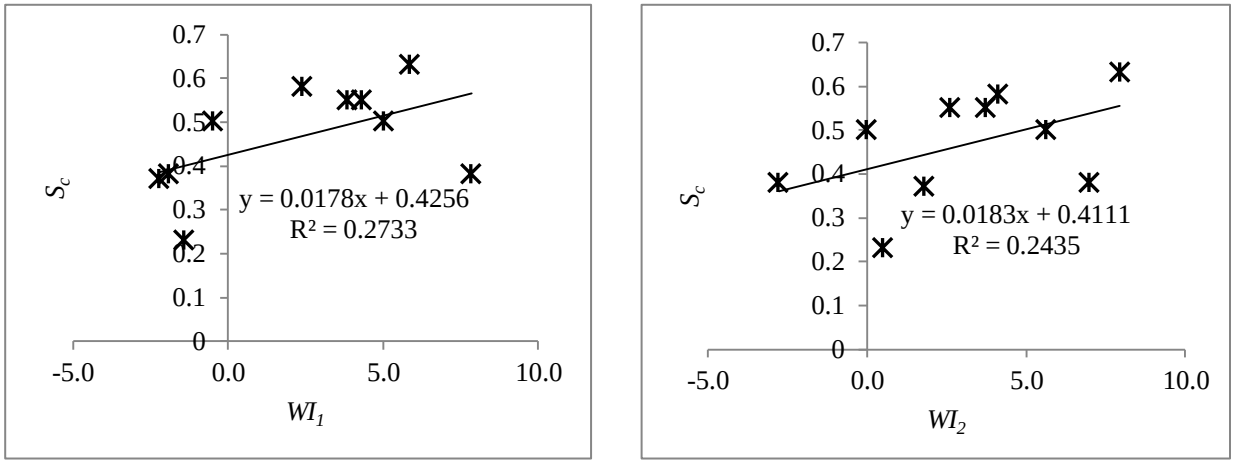


**Figure 6.6: Minimum dilution ($S_c$) at the end of the near-field with respect to a) the long-shore ($WI_1 = U_{wl}/U_0$ ) and b) cross-shore wind conditions ($WI_2 = U_{wc}/U_0$)**

Positive $WI_1$ and $WI_2$ respectively correspond to long-shore wind which deflects the plume from the confining jetty and shore to sea (onshore) wind conditions. The minimum dilution was weakened in the negative $WI_1$ and $WI_2$ wind conditions. This could be attributed to the fact that the onshore wind was directly opposite the discharge direction in this case and dissipated the initial momentum difference between the discharge and the ambient water, consequently weakening the mixing process. The shore to sea (offshore) wind condition enhanced the mixing process in the near-field of the plume. Considering the similar discharge rate for the May 15 and June 13 cases, it can be concluded the offshore wind condition could increase the minimum dilution by 20% by the end of the near-field. As previously mentioned Wang et al (2015) reported a higher TKE production in the onshore wind condition for the Merrimack River plume. Therefore, it was expected to observe a higher dilution rate for the onshore wind condition. However, in this study it was observed that onshore wind decreased the minimum dilution rate by the end of the near-field..

In order to investigate the effect of wind on the far-field plume dynamics, the modified Richardson number ($Ri^*$) was also provided for each investigated case in Table (6.1). In most of the cases in Fig. 6.2 $Ri^* < 5.5*10^3$ and shore line attachment is expected according to the proposed criteria by Nekouee et al.

(2013) (see Fig. 2.3 ). Comparing the observed results in Fig. 6.2, it can be seen that the plume differs from the behaviour predicted by the proposed criteria in most cases. This could be attributed to the fact that the Nekouee et al. method was developed based on a case where the river plume has detached from the bed close to the river mouth. The dissipating effect of bed shear in shallow water in the present case was not considered in the Nekouee et al's study.

## 6.7 Conclusion

The wind influence on the near-field dynamics of a coastal plume was investigated using a combination of remote sensing and numerical modelling approaches. The thermal images of Ras Laffan Industrial City (RLIC) surface thermal effluent were provided from LandSat7 thermal infrared (TIR) imageries between 2013 and 2014. The measured wind, water level and discharge condition were also used to determine the effective mixing sources. The thermal images showed that the wind effect was significant in the near-field dynamics of the plume. Numerical simulation was also conducted to validate that wind forcing has greater influence than tidal currents on near-field plume dynamics. Non-dimensionalized long-shore and cross-shore wind speed parameters were introduced in order to quantify the interaction of wind and discharge flow. The plume trajectory was found to be sensitive to the long-shore wind speed > 2 m/s which is about half of the reported value in a previous study. The lower effective wind speed was attributed to the shallow water discharge condition and lowre discharge rate in the current study. The shallow discharge condition resulted in faster dissipation of the initial discharge momentum and moved the intermidiate-field closer the outfall. Offshore wind was also found to have an enhancing effect on the mixing process. A previously reported classification scheme for predicting the general plume behavior under wind action was evaulated using the remotely sensed thermal plumes. The previous classifying method did not successfully predict the present shallow water plume behavior. This illustrates the importance of bed shear on plume dynamics and could be a good basis for future research.

# Chapter 7:

## Numerical modelling of mixing of the Ras-Laffan desalination plant outfall in Qatar coastal waters

**In consideration for submission to Environmental Modelling and Software**

**Authors**: Abolghasem Pilechi, Majid Mohammadian, Colin D. Rennie, Hazim Qiblawey

### 7.1 Abstract

In this study a nested coupled hydrodynamic-wave approach has been introduced to model the mixing pattern of thermal plumes in coastal waters. The model performance was verified using field measured and remotely sensed data of the Ras Laffan Industrial City thermal effluent plume in Qatar coastal waters. The method was found to be an efficient approach for practical applications which can be used in designing coastal outfalls as well as for environmental impact assessment purposes. Various factors were investigated in this study, including the effect of lateral confinement, wave interaction with the ambient flow, wave dissipation factors and different turbulence models. The lateral confinement was observed to weaken the minimum dilution rate by 50% at the end of the near-field. The white capping process was also found more significant on the mixing process among the other investigated wave dissipation factors.

### 7.2 Introduction

The discharge of effluents into water bodies from industrial plants or agricultural developments is an important subject in environmental and water resources engineering. Understanding the impact of these effluents on the water body and the way they are transported and mixed is necessary for developing environmentally suitable outfall systems. Variation of the centreline concentration of the effluent along its trajectory and the width of the plume are two primary parameters that are generally used to investigate the amount of dilution in mixing studies. Employing numerical models to investigate river and industrial

plumes in coastal regions is a popular approach in coastal mixing studies. These models generally couple a hydrodynamic and a wave model to consider the effect of wave-current interaction in the mixing process. The calculated velocity field can then be used for simulating mass transport in the computational domain. For example, Didier (2003) used the COHERENS model for simulating the near-field and far-field dispersion of brine from a desalination plant in Singapore under tidal action. Malcangio and Petrillo (2009) used MIKE3 in a mixing study of a brine effluent on the southern coasts of Italy. Some of these models are also able to be coupled with water quality models to simulate the interaction of different environmental parameters (e.g., $CO_2$ and ammonia). The ELCOM-CAEDYM model is one of these models, which have been used in several environmental impact studies of desalination plants (e.g., Okely et al., 2006; Harris et al., 2009).

Surface waves are the persistent environmental condition in coastal outfalls and are generally considered to enhance the dilution in coastal waters (Chin, 1987). Chin named this process as "spraying effect" which results in increasing the overall dilution by a factor of 2. The reduction of centerline velocity near the nozzle under wave action was also quantified by Koole and Swan (1994). The primary influence of the waves is significant shortening of the initial region described by a uniform "top hat" shaped velocity distribution, or the "zone of flow establishment" (e.g., Chin, 1987; Koole and Swan, 1994; Ryu et al., 2005). When the orbital velocities are in opposite direction to the jet flow, the jet becomes plume-like much closer to the source than in the absence of waves. This is due to the substantial increase of the turbulent components of the flow (Reynolds stresses) as a result of the interactions between incidental waves and the jet flow. Lin et al. (2012) reported an increase of approximately 30% in the average peak values of the Reynolds stress due to the wave action in their experimental study. In Lin et al.'s study, the wave was propagating in the opposite direction to the jet flow. The ambient flow was also assumed stagnant and the wave breaking influence on the mixing process was not considered.

Wave induced mixing is dependent on several factors: (1) relative water depth; (2) wave amplitude; (3) wave frequency; and (4) wave direction. The depth of the water column affected by the wave action is also related to the ratio of the water depth (h) to wavelength (L) (Sharp 1986). Chin (1987) reported a uniform profile for the orbital velocities of the water particles throughout the depth for h/L<0.05. For 0.05<h/L<0.5, the passing wave generated a non-uniform velocity profile throughout the depth with diminishing trend with depth that still had an influence at the sea floor. It was also found that for h/L>0.5 the wave has no influence on the ambient flow. Using the decay coefficient as the parameter that indicates how early the jet centreline begins to decay, Pope (2000) found a linear relationship between decay coefficient of a jet and the incident wave amplitude. However, the decay rate was found very close to the value in the stagnant ambient condition, thus the wave anplitude only weakly influenced decay rate. This implies the fact that the wave amplitude has no correlation with the decay rate of jet centerline velocity. In Koole and Swan's (1994) study also no significant change was observed in the decay rate under the wave action. However, the jet began to decay much earlier than in a stagnant ambient condition. Mori and Chang (2003) introduced the wave-to-momentum ratio ($R_M$) as the parameter for determining the influence of waves on the mixing process:

$$R_M = \frac{gA^2}{4b_0 u_0^{\,2}} \qquad \textbf{(7.1)}$$

In Eq.(1), A is the wave amplitude, $g$ is gravity, $b_0$ is jet radius and $u_0$ is jet velocity. They categorized the jet oscillations into three types of symmetric (I) or asymmetric (II) oscillations with a continuous jet center line as well as asymmetric oscillations with a discontinuous jet center line (III). They defined the mentioned types corresponding to $0.04< R_M <0.05$, $0.05< R_M <0.2$, and $R_M>0.2$ in their experiments. The study was conducted assuming a stagnant condition for the ambient flow. The dilution rate was not measured and only the free surface and the jet centreline movement were investigated. Furthermore, only short amplitude standing waves were used in this study and wave breaking effects were not considered.

Therefore, Mori and Chang noted that their proposed criteria for categorising the jet flow under wave action might not be the same for other geometric set up and wave conditions.

Chang et al. (2009) found that the $R_M$ ratio is essential in controlling the jet width in the self-similar region as well as the length of the ZFE of a jet. They proposed empirical equations for describing the decay coefficient and jet width in terms of the jet-to-wave momentum ratio. The precision of the developed relationships was validated in an experimental study by Hsiao et al. (2011). They found that the period or frequency of the wave plays a minor role in the mixing process compared to wave amplitude.

In coastal waters the offshore waves are diverted normal while propagating towards the shoreline due to refraction effects. This might be the reason that in most of the experimental wave mixing studies the jet direction is opposite to the wave propagation direction, i.e., 180° to the incident wave angle. However, this is not a practical assumption as offshore waves in different directions might also affect the mixing process in the far field of the jet where outfall momentum is dissipated. The orientation of wave propagation angle relative to the jet centerline is expected to influence the mixing characteristics. Sharp (1986) conducted an experimental study on the effects of discharge angle relative to the angle of wave propagation. No significant change was observed in mixing patterns when the discharge was parallel to the direction of waves, regardless of whether the jet flow was travelling in the same or the opposite direction of wave advancement. Chyan and Hwung (1993) studied the behavior of a vertically discharged jet towards the surface in a progressive wave environment. This situation is similar to a horizontal jet discharged perpendicular to the direction of waves. They observed a twin-peak in the concentration profile which was consistent with the "dumb-bell' effect described by Sharp (1986) and the twin-peak signature reported in Swan and Kwan's (1998) study. Xu et al. (2014) conducted an experimental study to investigate the effect of regular and random waves action of a vertical submerged jet. They also reported the twin-peak profile for the lateral profile of velocity under regular wave action which resulted in a lower axial velocity along the jet centreline in this case. The study was comprehensive with respect to

investigating various wave conditions and water depth. However, the incident wave was perpendicular to the jet axis and the ambient water was stagnant which might be different from the real condition in coastal waters.

Considering the effect of both waves and currents is important in optimal design of coastal and ocean outfalls. However, very little attention has been devoted to the unsteadiness or oscillatory flow produced by waves in a continuously moving ambient receiving body due to the difficulties in providing the experimental set up. Lam and Xia (2001) conducted a set of experiments to investigate jet dilution in an unsteady crossflow. They identified (1) jet-to-current velocity ratio, (2) unsteadiness parameter of the crossflow; and (3) the Strouhal number for defining the behavior of the jet. They reported that they generated large-scale effluent patches as a result of wave-flow interaction leading to an overall widening of jet and two to three times reduction of time-averaged concentrations. Coastal currents are the primary driving source of the mixing process in the intermediate and far field regions of coastal waters. The presence of the ambient flow could enhance or hinder the dilution (Roberts and Toms, 1987). These currents can be initiated due to wind, waves, tidal currents or Coriolis forces.

High computational cost has always been one of the main concerns for using numerical approaches in mixing studies. Far-field mixing is commonly simulated using numerical approaches, and different numerical models have been introduced and used in the literature for modelling the far-field mixing, such as FLOW-3D (Stamou and Nikiforakis, 2013), ALGE (Blanton et al., 2009) , EFDC (Lee and Qian, 2003), THREETOX (Maderich et al., 2008), MIKE3-HD (Elhakeem et al., 2007), COHERENS (Hassanzadeh et al., 2011) and Delft3D-FLOW (Morelissen et al., 2013). The above mentioned studies are different with respect to the numerical model and the extent of the studied region. However, the common aspect of all these works is using the hydrodynamic models without considering the interaction of wave and the tidal unsteady ambient flow which was previously demonstrated to significantly enhance the dilution.

The temporal and spatial scales of the mixing process are orders of magnitude smaller in the near-field than in the far-field. Therefore, using a numerical model for modelling the near-field and far-field regions requires the use of a fine-scale grid size close to the outfall to be able to model small turbulent eddies in the near-field region. This will consequently impose higher computational costs on the model when both the near-field and far-field are modelled at the same time. Due to lack of computational resources, even the most comprehensive studies have been conducted on two levels, where the near-field dilution and far-field dispersion of the brine have been modeled separately. Employing an appropriate approach to model the near-field and far-field mixing of effluents is one of the most challenging issues in mixing studies. The near-field mixing models can be categorized as jet integral models, CFD models and length scale models (Jones et al., 1996). Jet integral models are based on solving the ordinary differential equations and are derived by integrating jet properties like momentum, buoyancy and mass fluxes across a section (Jirka et al., 1981). The length scale models are based on the empirical expression of plume parameters and are derived from laboratory studies (Roberts et al., 1989a, 1989b, 1989c). Vaselali et al. (2009) used Mike21 for the far-field modelling and CORMIX3 in the near-field modelling of brine effluent mixing under tidal flow in the Persian Gulf. Alameddine and El-Fadel (2007) is another example of using the CORMIX3 model for simulating a thermal effluent of a desalination/power plant. RPS Consulting Engineers (2008) used the US EPA Visual Plumes program to model the initial dilution of brine from a desalination plant in Dublin, Ireland, and they used Mike21 to model the medium/far-field fate of the plume. Bleninger and Jirka (2010) developed a coupled CORMIX-Delft3D model for mixing studies that imports the output of CORMIX in the near-field as boundary for the Delft3D model in the far-field in each time step.

CFD models mostly solve Reynolds Averaged Navier Stoke Equation (RANS) (Versteeg and Malalasekara 2007) equations. In order to reduce the computational cost, hydrostatic pressure assumption is applied to the Navier Stokes equations for hydrodynamic modelling applications. In hydrostatic models, the total pressure is computed as a result of the hydrostatic pressure generated by the water surface elevation. In order to reduce the computational cost in large scale mixing studies, one

approach can be using hydrostatic models in both the near field and far field. This is the main motivation of using non-hydrostatic models, especially in the case of non-stratified ambient flows with a short near-field region and a mild slope bathymetry condition. Zijl (2002) investigated the effect of a non-hydrostatic model on simulating the near-field mixing of buoyant jets. A buoyant jet generated from a power plant was modelled using Delft3D (hydrostatic) and CFX (non-hydrostatic) models. A good agreement was observed between the hydrostatic and the non-hydrostatic models' results, especially in the far field.

Water level and wave height information are the primary boundary conditions in hydrodynamic/wave models. Tidal currents can be generated in a hydrodynamic model by applying the measured tidal water level as a boundary condition. However, the measured water level may not always be available for the region of interest. Therefore, oceanographic buoys need to be installed at the boundaries of the modelling region to provide the boundary data for the model. This solution may not be always applicable due to high cost and difficulties in access. This is the main motivation of this study: to introduce a nested modelling technique for the study of coastal mixing. In this study we show that the proposed method can be confidently used in designing coastal outfalls as well as in environmental impact assessment studies.

In this study, an efficient nested approach is introduced and applied in order to study mixing processes in coastal waters. In this method, the computational domain starts from the highest-level model (largest grid size) at the location of the available measured data. The measured water level data will be used as a boundary condition in the largest-scale model, and the boundaries of the other levels will be imported from the output of the next-higher level. The open source Delft3D Wave/Flow model, which is widely used in river and coastal hydrodynamics modelling, is used for generating the velocity field.The model is basically a hydrostatic model that solves the shallow-water equations. For the cases in which the vertical acceleration component is relatively small, the hydrostatics assumption for pressure distribution in the vertical direction is reasonable, and hence the hydrodynamic pressure can be ignored. The detailed discussion on the wave model can be found in (Deltares 2008; and Ris 1997). The model will be used to model the mixing pattern of the effluent of Ras Laffan Industrial City in Qatar. The numerical model will be validated using the field-measured temperature data from Chapter five. Ras Laffan Industrial City is

one of the biggest industrial compounds in Qatar, located on the eastern coast of Qatar, and discharges 222$m^3$/s of effluent into the Gulf through a surface outfall (Fig.7.1).

This chapter is organised as follows: In Section 7.2, the employed numerical model is explained, and results and discussions are presented in Section 7.3. Some concluding remarks in Section 7.4 complete the study.

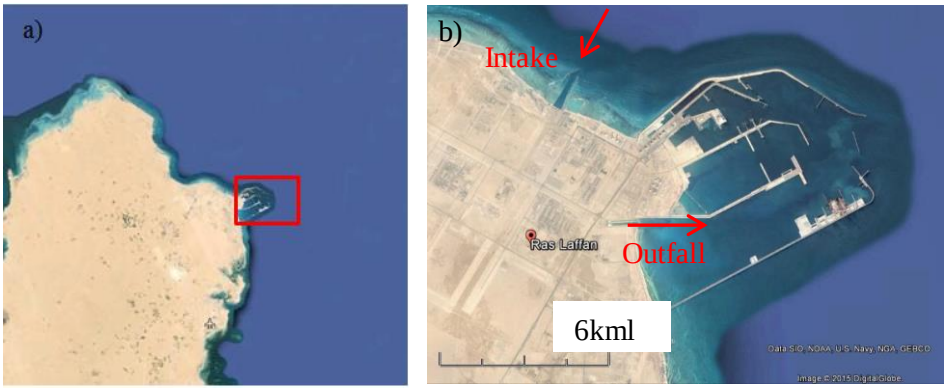


**Figure 7.1: a) Location of the Ras Laffan desalination plant on the eastern coast of Qatar; b) Ras Laffan intake and outfall, adapted from Google Earth**

## 7.3 Model set up

A nested approach is introduced and applied in this project for investigating the mixing pattern of thermal effluent from RLIC surface outfall (Fig. 7.1). The detailed information about the thermal effluent and the outfall system can be found inChapter five. A Delft3D flow/wave model is set up and run for the April 2013, Jun 2013 and May 2014 tidal and wave condition. The model consists of four levels with different grid sizes. Each lower-level model is nested in an encompassing higher-level model from which it obtains its boundary conditions for water level and waves.

The largest model (Level 1) is a 2D model which starts from the Strait of Hormuz and covers the entire Persian Gulf using a Cartesian structured grid with a 3km resolution (Fig. 7.2). The water level

boundary condition was obtained for the flow model from IHO buoy data from Farur Island, Lengeh Port and Ghanada Estuary stations (Fig.7.2). The wind data was also imported into the wave model to generate waves. The ETOPO2 bathymetry data with 1min resolution were downloaded from http://www.ngdc.noaa.gov/mgg/fliers/01mgg04.html. The model results were verified using IHO buoy data from Halul and UMM-Said (Fig. 7.3). Models Level 2 and 3 are also two-dimensional, and take their wave and water level boundary conditions from their neighbouring higher-level models.

The intermediate-level model (Level 2) is nested in model Level 1 and covers Qatar's eastern coasts with 500m grids (Fig. 7.4). The extent of model Level 3 is 10km*10km and surrounds the Ras Laffan port with 100m resolution grids (Fig. 7.4). The simulation results from models Level 2 and 3 were verified using the IHO buoy data for Jabal Al Fuwayrit and Al Wakrah stations, respectively (Fig. 7.5). Model Level 4 is a three-dimensional model and covers the entire Ras Laffan port and the outfall basin (Fig. 7.4b). The minimum grid size in this model is 20m in both the x and y directions at the outfall, and increases gradually with distance from the outfall. The model has ten sigma layers in the vertical direction.

The models were run for 1 year as a warm-up period. The time step for simulation in models Level 1 and 2 was 2 minutes. Due to the finer grid size in the lower level models, a time step size of 0.2 min was used in models Level 3 and 4. The sub-grid scale turbulence model (Van Vossen 2000) was used as a turbulence model in the 2D models (Levels 1, 2 and 3). The sub-grid scale and the $k$-$\varepsilon$ turbulence models were used in the Level 4 model. The total eddy viscosity in the model is the summation of a user-defined background eddy viscosity in the horizontal and the vertical directions and the calculated value by the turbulence models. The set up was conducted using the typical values for the background eddy viscosities. The details of the mentioned turbulence model can be found in the Delft3D user manual.

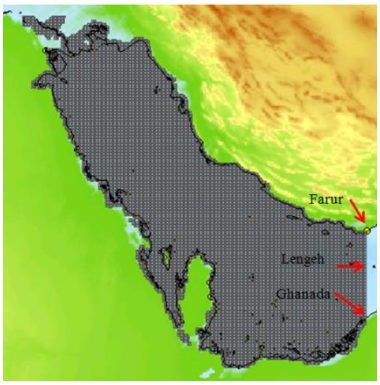


**Figure 7.2: The extent of model Level 1 and the location of the available IAHR tidal buoys**

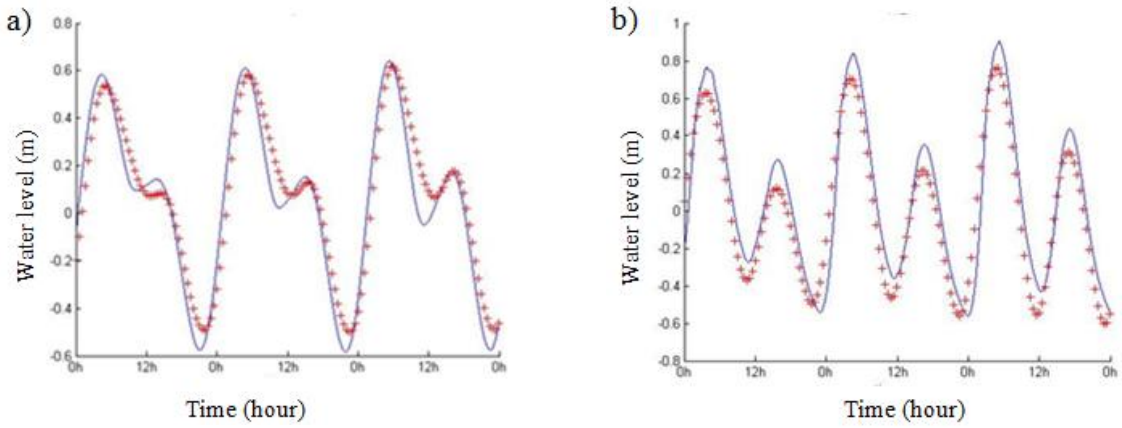


**Figure 7.3: Results of the numerical model (continuous line) and IHO gauge data from a) Halul and; b) UMM-Said stations**

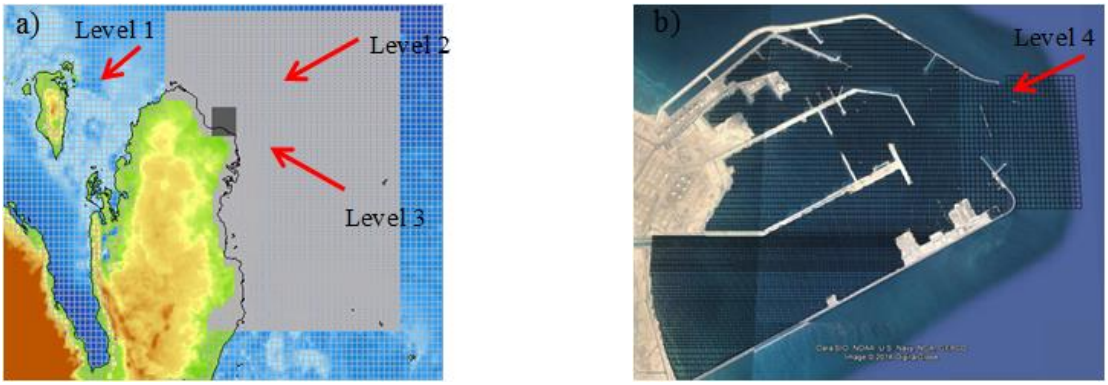


**Figure 7.4:Computational domain a) Level 1, Level 2 and Level 3; b) Level4**

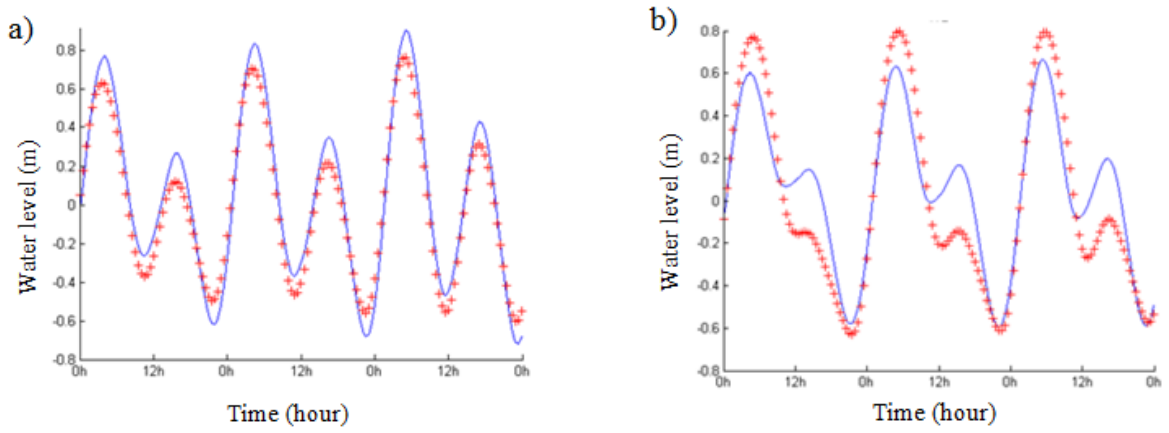


**Figure 7.5:Water level results of the numerical model (continuous line) and IHO gauge data from a) the Jabal Al Fuwayrit and; b) Al Wakrah stations**

Using the discharge information of RLIC outfall, the dispersion of the thermal effluent was simulated in model Level 4. The next section provides the detail of the simulation results.

## 7.4 Results

In this section, the model results for the temperature are presented and compared with the observed data from Chapter five. Figure 7.6 presents the modeled and measured spatial distribution of temperature on May 18, 2014.

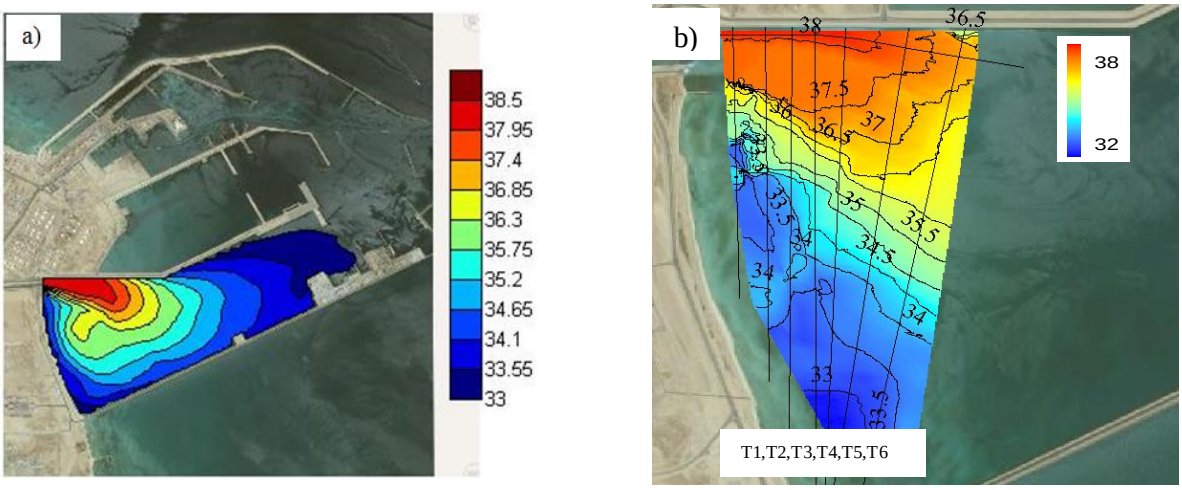


**Figure 7.6: Spatial distribution of temperature of RLIC effluent on May 18 from a) the model; b) the field survey, solid lines are data extraction lines in Fig.7.7**

Variation of the jet width and the maximum value along the jet trajectory for the parameter of interest (temperature in this project) are among the important factors in studying mixing processes. In order to investigate the performance of the numerical model, the lateral distribution of measured temperature was extracted on the defined lines in Fig. 7.6. The lines are located at different distances from the outfall and are oriented perpendicular to the jet axis. Figure 7.7 presents the lateral distribution of the temperature between 500m (a) to 1600m (f) from the outfall location.

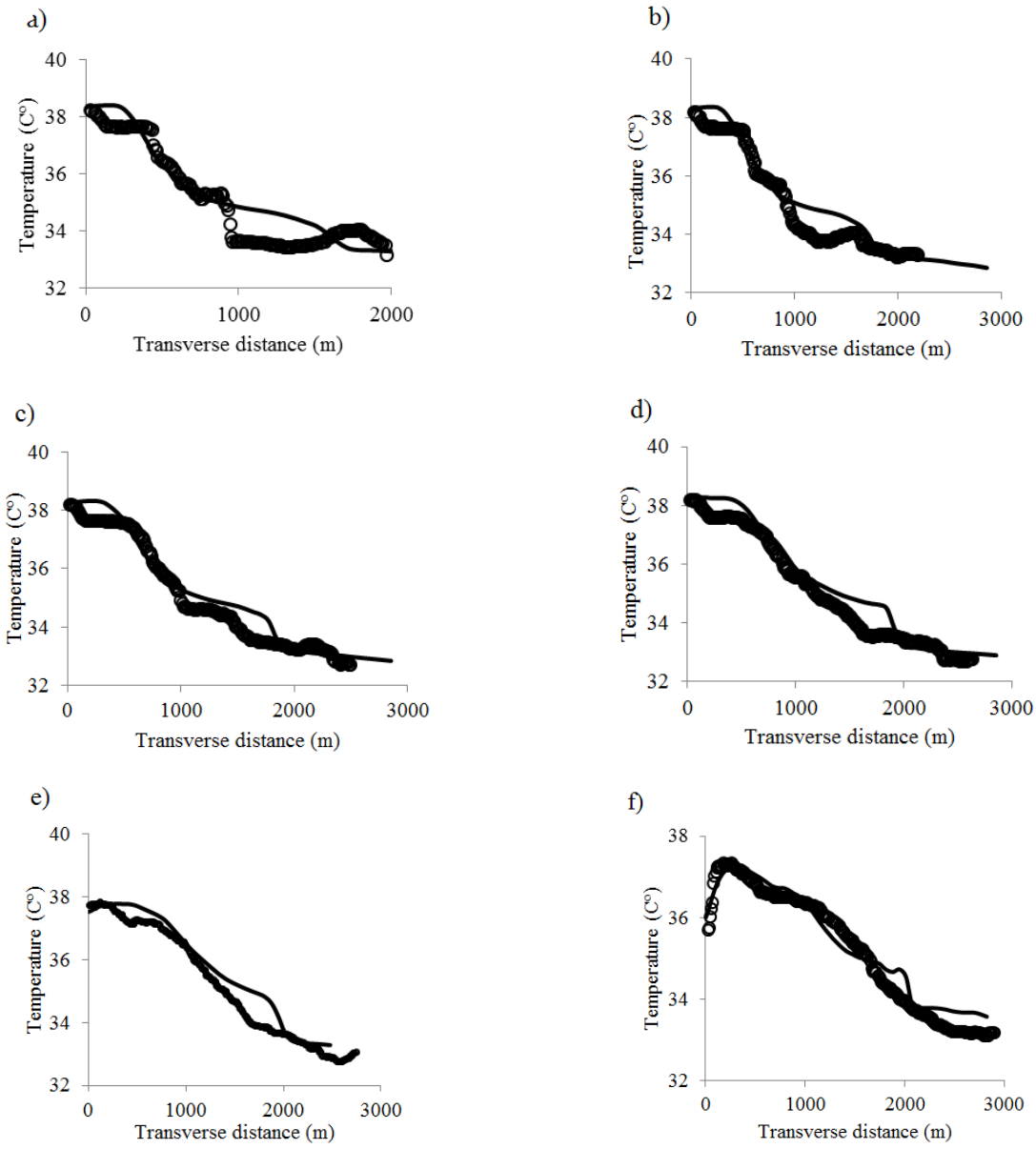


**Figure 7.7: Lateral distribution of temperature on the extraction lines T1 to T6 in Fig.7.6b, May 18 2014 (continuous line represents model results and the discrete points are data the measured data)**

Comparison of the estimated results and the measured data for temperature in Figures 7.6 and 7.7 shows that the introduced modelling approach is reasonably successful in predicting the measured temperature data. The model is also successful in predicting the detachment point from the left wall (observed in the field data). In order to examine the model performance in predicting the vertical mixing processes, the measured vertical profile of temperature at different locations of the plume (Fig. 7.8) were compared with

the model output in Fig. 7.9. The model performs better closer to the outfall in the shallower region (stations S3 and S5) and underestimates the vertical mixing. However the overall error in estimation of the depth averaged temperature is reasonable considering the large extent of the computational domain and temporal turbulent fluctuations within the measurement period.


**Figure 7.8: Location of the vertical profile measurement, May 17 2014**

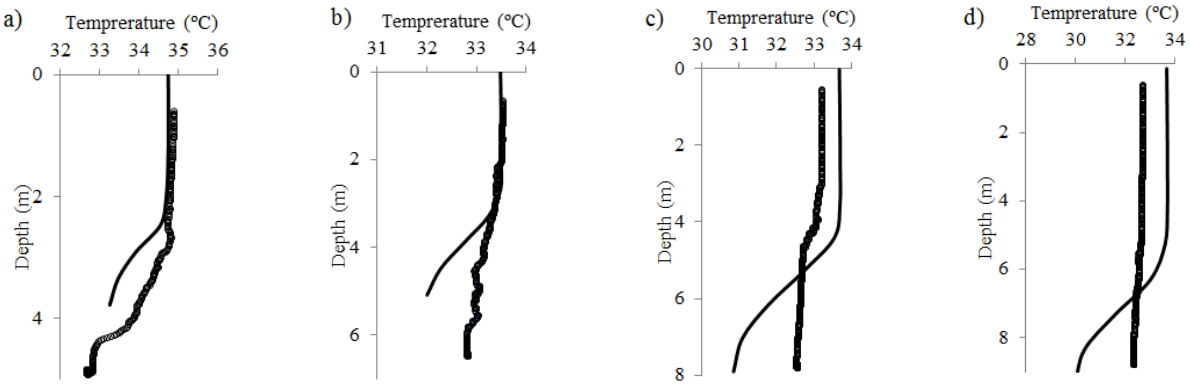


**Figure 7.9: Vertical profiles of temperature, May 17, 2014 for a) S3, b) S5, c) S7 and d) S9 (continuous line represents model results and the discrete points show the measured data)**

In order to further examine the performance of the proposed nested approach, a comparison was also made with the data obtained from remote sensing data for June 13th, 2013 (see Chapter five for

methodology details). As observed in Figure 7.10, the model is again able to estimate the general form of the spatial distribution of the outfall temperature with a reasonable accuracy.

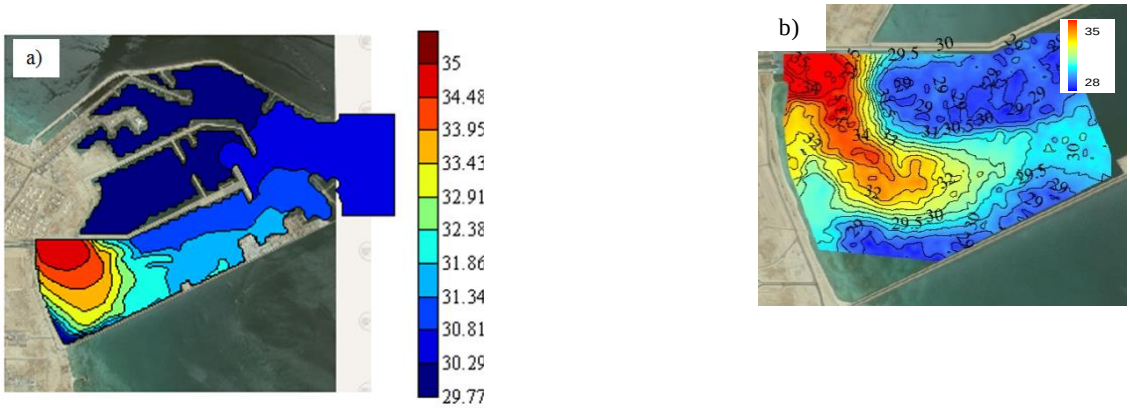


**Figure 7.10: Temperature contours for May 15, 2014 from a) model and; b) measured data**

## 7.5 Discussion

We begin with the effect of horizontal and vertical eddy viscosity. The total eddy viscosity in the model is the summation of the background eddy viscosity and the eddy viscosity calculated from turbulence models. In order to investigate the effect of the background horizontal and vertical eddy viscosity on the mixing process, the simulation results were compared for a range of background eddy viscosity values. The best fit to the measured data was found for the background horizontal eddy viscosity of 0.1 $m^2/s$ and the background vertical eddy viscosity of 0.0001 $m^2/s$. The resulting maximum obtained values for the total horizontal and total vertical eddy viscosities of the system were 2 $m^2/s$ and 0.0015 $m^2/s$, respectively. The horizontal eddy viscosity decreases with distance from the outfall due to the dissipation of the outfall momentum lowering kinetic turbulent energy (TKE). However, the vertical eddy viscosity increases with depth along the jet trajectory. This is attributed to the low bed roughness thus low bed shear velocity (velocity scale). Furthermore, the shallow initial depth confines the vertical eddy sizes (length scale) and restricts entrainment processes (and shear).

The performance of the employed turbulence model is analysed in the following. The turbulence models include *k-ε*, *k-l* and Algebraic stress schemes. As shown in Fig. 7.11, compared to the measured data from May15 and May18, 2014 field surveys, the *k-ε* model leads to better results than the two other models in estimating the dilution rate. Moreover, the length of zone of flow establishment and the plume width were also better estimated using the k-ε model (not shown). The estimated minimum dilution by the Algebraic stress turbulence model is about 50% lower than the observed and the estimated values by the k-ε model at the end of the near field region. The Algebraic stress model also overestimated the length of the zone of flow establishment by about 75% and the plume width by 65%. The *k-l* model showed better performance than the Algebraic model in predicting the minimum dilution rate. The estimated plume width by the *k-l* model is up to 90% greater than the *k-ε* predicted value. Buoyancy is an important parameter in TKE production in mixing processes which accompany density difference. The effect of this term on the mixing process is investigated in appendix A using the Standard Gradient Diffusion Hypothesis (SGDH) and the General Gradient Diffusion Hypothesis (GGDH) methods.

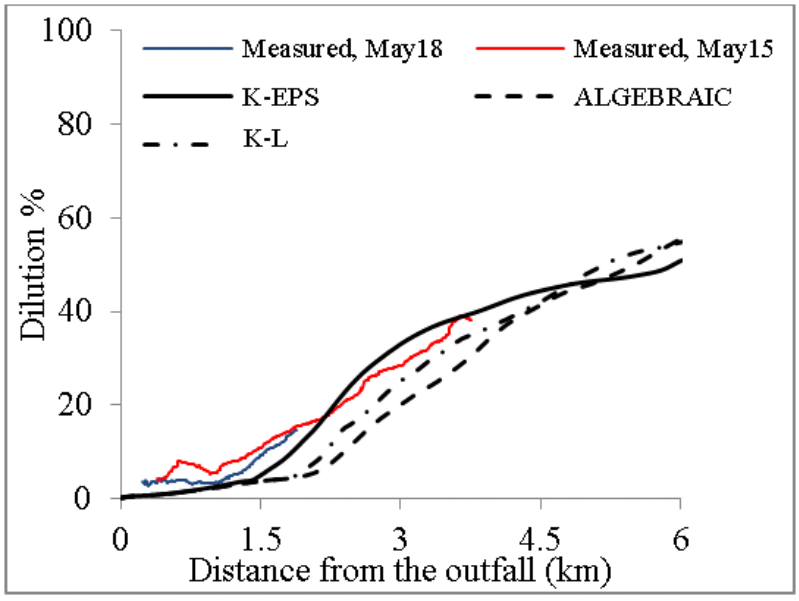


**Figure 7.11: Result of different turbulence models for predicting the variation of the minimum dilution along the jet trajectory**

The effect of confinement on the mixing process was also investigated in this study. The model results for the minimum dilution in two defined scenarios of one-side confinement (Cf1) and non-confined (Cf0) outfalls were compared with the two-side confinement (Cf2) case (current condition). Comparing the dilution with respect to the distance from the outfall, it was observed that locating the outfall inside the port (two-side confinement) has decreased the diluting potential of the outfall by 50% at the end of the near field mixing zone (not shown). It was also observed that although the minimum dilution at 3km (end of the near field, as discussed in Chapter five) was approximately the same in the no-confinement and one-side confinement cases, the minimum dilution at 1.5km from the outfall (end of the jet-like mixing zone) was about half of the minimum dilution in the no-confinement case. This could be attributed to the wall effect, which has restricted the entrainment of the ambient water into the jet leading to reduction of dilution rate in the near field region. The weakening effect of side confinement on the average dilution has also been observed and quantified in Chapter five.

The effect of the wave action on the minimum dilution was also investigated in this study. It was observed that waves weakened the minimum dilution by the end of the near field zone. This observation differs from the outcomes of some previous studies, which found that wave action enhanced the dilution by reducing the zone of flow establishment length (Koole and Swan, 1994). However, in this study, the minimum dilution increased in the far field region under wave action. This can be explained as a result of wave momentum that enhanced the mixing process at end of the near field. Indeed, in the near field zone, the wave momentum is small compared to the jet momentum and is thus ineffective, while in the far field, it becomes dominant and effective due to the dissipation of the outfall momentum. It was observed that waves with height $Hs>0.1$ m had a clear effect on the minimum dilution at the end of the near field region(not shown). The simulation results showed that the significant wave height in the studied region was less than 2 m. It was observed that when the wave was in the same direction as jet flow, it weakened the mixing process and when it was in the opposite direction it enhanced the dilution rate.

As previously mentioned, the wave simulation includes the wave energy dissipation due to the whitecapping, bottom friction effect and depth-induced breaking, all of which can influence the mixing process. The whitecapping was observed to enhance the mixing by 5 % when the wind was perpendicular or in the opposite direction to the jet flow. This factor was also found to be more effective than the wave-breaking factor in the mixing process. Finally, a sensitivity analysis of the mixing process with respect to the bottom friction factor was conducted in this study. The bottom friction value did not affect the mixing factor in the zone of flow establishment. Indeed, increasing bottom friction factor over a wide practical range only enhanced the mixing rate by 5% at the end of the near field region.

## 7.6 Conclusion

In this study, a nested approach was introduced for modelling the mixing process in coastal waters. The method was implemented in a four-level hydrodynamic/wave model to simulate the mixing pattern of the thermal effluent of Ras Laffan Industrial City in Qatar coasts. The nested model consisted of 2D models (Levels 1, 2, and 3) and a local three-dimensional model (Level 4) in the finest scale. In this approach, the simulated water level and waves in each level of the model were used as boundary conditions for the nearest lower-level model. Levels 1, 2 and 3 of the model were validated using IHO water level buoy data. The effluent dispersion process was modelled in the lowest-level model (Level 4). The mixing model was validated using the measured temperature data from field survey and thermal imagery provided from LandSat7 TIR imagery in Chapter five.

The model was also used to investigate the influence of confinement and wave-flow interaction on the mixing process. The simulation results showed that side confinement of the surface outfall reduced the minimum dilution rate up to 50% by the end of the near field zone. The mixing process was also investigated under wave action. The vertical profile of the temperature did not change significantly when waves were considered. However, the minimum dilution was enhanced by 10% at the end of near field due to the wave interaction with the ambient flow. From different parameters that incorporate

dissipation of the wave energy in the wave model, the whitecapping factor was found significant on the mixing process.

One of the challenges in designing surface outfalls and conducting environmental mixing studies in coastal waters is the high cost of field studies and lack of measured data to be used as input data for calibration and validation purposes in the numerical models. The proposed approach facilitates this task by providing an efficient method which can be used in design applications and environmental impact assessment projects, relying only on widely available oceanographic data. The numerical approach of the current study is also more comprehensive than previous studies due to considering the effect of wave-current interaction in the mixing process. Most, if not all, available mixing studies that consider the effect of both wave and flow on the mixing process are primarily experimental, and these are rare due to the difficulties in setting up the experiments. Another contribution of this work is the validation of the proposed approach based on the field measured data - which has the influence of all important environmental factors in a coastal climate such as unsteady ambient flow, wave and wind – in a parametric sensitivity analysis. The study investigates and shows the contribution of different effective parameters on the mixing. All of the above mentioned features make the proposed method in the current study a useful approach in practical applications of coastal mixing studies.

**Acknowledgements**

This publication was made possible by NPRP grant # 4-935-2-354 from the Qatar National Research Fund (a member of the Qatar Foundation). The statements made herein are solely the responsibility of the authors. The authors also thank the QNRF authority, Ras Laffan Industrial City (RLIC) administrative authority and the Qatar Ministry of Environment for their support in this project.

**Appendix A**

The dispersion process is modeled by turbulence model in hydrodyamic models. Different turbulence models have been developed on the basis of RANS equations. The k-ε turbulence model is one of the most common turbulence models due to its simplicity, computational efficiency and stability (Rodi 1980). The standard k-ε is a two equations turbulence model. The transport equations for k and ε are written as,

$$\frac{\partial k}{\partial t}+U_i\frac{\partial k}{\partial x_i}=\frac{\partial}{\partial x_i}\left(\frac{\partial \nu_t}{\sigma_k}\frac{\partial k}{x_i}\right)+P+G+\varepsilon \qquad \textbf{(7.a.1)}$$

$$\frac{\partial \varepsilon}{\partial t}+U_i\frac{\partial \varepsilon}{\partial x_i}=C_{1\varepsilon}\frac{\varepsilon}{k}(P+G)(1+C_{3\varepsilon}R_f)-C_{2\varepsilon}-\frac{\varepsilon^2}{k} \qquad \textbf{(7.a.2)}$$

where k is the turbulent kinetic energy and ε is the turbulence dissipation rate. The parameters P and G represent the source/sink term due to the shear and buoyancy respectively. The eddy viscosity is denoted as $\upsilon_t$. Applying the Bissinesq approximations, the shear induced source/sink term (P) is written as,

$$P=-\overline{u_i'u_j'}\left(\frac{U_i}{x_j}\right)=\nu_t\left(\frac{U_i}{x_j}+\frac{U_j}{x_i}\right)\frac{U_i}{x_j} \qquad \textbf{(7.a.3)}$$

where $U_i$ and $u'_i$ are respectively the time averaged velocity and the fluctuations in $x_i$ direction.The effect of buoyancy on production and dissipation of turbulent kinetic energy is essential in the cases which include density difference such as buoyant plumes dispersion. There are different methods for applying the buoyancy source/sink term in the k-ε turbulence model. The Standard Boussinesq Gradient Diffusion hypothesis (SGDH) (deffault method in Delft3D) is one of the popular methods which has been widely used in previous studies such as Rodi (1980) and Markatos et al. (1983). This model only consideres the vertical gradient of density in calculating the buoyancy production term. The buoyancy source term in SGDH method is defined as,

$$G = -\frac{\nu_t}{\sigma_t}\left(\frac{\partial \rho}{\partial x_j}\right) g_j \qquad \textbf{(7.a.4)}$$

$g_j$ is acceleration in $x_i$ direction. Different value has been used in the literature for the $\sigma_\varepsilon\ C_{1\varepsilon}\ C_{2\varepsilon}\ C_{3\varepsilon}$ are emperical constants.

$R_i$ is the flux Richardon number which is the ration of turbulence production/distruction due to the buoyancy to the one due to the shear velocity,

$$Ri = \frac{g}{\rho}\frac{\partial \rho / \partial z}{(\partial u / \partial z)^2} \qquad \textbf{(7.a.5)}$$

where $u$ and $v$ are horizontal and vertical components of velocity, $\upsilon_t$ is eddy viscosity, $\rho$ is density and g is the gravity. The ratio of eddy eddy viscosity to eddy diffusivity is defined as the Prantle-Schmit number. This parameter appears in the denominator of both shear and buoyancy induces source terms in the k and the ε equations and we assumed $\sigma_t$=0.85 in this study.

The General Gradient Diffusion Hypothesis (GGDH) by Daly and Harlow (1970) is another method which is more complex than the SGDH and considers the shear stress in calculating the buoyancy source term in the k-ε model. The buoyancy source term in GGDH method is defined as

$$G = -\frac{3}{2}\left(\overline{u'_j u'_k}\frac{\partial \rho}{\partial x_k}\right) g_j \qquad \textbf{(7.a.6)}$$

The buoyancy modified $k$-$\varepsilon$ model has been previously examined in different studies. In one of the most comprehensive studies, Van Maele and Merci (2006) studied the effect of buoyancy term of the turbulence model in a numerical simulationg of fire-induced flow. They studied the influence of both simple and the generalized hypothesis in standard and realizable k-ε turbulence models. The efficiency of GGDH hypotheis in modelling the turbulance thermal plumes has also been confirmed in some other studies. Yan and Holmstedt (1999) and Worthy et al. (2001) in their studies on thermal plumes found that

generalized diffusion hypothesis gives more realistic results. In this study the Delft3D *k-ε* turbulence model was modified by adding the buoyancy term using the General Gradient Diffusion Hypothesis (GGDH). Figure 7.A.1 presentes simulation results for tempreture field on May 18 using SGDH and GGDH methods.

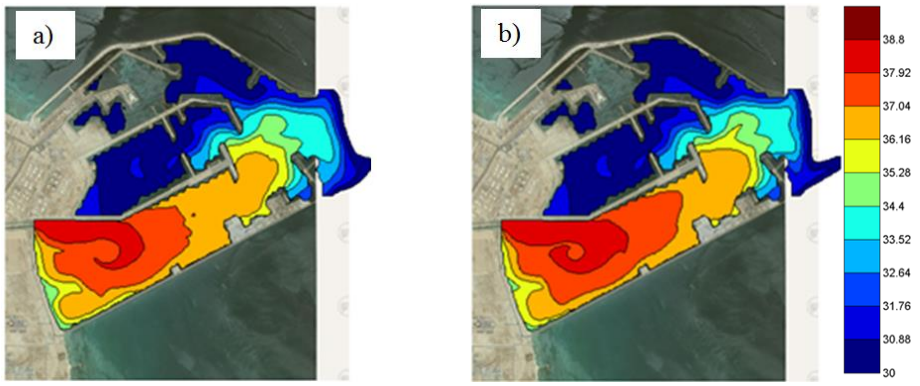


**Figure 7.12.a1: Temperature contours for May 15, 2014 a) GGDH; b) SGDH**

It can be seen that the use of different buoyancy induced turbulent production terms in the *k-ε* did not show significant difference on the simulation results. This could be attributed to the low density difference between the plume and the ambient water in this case which has resulted in negligible contribution for the buoyancy induced turbulence in the mixing process.

.

# Chapter 8:

## Conclusion

This study aimed to improve the understanding of mixing processes using simple and reliable methods for monitoring and modelling the near field and the far field fate of neutral/buoyant effluents in rivers and coastal waters.

In this research a new *in situ* measurement technique was introduced for investigating the intermediate mixing pattern in meandering rivers. Rhodamine WT was injected as tracer at the outfall location and the mixing pattern was tracked by measuring the tracer concentration with an *in situ* fluorometer across the river section in various sub reaches along a 83 km reach of the North Saskatchewan River. The full transverse mixing length of 130 km was estimated downstream of the Capital Region WWTP outfall.

A coupled field-numerical method was also introduced for modelling the mixing pattern in meandering rivers. The method was used to develop a numerical model in an innovative stream tube orthogonal curvilinear coordinate system to estimate the transverse mixing in the North Saskatchewan River. The model was calibrated using the field measured data for an 83-km reach of the North Saskatchewan river. An average transverse mixing coefficient of 0.037 $m^2/s$ was calculated for the surveyed reach.

The coastal mixing part of this research was conducted on the thermal effluent of Ras Laffan Industrial City (RLIC) in Qatar. An intensive field survey was conducted in the near-field and the far-field of the surface outfall. Using the measured temperature and hydrodynamic data, different characteristics of the surface buoyant jet such as dilution, thickness, detachment depth, etc. were investigated under a shallow water discharge condition. The entrainment coefficients of 0.67 $m^2/s$ and 0.78 $m^2/s$ were estimated for the jet mixing and the buoyant spreading processes, respectively. An innovative remote sensing technique was also introduced and used for obtaining the thermal images of the plume from LandSat thermal infrared (TIR) images.

As mentioned in the introduction section, tidal currents and wind are critical parameters in the coastal mixing process. Using the method proposed in Chapter 5, the thermal images of RLIC thermal effluent were generated from the available LandSat TIR images for the period January 2013 until May 2014. The images were used for investigating the effect of wind and tidal cycle on the dynamics of a surface thermal plume in Chapter 6 using a combination of remote sensing and numerical modelling approaches. Unlike previously reported studies, the wind effect was found significant on the trajectory and the mixing rate even in the near-field region of the plume. The plume trajectory was found affected by the long shore wind higher than 2 m/s. The near-field mixing rate was found to be enhanced up to 20% under the sea to shore wind condition. Two non-dimensional parameters were also proposed for quantifying the wind influence on the plume deflection and mixing rate.

A practical nested numerical approach was introduced and used in wave-flow model for simulating the RLIC plume in Chapter 7. A four-level model consisting of 2D models (Levels 1, 2, and 3) and a local three-dimensional model (Level 4) was set up using the measured water level, wind, temperature and discharge rate. The simulated water level and waves in each level of the model were used as boundary conditions for the nearest lower-level model. The model was validated using the field measured data presented in Chapter 5 and the thermal images obtained from remote sensing in Chapter 6. Different effective parameters on the mixing process including the confinement of the outfall, wave-current interaction and turbulence models were investigated. Lateral confinement was found to reduce the minimum dilution rate up to 50% by end of the near field. The minimum dilution was enhanced by 10% at the end of near field under the wave action. Whitecapping was found the most significant factor on the mixing process among different parameters that affect wave energy dissipation.

The conducted study sheds light on the RLIC environmental authorities' concern about the full dilution of effluent materials by the entrance of the port. The field measurements and remote-sensing data showed that the effluent reached the full dilution condition inside the port. The obtained calibrated model in this study can also be used in future investigation of the mixing process of any other effluent materials.

**Recommendations for Future Work:**

A field-numerical model can also be used in the coastal mixing part of the project using the similar concept as introduced in Chapter 4.2. The model solves the advection-diffusion equation in a stream-tube curvilinear coordinate system. In the first step the velocity field within the computational domain will be generated by solving the continuity equation in the near field control volume. The generated velocity field is calibrated using the aDcp measured data. The mixing process can be incorporated by the diffusion and sink terms in the advection-diffusion equation. The model can be calibrated using the field measured data such as salinity, temperature or tracer concentration.

## References


Abessi, O. Saeedi, M. Davidson, M., Hajizadeh Zaker, N. (2012). " Flow Classification of Negatively Buoyant Surface Discharge in an Ambient Current." Journal of Coastal Research, 28, Issue 1A: 148-155.

Abraham, G. (1973), "Jets and Plumes Issuing into Stratified Fluid. "International Symposium on Stratified Flows, Novosibirsk, 1972, Published by ASCE, 1973, pp. 4-31.2012.

Akar, P.J., Jirka, G.H. (1994). "Buoyant Spreading Processes in Pollutant Transport and Mixing. Part I: Lateral Spreading in Strong Ambient Current", J. of Hydraulic Research, Vol. 32, pp. 815-831.

Alameddine, I., El-Fadel, M., 2007, "Brine discharge from desalination plants: a modeling approach to an optimized outfall design", *Desalination* 214, 241–260.

Albers, C., Steffler, P. (2007). "Estimating Transverse Mixing in Open Channels due to Secondary Current-Induced Shear Dispersion." J. Hydraul. Eng., 133(2), 186–196.

Alberta Government (2014). "Terms of Reference for Developing the North Saskatchewan Regional Plan".https://landuse.alberta.ca/LandUse%20Documents/Terms%20of%20Reference%20for%20Developing%20the%20North%20Saskatchewan%20Region%20-%202014-05.pdf

Ali, J., Fieldhouse ,J., Talbot, C. (2011). "Numerical modelling of three-dimensional thermal surface discharges." Engineering Applications of Computational Fluid Mechanics Vol. 5, No. 2, pp. 201–209

Arita, M., Jirka, G. H.,Tamai, N. (1986). "Classification and mixing of two dimensional buoyant surface discharges." J. Hydr. Res., 24, 333-345.

Atkinson, J. (1993). "Detachment of Buoyant Surface Jets Discharged on Slope." J. Hydraul. Eng., 119(8), 878–894.

Baek, K., Seo, I.W, Jeong, J. J. (2006). "Evaluation of Dispersion Coefficients in Meandering Channels from Transient Tracer Tests." J. Hydraul. Eng., 132(10), 1021-1032.

Baek, K., Seo, I.W. (2008). "Prediction of Transverse Dispersion Coefficient Using Vertical Profile of Secondary Flow in Meandering Channels." KSCE Journal of Civil Engineering, 12(6), 417-426.

Baek, K.O., Seo, I.W. ( 2010). "Routing procedures for observed dispersion coefficients in two-dimensional river mixing." Advances in Water Resources, (33)12, 1551–1559.

Bansal, M.K. (1971). "Dispersion in natural streams." J Hydr Div ASCE, 97(11), 1867–1886.

Becker, M.W., Daw, A. (2005). "Influence of lake morphology and clarity on water surface temperature as measured by EOS ASTER". Remote Sensing of Environment 99, 288–294.

Beltaos, S. (1980). “Transverse mixing tests in natural streams.” J. Hydraul. Div., 106(10), 1607–1625.

Beltaos, S., Arora, V.K. (1988). “An explicit algorithm to simulate transient transverse mixing in rivers.” Canadian Journal of Civil Engineering 15, 964–976.

Blanton, J.O., Garrett, A.J., Bollinger, J.S., Hayes, D.W., Koffman, L.D., Amft, J., (2009). “Transport and Dispersion of a Conservative Tracer in Coastal Waters with Large Intertidal Areas.” *Estuaries and Coasts* 32, 573–592.

Bleninger, T., Jirka, G.H. 2004. “Near- and far-field model coupling methodology for wastewater discharges. In: J.H.W. Lee, K.M. Lam (eds.), Environmental Hydraulics and Sustainable Water Management, Proceedings of the 4th International Symposium on Environmental Hydraulics and 14th Congress of Asia and Pacific Division.” *International Association of Hydraulic Engineering and Research, Hong Kong, China, Taylor and Francis*, pp. 447-453.

Boxall, J. B., Guymer, I. (2003). “Analysis and prediction of transverse mixing coefficients in natural channels.” J. Hydraul. Eng., 129(2), 129–139.

Blanckaert, K. (2011). “Hydrodynamic processes in sharp meander bends and their morphological implications.” J. Geophys. Res. 116( F1), F01003, doi:10.1029/2010JF001806.

Blanckaert, K., De Vriend, H.J. (2003). “Nonlinear modelling of mean flow redistribution in curved open channels.” *Water Resour. Res.* 39(12), 1375, doi:10.1029/2003WR002068.

Boxall, J.B., Guymer, I. (2003). “Analysis and Prediction of Transverse Mixing Coefficients in Natural Channels.” *J. Hydraulic Eng.* 129(2), 129–139.

Boussinesq, J. (1871). “Théorie de l'intumescence liquide, applelée onde solitaire ou de translation, se propageant dans un canal rectangulaire.” *Comptes Rendus de l'Academie des Sciences*, 72, 755–759.

Carr, M.L., Rehmann, C.R. (2007). “Measuring the Dispersion Coefficient with Acoustic Doppler Current Profilers.” J. Hydraul. Eng., 133(8), 977–982.

Chang, K.-A., Ryu, Y., and Mori, N. (2009). “Parameterization of neutrally buoyant horizontal round jet in wave environment.” *J. Waterway, Port, Coastal, Ocean Eng.*, 135(3), 100–107.

Chander, G., Markham, B.L., Helder, D.L. (2009). “Summary of current radiometric calibration coefficients for Landsat MSS, TM, ETM+, and EO-1 ALI sensors.” Remote Sensing of Environment 113, 893–903.

Chin, D. A. (1987). “Influence of surface waves on outfall dilution.” J. Hydraul. Eng., 113(8), 1006–1018.

Chang, Y. C. (1971). “Lateral mixing in meandering channels.” PhD thesis, Univ. of Iowa, Iowa City, Iowa.

Chen, D., and Jirka, G. H. (1999). ‘‘LIF study of plane jet bounded in shallow water layer.’’ J. Hydraul. Eng., 125(8), 817–826.

Chin, D. and Roberts, P. (1985). ”Model of Dispersion in Coastal Waters.” J. Hydraul. Eng., 111(1), 12–28.

Chen F, MacDonald, D.G. (2006). “Role of mixing in the structure and evolution of a buoyant discharge plume. ” *J. Geophys. Res*. 111:C11002

Choi, B., and J. Wilkin (2007). “The effect of wind on the dispersal of the Hudson River plume. ” *J. Phys. Oceanogr*., 37(7), 1878–1897.

Chu, V. H., Jirka, G. H. (1986). “Buoyant surface jets and plumes in environmental fluid mechanics.” Encyclopaedia of fluid mechanics, N. Cheremisinoff, ed., Chap. 27, Gulf, Houston.

Cobb, N., Eernest D. (1972). “Transverse Diffusion of Solutes in Natural Streams.” Geological Survey Professional, C1–C19.

Constantinescu, G., Kashyap, S., Tokyay, T., Rennie, C.D., Townsend, R.D. (2013). “Hydrodynamic processes and sediment erosion mechanisms in an open channel bend of strong curvature with deformed bathymetry: Erosion mechanisms in a river bend.” *J. Geophys. Res.* 118(2), 480–496.

Cushman-Roisin, B., Beckers, J.M. (2011). "Introduction to Geophysical Fluid Dynamics." *Academic Press, Waltman*, p. 275

Daly B.J., Harlow, F.H. “Transport equations in turbulence.” *Phys Fluids* 1970;13:2634–49.

da Silva, J.F., Duck, R.W., Anderson, J.M., McManus, J., Monk, J.G.C. (2001). “Airborne observations of frontal systems in the inlet channel of the Ria de Aveiro, Portugal.” Physics and Chemistry of the Earth (B) 26:713–719.

Darby, S.E., Alabyan, A.M., Van De Weil, M.J. (2002). “Numerical simulation of bank erosion and channel migration in meandering rivers.” Water Resour. Res., 38:1163. DOI: 10.1029/2001WR000602.

Darwish, M.A., Mohtar, R. (2013). “Qatar water challenges.” Desalination and Water Treatment, Vol.51, Iss.1-3.

Davies, P.A., Mofor, L.A., Neves, M.J., (1997). “Comparisons of Remotely Sensed Observations with Modelling Predictions for the Behaviour of Wastewater Plumes from Coastal Discharges.” International Journal of Remote Sensing, 18(9): p. 1987-2019.

Davis, J. L., Herring, T.A., Shapiro, I. I., Rogers, A. E., Elgered, G. (1985). “Geodesy by radio interferometry: Effects of atmospheric modelling errors on estimates of baseline length.” Radio Sci., 20, 1593-1607, 1985.

Deo, R.C., Mi, J., Nathan, G.J. (2007). “The influence of nozzle aspect ratio on plane jets.” Exp. Therm. Fluid Sci., Vol.31, pp.825– 838.

Demuren, A.O., Rodi, W. (2006). “Calculation of flow and pollutant dispersion in meandering channels.” Journal of Fluid Mechanics 172, 63.

Demuren,A.O., Rodi, W. (1984). “Calculation of turbulence-driven secondary motion in non-circular ducts.” Journal of Fluid Mechanics, (140), 189- 222.

Deng, Z., Singh, V., Bengtsson, L. (2001). ”Longitudinal Dispersion Coefficient in Straight Rivers.” J. Hydraul. Eng., 127(11), 919–927.

Deng, Z., Bengtsson, L., Singh, V., Adrian, D. (2002). "Longitudinal Dispersion Coefficient in Single-Channel Streams." Journal of Hydraulic Engineering, 128(10), 901-916.

Dietrich, W. E.. and Smith, J. D. (1983). “Influence of the point bar on flow through curved channels.” Water Resources Res., 19(5), 1173-1192.

Doneker, R.L., Jirka, G.H. (2007). “CORMIX User Manual: A Hydrodynamic Mixing Zone Model and Decision Support System for Pollutant Discharges into Surface Waters. ” EPA-823-K-07-001, Dec. 2007.

Donlon, C.J., Minnett, P., Gentemann, C. (2002). “Towards improved validation of satellite sea surface skin temperature measurements for climate research.” Journal of Climate 15, 353–369.

Dow, K.E., Steffler, P.M., Zhu, D.Z. (2009). “Case study: Intermediate field mixing for a bank discharge in a natural river.” J. Hydraul. Eng., 135(1): 1–12. doi:10.1061/(ASCE)0733-9429(2009)135:1(1).

Dracos, T., Giger, M., Jirka, G. H. (1992). ‘‘Plane turbulent jets in a bounded fluid layer.’’ J. Fluid Mech., 241, 57–614.

Duan, J. G. (2004). “Simulation of Flow and Mass Dispersion in Meandering Channels.” J. Hydraul. Eng., (130)10, 964–976. DOI: 10.1061/(ASCE)0733-9429(2004)130:10(964)

Duan, J.G., Wang, S.S.Y., Jia, Y. (2001). “The applications of the enhanced CCHE2D model to study the alluvial channel migration processes.” J. Hydraul. Res., 39, 469–480.

Elder, J.W. (1959). “The dispersion of marked fluid in turbulent shear flow.” *J. Fluid Mech.* 5(4), 544-560.

Elhadi, N., Harrington, A., Hill, 1., Lau, Y. L., Krishnappan, B.G. (1984). “River Mixing-A state of the art report.” Canadian Journal of Civil Engineering, 11, 585-609.

Elhakeem, A.A., Elshorbagy, W., Chebbi, R. (2007). Oil Spill Simulation and Validation in the Arabian (Persian) Gulf with Special Reference to the UAE Coast. Water, Air, and Soil Pollution 184, 243–254.

Ellison, T. H. and J. S. Turner, Turbulent entrainment in stratified flows, J. Fluid Mech., 6, 423-448, (1959).

Fischer, H.B. (1969). The effect of bends on dispersion in streams. *Water Resour. Res.* 5(2), 496-506.

Fischer, H.B. (1968). “Dispersion prediction in natural streams”. Am. Soc. Civ. Engin., (SA5), 927-943.

Fischer, H.B., List, E.J., Koh, R.C.Y., Imberger, J., Brooks, N. H. (1979). “Mixing in inland and coastal waters.” Academic Press, NewYork.

Giger M, Dracos T, Jirka, G.H. (1991). “Entrainment and mixing in plane turbulent jets in shallow water. .” J Hydraul Res 29(4):615– 643.

Gharbi, S., Verrette, J. (1998). “Relation between longitudinal and transversal mixing coefficients in natural streams.” *J. Hydraulic Res. IAHR* 36(1), 43–53.

Glover, R. E. (1964). Dispersion of dissolved or suspended materials in flowing streams: *U.S. Geol. Survey Prof. Paper*. 433-B, 32 p.

Gowda, T.P.H. (1984). “Water Quality Prediction in Mixing Zones of Rivers.” Journal of Environmental Engineering, 110, 751–769.

Goudsmit, G.H, Peeters, F, Gloor, M, Wuest, A. (1997). “Boundary versus internal diapycnal mixing in stratified natural waters.” J. Geophys. Res. 102:27903–14

Gualtieri, C. (2009). “RANS-based simulation of transverse turbulent mixing in a 2D geometry.” *Environ. Fluid Mech.* 10(1-2), 137–156.

Harris, J.E., Antenucci, J.P., Okely, P.N., Mills, R., Yeates, P.S., 2009, “Three-dimensional hydrodynamic modeling of a coastal embayment for multiple use industrial discharge and infrastructure development.” 18th World IMACS / MODSIM Congress.

Hassanzadeh, S., Hosseinibalam, F., Rezaei-Latifi, A. (2011). “Three-dimensional numerical modeling of the water exchange between the Persian Gulf and the Gulf of Oman through the Strait of Hormuz.” *Oceanological and Hydrobiological Studies* 41, 85–98.

Hetland, R.D. (2005). “Relating river plume structure to vertical mixing. ” *J. Phys. Oceanogr*. 35 (9), 1667–1688.

Hetland, R.D., (2009). “The effects of mixing and spreading on density in near-field river plumes. ” *Dynamics of Atmospheres and Oceans* 49, 37–53.

Hetland, R. D., and Hsu, T.-J. (2013). Freshwater and sediment dispersal of large river plumes, in “Biogeochemical Dynamics at Large River-Coastal Interfaces: Linkages with Global Climate Change”, Editors: Thomas S. Bianchi, Mead A. Allison, and Wei-Jun Cai, Cambridge University Press, p55-85.

Hetland, R.D., MacDonald, D.G. (2008). “Spreading in the near-field Merrimack river plume.” *Ocean Model*. 21, 1-2 , 12–21.

Hickey, B., L. Pietrafesa, D. Jay, and W. Boicourt (1998). “The Columbia River plume study: Subtidal variability in the velocity and salinity fields.” *J. Geophys. Res.*, 103(C5), 10,339–10,368.

Horner-Devine, A.R., D.A. Jay, P.M. Orton, and E.Y. Spahn. (2009). “A conceptual model of the strongly tidal Columbia River plume. ” *Journal of Marine Systems* 78: 460–475.

Horner-Devine, A.R., R.D. Hetland, MacDonald, D.G (2015). “Mixing and transport in coastal river plumes. ” *Annual Review of Fluid Mechanics* 47 (Volume publication date December 2015)

Holley, E.R., Siemons, J., Abraham, G. (1972). “Some aspects of analyzing transverse diffusion in rivers. ” *J. Hydraulic Res.* 10(1), 27–57.

Holly, F.M., (1975). “Two-dimensional mass dispersion in rivers.” Colorado State University Hydrology Papers, 78. Fort Collins : Colorado State University.

Holly, F.M. (1985). “Dispersion in rivers and coastal waters. 1. Physical principles and dispersion equations, in Novak, P. (ed.).” Developments in Hydraulic Engineering, Elsevier, London, 1-37.

Hsiao, S.-C., Hsu, T.-W., Lin, J.-F., and Chang, K.-A. (2011). “Mean and turbulence properties of neutrally buoyant round jet in wave environment.” J. Waterway, Port, Coastal, Ocean Eng., 137(3), 109–122.

Hsieh, T.Y., Yang, J.C. (2003). “Investigation on the suitability of two-dimensional depth-averaged models for bend-flow simulation.” J. Hydraul. Eng., 129(8), 597–612.

Hunt, G. R., Linden, P. F. & Cooper, P. 2001 Thermal stratification produced by jets and plumes in enclosed spaces. Building Environ. 36, 871–882.

Hunt, C.D., Mansfield, A.D., Mickelson, M.J., Albro, C.S., Geyer, W.R., Roberts, P.J.(2010). " Plume tracking and dilution of effluent from the Boston sewage outfall." Marine Environ. Res. 70(2), 150–161.

Israelsson, P.H., Kim, Y.D., and Adams, E.E. (2006). "A comparison of three Lagrangian approaches for extending near field mixing calculations." Environ. Model. Softw. 21(12): 1631–1649. doi:10. 1016/j.envsoft.2005.07.008.

Jamieson, E.C., Rennie, C.D., Townsend, R.D. (2013a). "3D flow and sediment dynamics in a laboratory channel bend with and without stream barbs." J. *Hydraulic Eng*. 139(2), 154–166.

Jamieson, E.C., Ruta, M.A., Rennie, C.D., Townsend, R.D. (2013b). "Monitoring stream barb performance in a semi-alluvial meandering channel: flow field dynamics and morphology." *Ecohydrology*. 6(4), 611–626.

Jeon, T., M., Baek, K.O., Seo, I.W. (2007). "Development of an empirical equation for the transverse dispersion coefficient in natural streams." Environ. Fluid Mech. (7), 317–329.

Jiménez-Muñoz, J.C., Cristo´bal, J., Sobrino, J.A., So`ria, G., Ninyerola, M., Pons, X. Revision of the single-channel algorithm for land surface temperature retrieval from Landsat thermal-infrared data. IEEE Geoscience and Remote Sensing Letters 47 (1), 2009.

Jime´nez- Mun˜oz, J.C., Sobrino, J.A (2003). "A generalized single-channel method for retrieving land surface temperature from remote sensing data." Journal of Geophysical Research 108 (D22).

Jirka, G. H., Abraham, G., Harleman, D.R.F. 1975. "An assessment of techniques for hydrothermal prediction." Technical Rep. No. 203, R.M. Parsons Laboratory for Water Resources and Hydrodynamics, Cambridge, Mass. also published by U.S. Nuclear Regulatory Commission, Rep. No. NUREG-0044, 1976, Washington, D.C.

Jirka, G. H., Adams, E. E., and Stolzenbach, K. D. (1981). "Buoyant Surface Jets." Journal of the Hydraulics Division-ASCE, 107(11), 1467-1487.

Jirka, G.H., Doneker, R.L., Hinton, S.W. (1996). "User's Manual for CORMIX: A Hydrodynamic Mixing Zone Model and Decision Support System for Pollutant Discharges into Surface Waters, U.S". Environmental Protection Agency, Tech. Rep., Environmental Research Lab, Athens, Georgia, USA.

Jirka, G.H. (2004). "Integral Model for Turbulent Buoyant Jets in Unbounded Stratified Flows Part 1: Single Round Jet." Environmental Fluid Mechanics, Vol. 4: 1-56. Kluwer Academic Publishers.

Jirka, G. H. (2006). "Integral model for turbulent buoyant jets in unbounded stratified flows. 2: plane jet dynamics resulting from multiport diffuser jets." Environmental Fluid Mechanics, 6, 43–100.

Jirka, G.H. (2007). “Buoyant Surface Discharges into Water Bodies. II: Jet Integral Model.” Journal of Hydraulic Engineering, Vol. 133, No. 9, pp. 1021-1036.

Jirka, G.H., E.E. Adams, and K.D. Stolzenbach, 1981."Buoyant Surface Jets," Journ. Hyd. Div., ASCE, Vol. 107, No. HY11, pp. 1467-1487.

Johnson, T. R., Ellis, C. R., Stefan, H. G. (1989). “Negatively buoyant flow in a diverging channel. IV: Entrainment and dilution. ” Journal of Hydraulic Engineering, 115: 437–456, doi:10.1061/ (ASCE)0733-9429(1989)115:4(437)

Jones, G. R., Nash, J. D., Jirka, G. H. (1996). “Cormix3: An expert system for mixing zone analysis and prediction of buoyant surface discharges.”Technical Rep., DeFrees Hydraulics Laboratory, CornellUniv., Cornell, NY.

Jones, G., Nash, J., Doneker, R., Jirka, G. (2007). “Buoyant Surface Discharges into Water Bodies. I: Flow Classification and Prediction Methodology.” J. Hydraul. Eng., 133(9), 1010–1020.

Johnston, A. J., Volker, R. E. (1993). “Round buoyant jet entering shallow water.” J. Hydrosci. Hydraul. Eng., 31(1), 121–138.

Kakoulaki, G., MacDonald, D.G., Horner-Devine, A.R. (2014). “The role of wind in the near- and mid-field of a river plume. ” *Geophysical Research Letters* 41: 5132–5138

Kashyap, S., Constantinescu, G., Rennie, C.D., Post, G., Townsend, R. (2012). “Influence of channel aspect ratio and curvature on flow, secondary circulation, and bed shear stress in a rectangular channel bend.” *J. Hydraulic Eng.* 138(12), 1045–1059.

Katz, C.N., Chadwick, D.B., Rohr, J., Hyman, M., Ondercin, D. (2003). “Field measurements and modelling of dilution in the wake of a US navy frigate.” *Marine Pollution Bulletin*. 46(8), 991–1005.

Kaufman, J. T., Adams, E. E. (1981). “Coupled near and far field thermal plume analysis using finite element techniques.” Rep. MIT-EL 81-036, Energy Laboratory, Massachusetts Institute of Technology, Cambridge, Mass.

Kay, J.E., Kampf, S.K., Handcock, R.N., Cherkauer, K.A., Gillespie, A.R., Burges, S.J. (2005). “Accuracy of lake and stream temperatures estimated from thermal infrared images.” Journal of the American Water Resources Association 41, 1161–1175.

Keller, E.A. (1971). “Areal sorting of bed-load material: the hypothesis of velocity reversal.” *Geological Society of America Bulletin*. 82(3), 753-756.

Kim, D., 2012. “Assessment of longitudinal dispersion coefficients using acoustic Doppler current profilers in large river.” J. Hydro-environ. Res. (6), 29-39.

Kim, J.S., Cho, M. (2007). “Enhanced first-order theory based on mixed formulation and transverse normal effect.” Int J Solids Struct 2007;44:1256–76.

Kim DG, Cho, H.Y. (2006). “Modelling the buoyant flow of heated water discharged from surface and submerged side outfalls in shallow and deep water with a cross flow.” Environmental Fluid Mechanics 6: 501–518, DOI 10Ð1007/s10652-006-9006-3.

Kironoto, B.A., Graf, W.H. (1994). “Turbulence characteristics in rough uniform open-channel flow.” Proceedings of the *ICE - Water Maritime and Energy*. 106 (4), 333–344.

Kishino, M., Matsunaga, T., Abrams, M., Kato, M. Water quality and temperature mapping using ASTER, in: International Geoscience and Remote Sensing Symposium (IGARSS) 2000, Honolulu, Hawaii, 2000.

Kishino, M., Matsunaga, T., Abrams, M., Kato, M. (2000). “Water quality and temperature mapping using ASTER” International Geoscience and Remote Sensing Symposium (IGARSS) 2000, Honolulu, Hawaii.

Koole, R., Swan, C. (1994). “Dispersion of pollution in a wave environment.” *In: Proc., 24th Coast. Eng. Conf., Kobe.*

Kumar, A., Minnett, P.J., Podesta´, G., Evans, R.H. (2003). “Characteristics of the atmospheric correction algorithms used in retrieval of sea surface temperatures from infrared satellite measurements: global and regional aspects.” Journal of the Atmospheric Sciences 60, 575–585.

Lam, K.M., and Xia, L.P., 2001, “Experimental simulation of a vertical round jet issuing into an unsteady cross flow,” J. Hydraul. Eng., 127(5), 369-379.

Lal, P. B. B., Rajaratnam, N. (1977). “An Experimental Study Of Bluff Buoyant Turbulent Surface Jets.” Journal of Hydraulic Research, vol. 15, no. 3, pp. 261-275, 1977

Lamaro, A. A., Marinelarena, A., Torrusio, S. E., Sala, S. E. (2013). “Water surface temperature estimation from Landsat 7 ETM+ thermal infrared data using the generalized single-channel method: Case study of the Embalse del Río Tercero (Cordóba, Argentina).” Advances in Space Research, 492 - 500.

Landsberg, J. H. (2002). "The effects of harmful algal blooms on aquatic organisms". Reviews in Fisheries Science 10 (2): 113–390. doi:10.1080/20026491051695

Lau, Y.L., Krishnappan, B.G. (1981). “Modelling Transverse Mixing in Natural Streams.” ASCE J HydrDiv ASCE. 107(2), 209–226.

Ledwell, J. R., Duda, T. F., Sundermeyer, M. A., Seim, H. E. (2004). “Mixing in a coastal environment: 1. A view from dye dispersion.” Journal of Geophysical Research, 109(C10013). doi:10.1029/2003JC002194.

Lee, J.H., Qian,A., 2003."Three-dimenaional modeling of hydrodynamic and flushing in deep bay, International Conference on Estuaries and Coasts.

Lin, C.Y., Holley, E.R., Maxwell, W.H.C. (1977). “Buoyant surface jets discharged into a strong crossflow”. University of Illinois at Urbana-Champaign. Final report, Project No. B-088-ILL

Lin, J. F., Hsiao, S. C., Hsu, T. W. and Chang, K. A., 2012. Buoyancy effect on turbulent round jet under regular waves, J. Waterw. Port Coast. Ocean Eng., ASCE, 139(3): 190–208. Malcangio, D., Petrillo, A.F., 2010, “Modeling of brine outfall at the planning stage of desalination plants”, Desalination, 254, 114–125.

Luk, G.K.Y., Lau, Y.L., Watt, W.E., 1990. “Two-Dimensional Mixing in Rivers with Unsteady Pollutant Source.” Journal of Environmental Engineering 116, 125–143.

Luketina, D., Imberger, J., (1987). Characteristics of a suface buoyant jet. J. Geophys. Res. 92 (C5), 5435–5447.

Maderich, V., Heling, R., Bezhenar, R., Brovchenko, I., Jenner, H., Koshebutskyy, V., Kuschan, A., Terletska, K., 2008. Development and application of 3D numerical model THREETOX to the prediction of cooling water transport and mixing in the inland and coastal waters. Hydrological Processes 22, 1000–1013.

Markatos NC, Malin MR, Cox G. Mathematical modeling of buoyancy-induced smoke flow in enclosures. Int J Heat Mass Transfer 1982;25:63–75.

MacVicar, B.J., Rennie, C.D., Roy, A.G. (2010). Discussion of “Unifying Criterion for the Velocity Reversal Hypothesis in Gravel-Bed Rivers” by D. Caamaño, P. Goodwin, J. M. Buffington, J. C. P. Liou, and S. Daley-Laursen. *J. Hydraulic Eng.* 136(8), 550–552.

McCabe, R.M., MacCready P, Hickey B.M. (2009). “Ebb tide dynamics and spreading of a large river plume. ” *J. Phys. Oceanogr*. 39:2839–56

Mclean, S.R. (1984). “A Model for Flow in Meandering Streams.” Water Resources Research 20, 1301.

Moawad, A.K., (1998) "An experimental study of dilution and mixing with turbulent jets in cross flows." Thesis submitted in partial fulfillment of the requirements for the Ph.D. degree at Alberta University, Spring 1998.

Mohammadian, A.M., Le Roux, D., (2008). "Fourier analysis of upwind schemes in shallow water systems for gravity and Rossby waves." International Journal for Numerical Methods in Fluids, (57)4, 389-416.

Molls, T., Chaudhry, M.H. (1995). "Depth-Averaged Open-Channel Flow Model." Journal of Hydraulic Engineering 121, 453–465.

Moore, S.; et al. (2011). "Impacts of climate variability and future climate change on harmful algal blooms and human health". Proceedings of the Centers for Oceans and Human Health Investigators Meeting. doi:10.1186/1476-069X-7-S2-S4.

Morelissen, R., Van der Kaaij, T., Bleninger, T., 2013. Dynamic coupling of near field and far field models for simulating effluent discharges. Water Science & Technology 67, 2210.

Mori, N., Chang, K.A. (2003). "Experimental study of a horizontal jet in a wavy environment".J.Eng.Mech129(10),1149–1155.

Morton, B, Taylor, G.I., Turner, J.S. (1956). "Turbulent gravitational convection from maintained and instantaneous sources. " Proc. Roy. Soc., A234:1-23.Nekouee, N., Roberts, P., Schwab, D., McCormick, M. (2013). "Classification of Buoyant River Plumes from Large Aspect Ratio Channels." J. Hydraul. Eng., 139(3), 296–309.

Nekouee, N. (2010). "Dynamics and numerical modeling of river plumes in lakes." NOAA Technical Memorandum Rep. GLERL-151, NOAA, Ann Arbor, MI.

Nekouee, N., Roberts, P. J. W., Schwab, D. J., & McCormick, M. J. (2013). "Classification of buoyant river plumes from large aspect ratio channels. " *Journal of Hydraulic Engineering*, 139(3), 296–309.

Nikiema, O., Devenon, J.L., Baklouti, M. (2007). "Numerical modelling of the Amazon River plume." *Cont. Shelf Res.* 27(7), 873–899.

Okely, P., Yeates, P.S., Antenucci, J.P., Imberger, J., Hipsey, M.R., 2006, "Modelling of the impact of the Perth Seawater Desalination Plant discharge on dissolved oxygen in Cockburn Sound" report, The University of Western Australia P06/045/JA.

Parker, G.T., Droste, R.L., Rennie, C.D. (2012). "Coupling model uncertainty for coupled rainfall/runoff and surface water quality models in river problems." Ecohydrology. 6(5), 845–851.

Phillips, N. A., 1957. \A co-ordinate system having some special advantages for numerical

forecasting." Journal of Meteorology 14: 184{185. 185, 195

Pilechi, A., Rennie, C.D., Mohammadian, A., Zhu, D.Z., Delatolla, R. (2012). "Physical mixing patterns of water and contaminants in the North Saskatchewan River." Technical Report, Alberta Environment, Canada.

Pope, S. B. (2000). Turbulent flows, Cambridge University Press, Cambridge, U.K.

Pritchard, M., Huntley, D. A. (2002). "Instability and mixing in a small estuarine plume front." Estuarine, Coastal Shelf Sci., 55(2), 275–285.

Pritchard, M., and Huntley, D. A. (2006). "A simplified energy and mixing budget for a small river plume discharge." J. Geophys. Res., 111, 1–11.

Putz, G., Smith, D., W. (1998). "Verification of a Transient Input, Two-dimensional, River Mixing Model". Canadian Journal of Civil Engineering, 25: 51.66.

Rajaratnam, N. (1976). Turbulent Jets, Elsevier, Amsterdam, The Netherlands, 304.

Rajaratnam, N., Humphries, J. A. (1984). "Turbulent non-buoyant surface jet." J. Hydraul. Res., 22(2), 103–115.

Rajaratnam, N. (1985). "An Experimental Study of Bluff Surface Dis charges with Small Richardson Number." J. Hydraul. Res., 23(1), 47, 47-55. DOI:10.1080/00221688509499376.

Rennie, C.D., Church, M. (2010). "Mapping spatial distributions and uncertainty of water and sediment flux in a large gravel bed river reach using an acoustic Doppler current profiler." *J. Geophys. Res.* 115( F3), F03035, doi: 10.1029/2009JF001556.

Rennie, C.D., Rainville, F. (2006). Case study of precision of GPS differential correction strategies: influence on aDcp velocity and discharge estimates. *J. Hydraulic Eng.* 132(3), 225–234.

*Roberts, P.J.W. (2013). "Ocean Outfalls." In Handbook of Environmental Fluid Dynamics, Volume Two. H. J. Fernando, Ed., CRC Press: 229-242.*

*Roberts, P.J.W., Snyder, W.H., and Baumgartner, D.J. (1989a). "Ocean Outfalls. I: Submerged Wastefield Formation." Journal of Hydraulic Engineering, ASCE, 115(1), 1 25.*

*Roberts, P.J.W., Snyder, W.H., and Baumgartner, D.J. (1989b). "Ocean Outfalls. II: Spatial Evolution of Submerged Wastefield." Journal of Hydraulic Engineering, ASCE, 115 (1), 26-48.*

Roberts, P. J. W., Snyder, W. H., Baumgartner, D. J. (1989). “Ocean outfalls III: Effect of diffuser design on submerged wastefield.” J. Hydraul. Eng., 115(1), 49–70.

Roberts, P. J. W., and Toms, G. (1987). “Inclined dense jets in flowing currents.” J. Hydraul. Eng., 113(3), 323–341.

Roberts, P.J.W., Snyder, W.H., Baumgartner, D.J., 1989a. Ocean Outfalls. I: Submerged Wastefield Formation. Journal of Hydraulic Engineering 115, 1–25.

Roberts, P.J.W., Snyder, W.H., Baumgartner, D.J., 1989b. Ocean Outfalls. III: Effect of Diffuser Design on Submerged Wastefield. Journal of Hydraulic Engineering 115, 49–70.

Roberts, P.J.W., Snyder, W.H., Baumgartner, D.J., 1989c. Ocean Outfalls. II: Spatial Evolution of Submerged Wastefield. Journal of Hydraulic Engineering 115, 26–48.

Rodi, W. (1993). “Turbulence models and their application in hydraulics: a state-of-the-art review.” ed. 3 *International Association for Hydraulic Research*, Balkema, Rotterdam.

Rodi W. Turbulence models and their application in hydraulics. Germany: University of Karlsruhe; 1980.

Rowiński, P.M., Guymer, I., Kwiatkowski, K. (2008). “Response to the slug injection of a tracer a large-scale experiment in a natural river”. *Hydrological Sci. J.* 53(6), 1300–1309.

RPS Consulting Engineers, 2008, “Desalination Study Report of Dublin Region”.

Rutherford, J.C. (1994). *River mixing*. Wiley, Chichester [England] ; New York.

Safaie, B. (1979). “Mixing of buoyant surface jet over sloping bottom." J. Wtrwy.Port Coast. Oc. Div., ASCE, 105(4), 357-373.

Sayre, W.W., Caro-Coredro, R. (1979). “Shore attached thermal plumes in rivers.” Proc. Institute on River Mechanics- Modelling of Rivers. Colorado State University, July 5-15.

Schlichting, H. (1979). Boundary layer theory, 4th Ed., McGraw-Hill, New York.

Schlichting, H., Gersten, K. (2000). “Boundary-layer theory”, 8th Ed., Springer, Berlin, Chap. 22.3, 663.

Schneider, W. (1985). “Decay of momentum flux in submerged jets.” J. Fluid Mech., 154(5), 91–110.

Seo, I.W., Baek, K.O. (2004). “Estimation of the longitudinal dispersion coefficient using the velocity profile in natural streams.” J. Hydraul. Eng., 130(3), 227–236.

Seo, I., Baek, K.O., Jeon, T.M. (2006). “Analysis of transverse mixing in natural streams under slug tests.” *J. Hydraulic Res.* 44(3), 350–362.

Seo, I., Lee, M., Baek, K. (2008). "2D Modelling of heterogeneous dispersion in meandering channels." J. Hydraul. Eng.,134(2), 196–204.

Seo, I.W., Cheong, T. S. (1998). "Predicting longitudinal dispersion coefficient in natural streams." J. Hydraul. Eng.,124(1), 25-32.

Seo, I.W., Park, S.W. (2010). "Two dimensional analysis of flow patterns and dispersion in meandering channels." River Flow 2010, edited by Dittrich, Koll, Aberle & Geisenhainer , Bundesanstalt für

Wasserbau. ISBN 978-3-939230-00-7.

Shen, C., Niu, J., Anderson, E.J., Phanikumar, M.S. (2010). "Estimating longitudinal dispersion in rivers using Acoustic Doppler Current Profilers." Advances in Water Resources (33), 615–623.

Shen, C., Niu, J., Anderson, E.J., Phanikumar, M.S. (2010). Estimating longitudinal dispersion in rivers using acoustic Doppler current profilers. *Adv. Water Res.* 33(6), 615–623.

Shinneeb, A., Balachandar, R., and Bugg, J. (2011). "Confinement Effects in Shallow-Water Jets." J. Hydraul. Eng., 137(3), 300–314.

Shirazi, M.A., Davis, L. R. (1976). "Analysis of buoyant surface jets." J. Heat Transfer, Trans.. Am. Soc. Mining Eng., pp. 367-372.

Shirazi, M. A. and Davis, L. R., "Workbook of Thermal. Plume Prediction Vol. 2, Surface Discharges." Environmental Protection Technology Series, U.S. Environmental. Protection Agency, Corvallis, Oregon, Report No. EPA-R2-72-0056, 1974, 430 pp.

Sobey, R. J., Johnston, A. J., Keane, R. D. (1988). "Horizontal Round Buoyant Jet in Shallow Water." J. Hydraul. Eng., 114(8), 910– 929.

Somlyódy, L., (1982). "An approach to the study of transverse mixing in streams." Journal of Hydraulic Research 20, 203–220.

Song, T., Graf, W.H. (1996). Velocity and turbulence distribution in unsteady open-channel flows. *J. Hydraulic Eng.* 122(3), 141–154.

Srivastava, P.K., Majumdar, T.J., Bhattacharya, A.K. (2009). "Surface temperature estimation in Singhbhum Shear Zone of India using Landsat-7 ETM+ thermal infrared data". Advances in Space Research, 43 (10), 1563–1574.

Stefan, H., Hayakawa, N., Schiebe, F. R. (1971). "Surface Discharge of Heated Water." Water Pollution Control Research Series 16130 PSU 12171.

Stephan, H., Bergstedt, L., Mrosla, E. (1975). "Flow Establishment and Initial Entrainment of Heated Water Surface Jets." Environmental Protection Agency Report No. EPA-660/3-75-014.

Sharp, J. J. 1986. The Effects of Waves on Buoyant Jets. Proc. Inst. Civ. Eng., 81: 471–475. part 2

Stamou, A.I., Nikiforakis, I.K., 2013. Integrated modelling of single port, steady-state thermal discharges in unstratified coastal waters. Environmental Fluid Mechanics 13, 309–336.

Stolzenbach, K.D., Harleman, D.R.F. (1973). "Three-dimensional heated surface jets." Water Resour. Res., 9, 129-137.

Stolzenbach, K., Harleman, D.R. F. (1971). "An Analytical and Experimental Investigation of Surf ace Discharges of Heated Water." M. I. T. Hydrodynamics Laboratory Technical Report No. 135, February, 1971, 212 pp.

Swean, T. F., Jr., Ramberg, S. E., Plesniak, M. W., Stewart, M. B. (1989). ''Turbulent surface jet in channel of limited depth. " J. Hydraul. Eng., 115(12), 1587–1606.

Tam,B.F.,Li,C.W.,2008.Flowinducedbyaturbulentjetunderrandomwaves. J. Hydraul.Res.46(6),820–829.

Torgersen C.E., Faux R.N., McIntosh, B.A., Poage, N.J., Norton D.J. (2001). "Airborne thermal sensing for water temperature assessment in rivers and streams. " RemoteSensing of Environment, 76, 386–398.

Townsend, A. A. (1966). "The mechanism of entrainment in free turbulent flows." J. Fluid Mech. 26, 689–715.

Vaselali, A., Vaselali, M., 2009, "Modeling of Brine Waste Discharge Spreading Under Tidal Currents", Journal of Applied Science 9 (19):3454-3468.

Versteeg, H., Malalasekara, W. 2007. An Introduction to Computational Fluid Dynamics. The Finite Volume Method (2nd Edition ).

Vossen, B. van, 2000. Horizontal Large Eddy simulations; evaluation of ow computations

with Delft3D-FLOW. Tech. Rep. MEAH-197, WL j Delft Hydraulics, Delft, The Netherlands.

534, 537

Vanvari, M. R., and Chu, V. H. (1974). "Two-dimensional turbulent surface jets of low Richardson number." Tech. Rep. No. 74-2 [FML], Fluid Mechanics Laboratory, Dept. of Civil Engineering and Applied Mechanics, McGill Univ., Montreal.

Worthy J, Sanderson V, Rubini P. Comparison of modified $k$-$\varepsilon$ turbulence models for buoyant plumes. Numer Heat Transfer B— Fund 2001;39:151–65.

Wang, J., MacDonald, D. G., Orton, P. M., Cole, K., Lan, J. (2015), "The Effect of Discharge, Tides, and Wind on Lift-Off Turbulence" Estuaries and Coasts DOI 10.1007/s12237-015-9958 yReceived: 14 January 2014 /Revised: 4 February 2015 /Accepted: 25 February 2015 # Coastal and Estuarine Research Federation 2015.

Whitney, M.M., Garvine, R.W. (2005). "Wind influence on a coastal buoyant outflow." Journal of Geophysical Research: Oceans, 110, C3, 1978–2012. DOI: 10.1029/2003JC002261.

WL | delft hydraulics. (1999) "Delft3D-FLOW user manual" Version 3.05.

Yankovsky, A.E., Chapman, D.C. (1997). "A Simple Theory for the Fate of Buoyant Coastal Discharges." J. Phys. Oceanogr., 27, 1386–1401.doi: http://dx.doi.org/10.1175/1520 0485(1997)027<1386:ASTFTF>2.0.CO;2

Ye, J., McCorquodale, J. (1997). "Depth-averaged hydrodynamic model in curvilinear collocated grid." J. Hydraul. Eng.,123(5), 380–388.

Yotsukura, N., Cobb, E.D. (1972). Transverse Diffusion of Solutes in Natural Streams. *Geological Survey Professional*. C1–C19.

Yotsukura, N., Fischer, H.B., Sayre, W.W. (1970). "Mixing characteristics of the Missouri River between Sioux City, Iowa and Platmouth, Nebraska." US geological survey, Water supply Paper, No. 1899-G.

Yotsukura, N., Sayre, W.W. (1976). "Transverse mixing in natural channels."*Water Resour. Res.* 12(4), 695-704.

Zhang, W., Wilkin, J., Chant R. (2009). "Modeling the pathways and mean dynamics of river plume dispersal in the New York Bight. " *J. Phys. Oceanogr*. 39: 1167–1183.

Zhang, W., Zhu, D,Z. (2011). "Transverse Mixing in an Unregulated Northern River." J. Hydraul. Eng., (137)11, 1426-1440.

Zhao, L. (2012). "Development of an Integrated System for the Simulation and Assessment of Produced Water Discharges from Offshore Platforms". Ph.D thesis, Concordia University, Montreal, Quebec, Canada.

Xu, Z. S., Chen, Y. P., Zhang, C. K., Li, C. W., Wang, Y. N. and Hu, F., 2014. Comparative study of a vertical round jet in regular and random waves, Ocean Eng., 89, 200–210.

Xu, Z., Chen, Y., Zhang,C.,Li,C., Wang,Y.,Hub,F. (2014). "Comparative study of a vertical round jet in regular and random waves." Ocean Engineering, 89(2014)200–210.

Yan Z, Holmstedt G. A two-equation turbulence model and its application to a buoyant diffusion flame. Int J Heat Mass Transfer 1999;42:1305–15.

Zijl, F. ,2002. “On the effect of non-hydrostatic simulation on buoyant jets”, masterThesis,TU Delft, Faculty of Civil Engineering and Geosciences, Hydraulic Engineering.